Photoelectron spectroscopy on magnesium ensembles in helium nanodroplets

Dissertation

zur

Erlangung des akademischen Grades

doctor rerum naturalium (Dr. rer. nat.)

der Mathematisch-Naturwissenschaftlichen Fakultät

der Universität Rostock

vorgelegt von

Lev Kazak

geb. am 05.07.1988 in Karaganda, UdSSR

Rostock

August 2019

Abstract

The special conditions provided by the ultracold and liquid environment of helium nanodroplets allow the formation of unusual and unique structures from embedded complexes. A recent example is magnesium atoms, which show evidence for the formation of a metastable structure called foam, in which single atoms are separated by a layer of helium. The present work focuses on the electronic properties of the foam, which were studied by photoelectron spectroscopy. The photoemission spectra show characteristic features which are assigned to the ionization from highly excited atomic states. This is attributed to a collapse of the photoexcited ensemble, which is accompanied by an energy transfer to the foam atoms. The maximum number of atoms that can be stabilized in the droplet is obtained by analyzing the doping dependence of the photoelectron features with respect to the pick-up statistic. Mass spectrometry studies on heavily doped droplets show the formation of magnesium clusters. The ionization potentials of small Mg_N clusters are determined by recording cluster ion yield as a function of the photon energy.

Kurzzusammenfassung

Die besonderen Bedingungen der Helium Nanotropfen, die in der ultrakalten und flüssigen Umgebung herrschen, können zur außergewöhnlichen und einzigartigen Strukturen eingebetteter Komplexe führen. Ein aktuelles Beispiel sind die Magnesiumatome, die Hinweise zeigen auf die Bildung einer metastabilen „Schaum"-Struktur, bei der einzelne Mg-Atome durch eine Heliumschicht getrennt sind. Der Fokus dieser Arbeit liegt auf den elektronischen Eigenschaften dieses Schaums, die mit Photoelektronenspektroskopie untersucht wurden. Die Photoemissionsspektren zeigen charakteristische Merkmale, die der Ionisation aus hochangeregten atomaren Zuständen zugeordnet werden können. Ursache ist der Kollaps des photoangeregtem Ensembles, der von einem Energietransfer auf die Schaum-Atome begleitet wird. Durch eine Analyse der Dotierungabhängigkeit der Photoelektronen Signale in Hinblick auf die Pick-up Statistik wurde die Maximalzahl an Atomen, die in einem Tropfen stabilisiert werden können, bestimmt. Massenspektrometrische Untersuchungen der Ionen stark dotierter Tropfen zeigen ein intensives Signal an Magnesiumclustern. Durch die Aufnahme der Ionenausbeuten als Funktion der Photonenenergie wurde die Ionisationspotentiale kleiner Mg_N Cluster ermittelt.

Contents

List of Figures

List of Tables

1 Introduction

High-resolution spectroscopy requires the preparation of atoms and molecules under well-defined conditions. One of the key parameters is the temperature, since it defines the number of populated vibrational and rotational states. Hence, the preparation of the investigated molecular samples at the lowest possible temperature is essential. To solve this problem several experimental methods have been developed. In matrix isolation spectroscopy, introduced in 1954 [1], particles are embedded into a solid state matrix at low temperature. However, such a technique has several disadvantages [2]. The interaction between molecules and matrix atoms leads to a perturbations of the molecular levels and, thus, results in shifts and inhomogeneous broadening of spectral lines. The situation becomes even more complex when particles occupy different site states which results in a multiplet structure of spectra. In addition, rotation is restricted for most of the molecules, thus, information about rotational structure cannot be obtained. As another approach, seeded supersonic jets provide cold and free molecules suitable for high-resolution spectroscopy [3, 4]. However, this method is hardly applicable to molecules having a low volatility [5]. It is important to note, that both methods allow to create clusters, even when clustering is unwanted.

Helium nanodroplets provide a manifold of opportunities to study isolated atoms, molecules and cluster [6–8]. Foreign particles can be picked-up by the droplets and effectively cooled down. Doping with a wide variety of particles has been reported, e.g. noble gases [9, 10], metals [11, 12] di- [13, 14] and polyatomic [15, 16] molecules, as well as bio-molecules, such as nucleobases [17, 18], amino acids [19, 20] and proteins [21, 22]. The temperature of the droplets ($0.37\,\mathrm{K}$) and optical transparency in the wide spectral range allow to conduct experiments in the ultracold environment. The weak interaction between dopants and helium atoms reduces the perturbation in the electronic structure, whereas the superfluid nature of the droplets permits rotationally resolved spectroscopy of molecules [23]. In addition, only two possible configurations of embedded particles in the droplet are possible, i.e. particles can be completely immersed in the droplet or reside on the surface. Besides single atoms and molecules, multiple particles can be picked-up and successfully aggregated to clusters, whereas the size of the clusters is

simply controlled by varying the particle density in the pick-up region. Hence, helium droplets are unique nanoscopic medium for spectroscopy. In the past, a variety of experiments have been performed, e.g. atomic [24–27] and high resolution molecular spectroscopy [28–30], studies on embedded clusters [31–33], chemical reactions [34–36] and electron diffraction [37–39]. Pure and doped droplets serve as an attractive target for studies of the interaction of matter with strong laser fields [40, 41] and collective processes [42, 43]. The superfluidity of He droplet reflects in presence of quantum vortices, which has been recently observed by diffractive imaging using free-electron laser radiation [44, 45].

The droplet environment allows to synthesize exotic structures. Polar molecules arrange themselves in linear chains inside the droplet [46]. Water molecules form cyclic water hexamers which are high energy isomers [47]. Alkali clusters on the surface of the droplets are created in high-spin states [48]. In droplets doped by Rb and Sr atoms, atoms are spatially separated, i.e., Rb is located on the surface, whereas Sr is immersed in the droplet interior [49]. The formation of spatially separated structures within the droplet is proposed for Ne and F atoms [50]. Recently, evidence was found that Mg atoms embedded in the nanodroplet do not form a cluster, but create a metastable network of isolated atoms called *foam* [51], in which atoms are located apart from each other and separated by a layer of helium.

The present work focuses on the electronic properties of a photoexcited Mg foam, which are studied by photoelectron spectroscopy. For these studies, the Mg doped droplets are ionized by resonant two-photon ionization at the laser wavelength corresponding to the foam absorption. Photoelectron spectra are recorded for a wide range of doping conditions and droplet sizes. The comparison of the features in the photoemission spectra with the level scheme of Mg reveals the presence of highly excited atomic states. The formation of highly excited atoms is discussed in terms of a foam collapse after photoabsorption. The dependence of the photoelectron yields on the doping conditions is analyzed with respect to the pick-up statistics. The application of this method allows to reveal the maximum number of Mg atoms that can be stabilized as a foam. Mass spectrometry studies beyond the stability limit show the presence of free Mg_N clusters. Cluster ion mass spectra recorded as a function of the photon energy allow to determine the ionization potentials of Mg_N in the size range $7 \leq N \leq 56$. The size dependence of the ionization potentials is discussed in terms of the conducting sphere model.

The thesis is structured as follows: Chapter 2 provides an overview of the formation,

size distributions, properties and doping of helium nanodroplets. Chapter 3 describes the properties of particles in droplets and provides a summary of the experimental and theoretical investigation of Mg doped droplets. Chapter 4 provides information relevant to mass spectroscopy of Mg clusters, i.e. shell structure of atomic clusters and size-dependent behavior of ionization potentials. In Chapter 5, a description of the experimental setup is given. Chapter 6 describes the experimental results, which are discussed in the following Chapter 7. Finally, in Chapter 8 the main achievements of this work are summarized and an outlook for future experiments is given.

2 Helium nanodroplets

This chapter is focusing on the general background of helium nanodroplets, including a method to produce the droplets and control their sizes and size distributions, physical properties and the pick-up technique.

2.1 Formation of He nanodroplets

The common way to produce helium[1] nanodroplets is similar to the technique, which is used to generate gas clusters. Generally, helium clusters are created in a supersonic expansion of cold gas through a tiny nozzle into vacuum [6]. The expansion process is adiabatic, meaning that there is no energy exchange between the expanding gas and the surrounding media. Under such conditions, the atoms are accelerated to velocities higher than the sound velocity and the velocity distribution narrows due to collisions between the particles. The temperature of the particles in the beam decreases and the formation of clusters and droplets becomes feasible.

For helium, the initial expansion conditions, such as pressure P_0 and temperature T_0 are used to adjust the size of the droplets. This could be explained by a close look at the pressure-temperature phase diagram [52], see Fig. 2.1. Starting from the initial condition at P_0 and T_0 the thermodynamical conditions follow different isentropes during the expansion and pass a phase line from different sides. This leads to various regimes of nanodroplet formation[2] [52, 53]:

(i) Regime 1: Subcritical Expansion. This process takes place at relatively high temperatures (T_0>10K). The isentropes cross the phase line from the gas phase [52]. In this regime, helium droplets are formed by gas condensation with sizes up to about N_{He}=3·10^4 atoms.

(ii) Regime 2: Critical Expansion. This expansion regime corresponds to the temperature range 9K<T_0<10K. The isentropes approach the phase line close to the critical point. Under this conditions liquid and gas phases of the helium coexist. Helium

---

[1]Here and in following by helium means ^{4}He isotope.

[2]Here, the conditions for expansion regimes as well as the droplet sizes are presented with respect to the experimental setup used in present work. See also Fig.5.2.
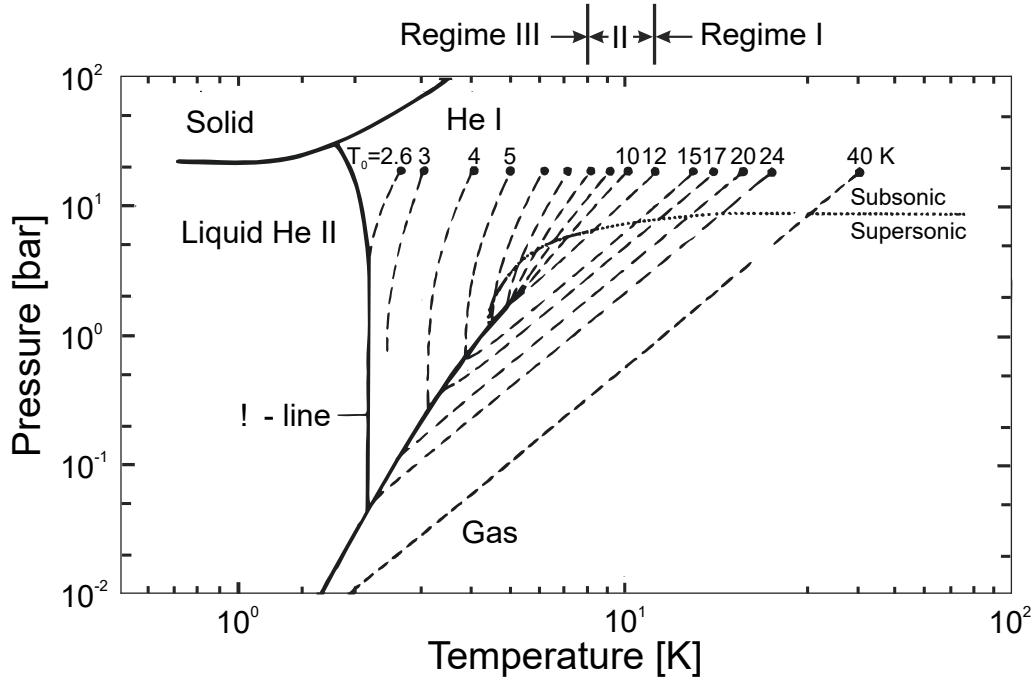
Figure 2.1: Helium phase diagram. The dashed lines correspond to different isentropes. The black dots show the initial starting point for P_0 =20 bar. Adapted from [52].

droplets are formed by two mechanisms, i.e. gas condensation and partial fragmentation of liquid helium formed at the nozzle [53]. Droplet sizes N_{He}=3·10^4-10^6 can be produced. A slight change in T_0 at a constant pressure leads to a strong change in the droplet size.

(iii) Regime 3: Supercritical expansion (T_0<9K): isentropes are strongly bent and cross the phase line from the liquid phase. In this regime, droplets are formed by the fragmentation of the liquid, during the propagation of the gas in the nozzle chanel [7,52]. Droplets with sizes N_{He}>10^6 could be created.

When helium gas is cooled to temperatures below the evaporation point at a low pressure, it completely liquefies in the reservoir. This leads to conditions, where a liquid jet is produced [54], with a diameter comparable to the nozzle size. Droplets of μm size are formed by a spontaneous break up of the filament due to the Rayleigh instability. The liquid jet technique, with other types of gases, such as hydrogen or other noble gases, are the subject of studies on the interaction of matter with strong laser fields [55] and in plasma physics [56, 57]. They serve as an attractive target for laser particle accelerators [58].

After the formation, nanodroplets reach their equilibrium temperatures by evapora-

tive cooling. This energy dissipation process has to be taken into account whenever excess energy is transferred to the droplet. Simultaneously, it is responsible for the decrease of the droplet size. In the case of a high amount of deposited energy, the droplet size can be strongly reduced.

Since the formation is a statistical process, which also depends on the expansion regime, droplets with a broad size distribution are produced in the expansion. In the experiment, it is challenging to determine the exact size distributions by common techniques, e.g. ionization of droplets combined with time-of-flight mass spectroscopy. The reason is the strong impact of fragmentation on the observed mass spectra. The signals from small fragments dominate, while the signal of initial large droplets is suppressed. The droplet sizes N_{He} have been obtained experimentally by different techniques, like scattering by an atomic beam [59, 60], beam depletion, electron attachment [61] and beam titration [62].

In the subcritical expansion, N_{He} have a log-normal distribution [59, 60, 63]. This has been experimentally verified by beams scattering experiments, where the helium beam is deflected by collisions with an atomic beam of heavy particles with a well defined and sharp velocity distribution. The size distribution has been deduced from the scattering angle. The log-normal distribution is described by the equation:

$$P(N_{He}) = \frac{1}{s\sqrt{2\pi}N_{He}} \cdot \exp[-\frac{(\ln(N_{He}) - \mu)^2}{2s^2}], \qquad (2.1)$$

where the parameters μ and s are connected to the mean $\overline{N}_{He}$ and the width of the distribution ΔN_{He}, as

$$\overline{N}_{He} = \exp(\mu + s^2/2) \qquad (2.2)$$

$$\Delta N_{He} = \exp(\mu - s^2 + s\sqrt{2\ln 2}) - \exp(\mu - s^2 - s\sqrt{2\ln 2}) \qquad (2.3)$$

It has been shown, that the value of ΔN_{He} is close to the mean droplet size $\Delta N_{He} \approx (0.88 \pm 0.06)\overline{N}_{He}$ [64]. It allows to calculate parameters μ and s by Eqs. 2.2 and 2.3 with known mean droplet size. Therefore, the droplet size distribution in the subcritical regime can be predicted. Examples of the distributions calculated according to Eq. 2.1-2.3 are shown in Fig. 2.2, left.

In the supercritical regime, droplets are formed by the fragmentation of liquid helium. This leads to a new size distribution, which has a linear-exponential shape [61] and
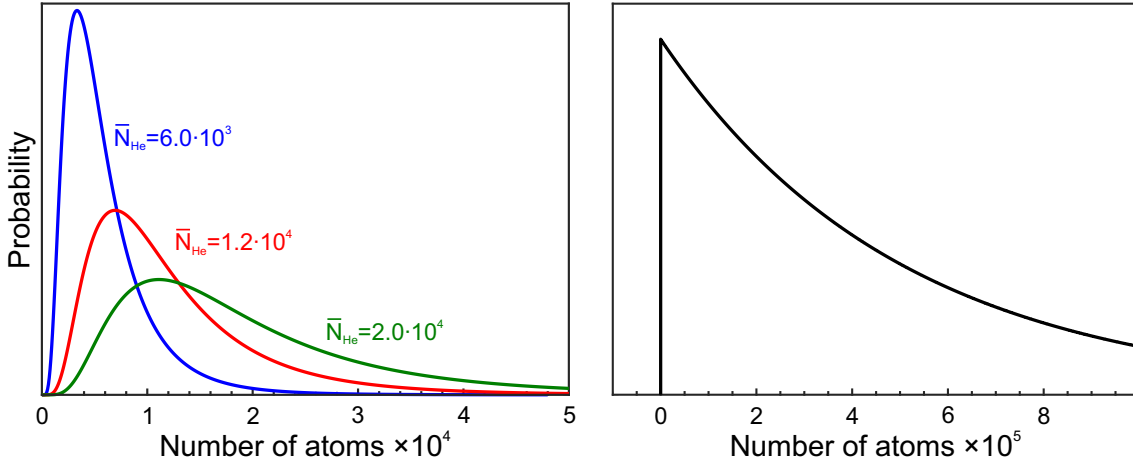
Figure 2.2: Examples of droplet size distributions in the different experimental regimes. (Left) Calculated log-normal distribution for three different mean droplet sizes (subcritical expansion). (Right) Calculated linear-exponential distribution for a mean size of $N_{He}^{avg} = 5 \cdot 10^5$ (supercritical expansion).

it has been experimentally verified by deflection of heavy positively and negatively charged droplets [65, 66]. The linear-exponential distribution can be calculated as:

$$P(N_{He}) = \frac{1}{\overline{N}_{He}} \exp\left(\frac{N_{He}}{\overline{N}_{He}}\right) \qquad (2.4)$$

where only the value of $\overline{N}_{He}$ is needed to estimate the experimentally produced droplet sizes. An example of the distribution calculated by Eq. 2.4 is shown in Fig. 2.2, right.

In the critical regime, the situation becomes more complex, due to contributions of two expansion phases. The final size distribution is bimodal [52, 66], being a superposition of log-normal and linear-exponential parts. Experimental data about the droplet sizes in this regime can be found in [66].

The information about the size distribution is important in experiments with atomic clusters in general, since the detected signal may originate from different cluster sizes. Furthermore, in investigations focusing on nanodroplets isolation spectroscopy, it plays an important role in order to estimate the number of foreign atoms in the droplets, since the experimental data have to be analyzed with respect to the pick-up statistics.

2.2 Properties of helium nanodroplets

The properties of the helium droplets have been studied in detail, see examples in [60,67–70]. It has been found that helium droplets are stable for all size ranges. The binding energy of the atoms in the droplet changes from 1.1-1.3·10^{-3} K for He_2 [71,72] to 7.21 K for bulk liquid helium [73]. The binding energy per atom can be estimated as [73]:

$$\frac{E(N_{He})}{N_{He}} = -7.21 + 17.71 N_{He}^{-1/3} - 5.95 N_{He}^{-2/3} \text{ [K]} \tag{2.5}$$

Helium droplets are considered to have a spherical shape in the ground state. However, nonspherical shapes have been observed experimentally [44,74,75]. For subcritical expansion, some droplets carry angular momentum, which is transferred by inhomogeneities in the flow of liquid helium through the nozzle [76]. The rotation of the droplet induces centrifugal forces, leading to a change from spherical to a wheel-like shape. In the present work, the droplets are formed via gas condensation and assumed to be spherical. The droplet radius r_{drop} depends on N_{He} and can be calculated as

$$r_{drop} = r_0 \cdot N_{He}^{1/3} \tag{2.6}$$

where r_0=2.22 Å is the Wigner-Seitz radius of He. The particle density ρ_{He} of the nanodroplets is uniform up to the surface layer, where ρ_{He} drops drops from 90% to 10%, within a characteristic length of 6 Å [60], see Fig. 2.3. The internal pressure of the droplets could be calculated by the Young–Laplace equation:

$$P_{drop} = \frac{2\sigma_{He}}{r_{drop}} \tag{2.7}$$

where σ_{He}=0.35·10^{-5} N/cm is the the surface tension of liquid helium at T=0 K [77]. As an example, for N_{He}=1000, one can estimate that P_{drop}=3.2 bar, which is significantly lower than the pressure P_{solid} at which helium solidifies. Since P_{drop} is inversely proportional to r_{drop} and decreases with a droplet radius, the larger droplets are expected to be liquid as well.

The temperature T_{drop} of the droplets has been determined by rotational spectroscopy of embedded molecules and has a value of T_{drop} =0.37 K [23], which is well below the λ-line (Fig. 2.1), which defines the superfluid transition. The superfluidity of He nanodroplets has been demonstrated experimentally [29, 79]. Moreover, microwave
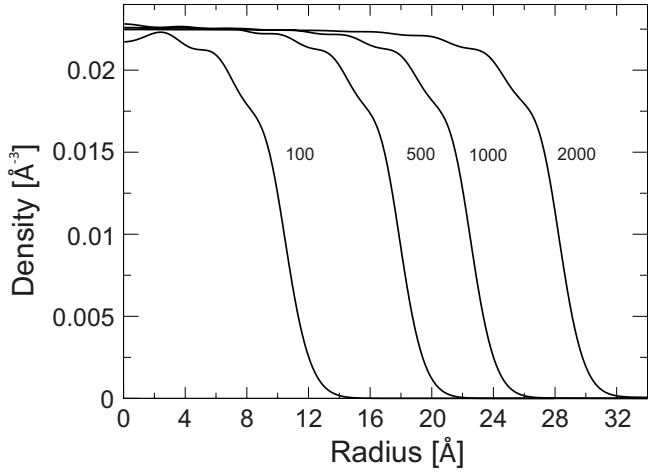
Figure 2.3: Radial density profiles of helium droplets with sizes N_{He}=100, 500, 1000, 2000 atoms. Adapted from [78].

spectroscopy of small molecule-helium clusters [80], demonstrated that even a few tens of atoms are sufficient for helium clusters to be superfluid.

An important property relevant for the present work is evaporative cooling, by which excess energy deposited into the droplet is released through evaporation of helium atoms. The cooling rate has a value of 10^{10} K·s^{-1} and follows an exponential decrease with temperature [6]. Around T=1 K the rate reaches value of 10^9 K·s^{-1} [67]. On one hand, such fast evaporation gives a great advantage, for spectroscopy of particles in the ultracold environment. Indeed, when any foreign particles with initial temperatures higher than T_{drop}, collide and coagulate within the droplet, they will rapidly lose their energy. At the end, the temperature of the impurity will be equal to T_{drop}. On the other hand, studies on He nanodroplets at temperatures higher or lower than 0.37 K are not possible.

Being liquid, the helium nanodroplets could undergo an elementary excitation such as surface vibrational and volume compression [67, 69]. The dispersion relations for this excitation can be obtained with the liquid drop model. The energy of the volume modes is

$$\omega_{vol} = q\sqrt{\frac{1}{k\rho_{He}m_{He}}} \tag{2.8}$$

where k is the compressibility parameter, ρ_{He} is the density of liquid helium, m_{He} is the mass of helium atom, and value q is determined by the boundary conditions and for the lowest excitation $q = \pi/r_{drop}$. It is possible to show, that the lowest excitation

Figure 2.4: Energy of volume and surface fundamental modes for different droplet sizes. The solid black line corresponds to E_{vol} according to Eq. 2.9. The dashed lines correspond energy of surface modes, according to Eq. 2.11, for υ=2 and 3. The dotted-dashed lines correspond to the evaporation energy (calculated by Eq. 2.5) and the droplet temperature. According to [6, 73]
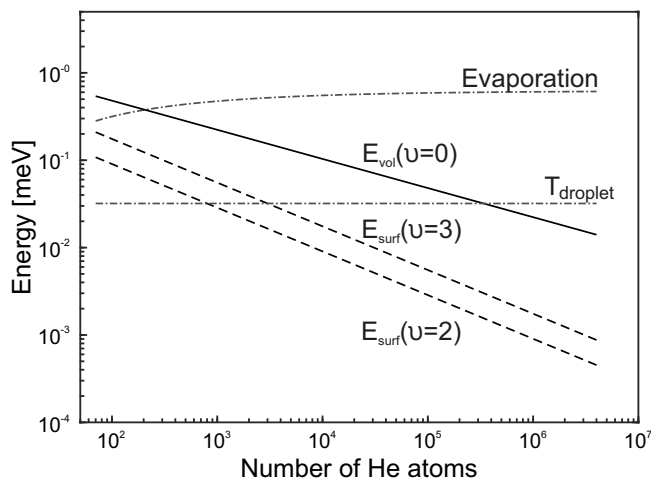
energy depends on the droplet size as [69]:

$$E_{vol} = \frac{18}{\sqrt[3]{N_{He}}}\ [\text{cm}^{-1}] = \frac{2.23}{\sqrt[3]{N_{He}}}\ [\text{meV}] \tag{2.9}$$

The energy of the surface oscillation modes (or ripplons) can be expressed as

$$\omega_{surf} = \frac{1}{\sqrt{N_{He}}}\sqrt{\frac{4\pi\sigma_{He}}{3m_{He}}\upsilon(\upsilon-1)(\upsilon+2)} \tag{2.10}$$

where σ_{He} is the surface tension of liquid helium and υ is the vibrational quantum number and $\upsilon \geq 2$. In the simplified form, the surface excitation energy can be calculated as [69]

$$E_{surf} = \frac{2.6}{\sqrt{N_{He}}}\sqrt{\upsilon(\upsilon-1)(\upsilon+2)}\ [\text{cm}^{-1}] = \frac{0.37}{\sqrt{N_{\text{He}}}}\sqrt{\upsilon(\upsilon-1)(\upsilon+2)}\ [\text{meV}] \tag{2.11}$$

The dependence of the lowest elementary excitation energies for both surface and volume modes on droplet size is shown in Fig. 2.4. It is clearly visible, that the volume modes cannot be excited in the droplets within the size range $N_{He} \leq 10^{6}$, since the energy of volume mode is higher than T_{drop}. On the other hand, when the size of the droplet exceeds the value of about 10^{3} atoms, the lowest excitation energy of the surface modes is well below T_{drop}, and therefore can be excited. Since the energies E_{surf} are relatively low, they do not affect the particles embedded in the droplets.

One of the fundamental aspects of superfluid helium are quantum vortices. Being proposed to exist in the droplets [81–83], a clear experimental verification of this phenomenon has been demonstrated only recently. First indications have been obtained in

experiments on the deposition of silver clusters formed in large droplets [76]. TEM [3] has shown that deposited clusters arrange along a line which has been interpreted as clustering along the vortex core. More recently, x-ray scattering experiments performed on large doped helium droplets have verified the presence of vortices [44]. The scattering patterns show characteristic features, which has been attributed to stem from vortex lattices. Both experiments showed that foreign particles enter the vortex core and stabilize within. The existence of such an intrigous quantum object on the nanoscale has pushed related experimental [84, 85] and theoretical investigations on pure [86, 87] and doped [85, 88, 89] droplets. Droplets which contain vortices have also been used as media to create and study one-dimensional chains (nanowires) of particles [90–94]. It is important to note, that all the experiments mentioned above, have been conducted on relatively large droplets ($r_{drop} \geq 200\,\text{nm}$). Evidence for similar structures in smaller droplets is still missing.

2.3 Doping of helium nanodroplets

As described above, the helium droplets are interesting and attractive objects for investigations. Their properties give a great advantage for using them as a cryogenic matrix. The possibility of embedding foreign particles was shown for example for noble gases [9, 10, 95], metals [12, 24, 96, 97] and molecules [15, 98]. With the capture of more than a single particle, it can be used as medium for cluster formation [31, 99–103].

In the experiment, the doping is realized via propagation of a droplet beam through a region filled with a dopant gas. Due to collisions, the dopant particles may be immersed into the droplets. This process is called pick-up and it can be described as a statistical process. The probability to pick-up k atoms by a droplet can be described by Poisson statistics [63, 104]:

$$P_k = \frac{\overline{N}^k}{k!} \cdot e^{\overline{n}},$$

(2.12)

where $\overline{N}$ is the mean of the distribution, and can be expressed as

$$\overline{N} = S \cdot n_{dop} \cdot L$$

(2.13)

where S is the droplet cross-section, n_{dop} is the particle density and L is the length of

---

[3]Transmission electron microscopy

pick-up region. The geometrical cross section of a spherical droplet is

$$S = \pi \cdot (2,22)^2 \cdot N_{He}^{2/3} \ \text{nm}^2 \tag{2.14}$$

Experimentally, the density of the particles is controlled by varying the partial pressure P_{dop} of the dopant gas in a pick-up cell. The particle density can be calculated as[4]

$$n_{dop} = \frac{P_{dop}}{k_b \cdot T_{dop}} \tag{2.15}$$

where k_b is the Boltzmann constant, T_{dop} is the temperature of the gas.

A pressure of about 10^{-6}-10^{-5} mbar is sufficient to pick-up a single particle. During the collision, energy and momentum of the foreign particle are completely transferred to the droplet, which leads to a rapid evaporation of helium. As a consequence, the particle cools down to the droplet temperature. Since the droplet is superfluid, dopants can freely move within. Thus, under high doping conditions, multiple particles can coagulate, forming a cluster. The binding energy released during the cluster formation is also transferred to the droplet, providing an additional contribution to helium evaporation. The total energy release during the pick-up can be calculated as

$$E_r = \langle E_{col} \rangle + E_{bin}^{He-dop} + E_{bin}^{dop-dop} + E_{int}^{dop} \tag{2.16}$$

where $\langle E_{col} \rangle$ is the mean collision energy, E_{bin}^{He-dop} is the binding energy between dopant and droplet and $E_{bin}^{dop-dop}$ is the binding energy between dopants when multiple particles are captured. The value of E_{int}^{dop} determines the internal energy of the impurity, i.e., rotational or vibrational, and it has to be taken into account for molecular species.

The last three terms in Eq. 2.16 are determined by the type of the impurity, whereas $\langle E_{kin} \rangle$ depends on the experimental conditions. For the collision of two particles, in the center of mass frame, the collision energy E_{col} stems from the kinetic energies of the helium droplet and dopant particle. In this case the collision energy:

$$E_{col} = \frac{1}{2} M (\vec{v}_{He} + \vec{v}_{dop})^2 \tag{2.17}$$

where $M = m_{He} \cdot m_{dop} / (m_{He} + m_{dop})$, with m_{He}, $\vec{v}_{He}$ and m_{dop}, $\vec{v}_{dop}$ mass and velocities of the droplet and dopant, respectively. For a uniform spatial velocity distribution of the

---

[4]This relation follows from the ideal gas law.
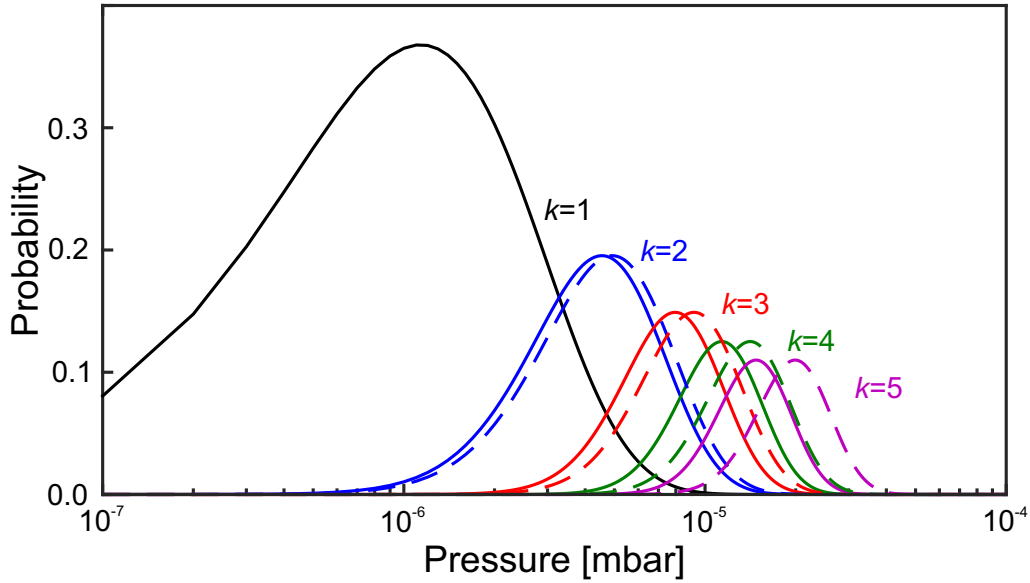
Figure 2.5: Probability of pick-up of k atoms with (solid lines) and without (dashed lines) evaporation of He atoms, calculated according to Eq. 2.12 as a function of gas pressure. For the calculation, a droplet size of $N_{He} = 36000$ atoms, a pick-up length of $L = 20\,\text{cm}$ and an evaporation rate of 1000 atoms per one dopant atom has been assumed

dopant particles and when $m_{He} \gg M_{dop}$, the average kinetic energy can be calculated as

$$\langle E_{col} \rangle = \frac{3}{2} k_B T_{dop} + \frac{1}{2} m_{dop} v_{He}^2 \tag{2.18}$$

and does not depend on the mass of the droplet. As an example, the collision energy for a droplet speed of $300\,\text{m/s}$ (subcritical condition) and Xe atoms at room temperature is $\langle \text{E}_{kin} \rangle = 160\,\text{meV}$.

The value of E_r determines the number of He atoms evaporated from the droplet upon doping. As a rule of thumb, 1600 atoms per $1\,\text{eV}$ excess energy can be used [6]. An example of pick-up probabilities for different numbers of impurities for a given droplet size with (dashed lines) and without (solid lines) evaporation are shown in Fig. 2.5. It is clear, that for a relatively high number of evaporated atoms (1000 atoms per particle), the pick-up up probabilities deviate. With the increase of the dopant load, the differences become stronger.

Alternatively, the number of picked-up atoms can be estimated by the method described in [105]. Assuming, that the pick-up probability scales with the droplet size as
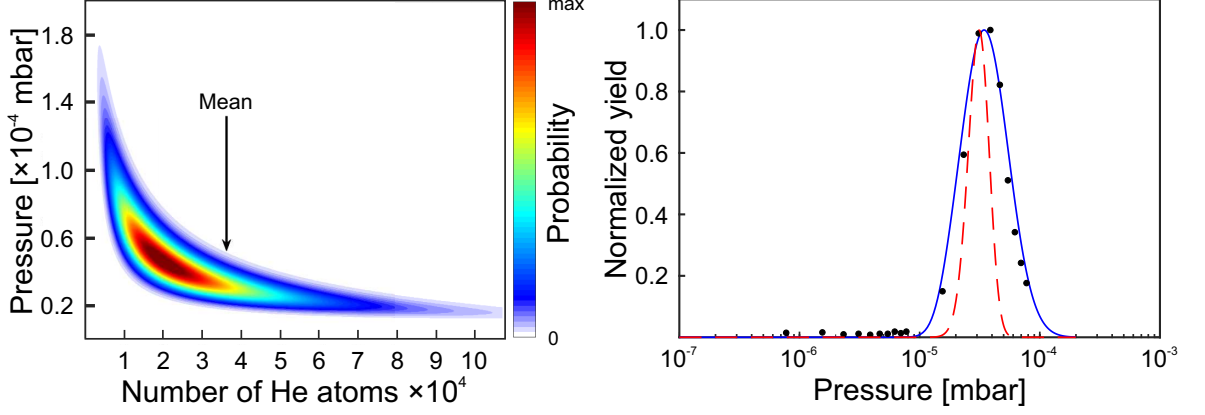
Figure 2.6: (left) Probability to pick-up k=25 atoms with respect to a log-normal distribution of droplets with $\overline{N}_{He}$=3.6·10^4. The probability is given by a color scale. The arrow indicates the position of the log-normal distribution. (right) The total probability to pick-up k=25 atoms by including all droplet sizes (blue solid line) and only for $\overline{N}_{He}$ (red dashed line). The black circles indicate the experimentally observed yield of Ar_{25}^+ ions as a function of Ar gas pressure.

$N_{He}^{2/3}$, the average number N_{dop} of dopants can be expressed as

$$dN_{dop} = \chi \frac{(N_{He} - cN_{dop})^{2/3}}{N_{He}^{2/3}} dp_{dop} \qquad (2.19)$$

where c is a constant, which determines the number of helium atoms evaporated per one captured impurity atom. The parameter χ is given by

$$\chi = \frac{S \cdot L}{k_b T} \cdot \sqrt{\frac{\langle v_{He}^2 \rangle + \langle v_{dop}^2 \rangle}{\langle v_{He}^2 \rangle}} \qquad (2.20)$$

where $\langle v_{He}^2 \rangle$ and $\langle v_{dop}^2 \rangle$ are the mean square velocities of the helium beam and the dopant gas, respectively. Integration of eq. 2.19 gives

$$N_{dop} = \frac{N_{He}}{c} \left(1 - \left(1 - \frac{c\chi}{3N_{He}} p_{dop} \right)^3 \right) \qquad (2.21)$$

This method gives an accuracy of the mean dopand size within ± 20 % [106].

Both methods can be applied to determine P_k for a single droplet size. In the experiment, however, droplets with different sizes are present. Therefore, it is required to apply the Poisson statistics to a helium droplets size distribution to achieve a better

agreement between estimated and experimental values [104]. For a given size distribution the pick-up probabilities strongly vary for different droplet sizes. In order to illustrate this, the probability to pick-up $k=25$ atoms by the droplets ($\overline{N}_{He}=3.6{\cdot}10^4$) is shown in Fig. 2.6, left. For droplets with $\overline{N}_{He}$ the optimal doping can be achieved in the narrow pressure range, whereas smaller droplets give a strong contribution to the doping probability at higher pressures. Fig. 2.6, right, shows experimental ion yield of Ar_{25}^+ as a function of argon pressure together with a total probability including all droplet sizes and the Poisson distribution for $\overline{N}_{He}$ only[5]. Clearly, the calculated pick-up dependence based on the full log-normal distribution gives a better agreement to the experiment.

Location of dopant particles

Capture and solvation of foreign particles by He droplet depend on the interaction between the species and helium. In general, impurities can be separated into two groups: so-called 'heliophobic' and 'heliophilic' [6], which can be traced back to the chemical potential μ. For example, μ is positive for alkali-metal atoms and thus they can be referred as 'heliophobic'. Such atoms are not solvated in the droplet interior, but reside on the surface forming a dimple, see [11, 24, 26, 107, 108] for experiment and [109–111] for theory. Other species, e.g., rare gases [10, 112], molecules [23, 113] and some metals [114–116] have a negative value of μ, and are located in the droplet interior.

For the prediction of the dopant location, Ancilotto *et al.* have provided a model based on the He-dopant interaction potential and macroscopic helium properties [117]. The position of an impurity is determined by a dimensionless parameter λ_A:

$$\lambda_A = \frac{1}{2^{1/6}} \cdot \frac{\rho_{He}\varepsilon r_{min}}{\sigma_{He}} \tag{2.22}$$

where ρ is the number density of liquid helium, σ is the surface tension of liquid helium, ε is the well depth of the interaction potential and r_{min} is the equilibrium separation distance. Examples of calculated λ_A for different elements are given in Tab. 2.1. For $\lambda_A < 1.9$ impurities are located on the surface, whereas for $\lambda_A > 1.9$ species are solvated. However, for the elements having λ_A close to 1.9 the assignment may be incorrect, since the shape of the interaction potential is not considered in the model [118]. A

---

[5]The experimental data are obtained by electron impact ionization of Ar doped droplets in present work.

Atom	ε, meV	r_{min},Å	λ_A	Location	Ref.
Ne	1,8	3,5	4,81	Inside	[120]
Xe	2,5	3,97	8,83	Inside	[120]
Na	0,15	6,06	0,80	Surface	[109]
K	0,12	6,76	0,71	Surface	[109]
Ag	0,93	4,6	3,76	Inside	[121]
Mg	0,61	5,1	2,73	Inside	[122]
Mg	0,96	4,7	3,96	Inside	[123]
Mg	0,28	5,7	1,4	Surface	[124]
Ca	0,43	5,9	2,23	Inside	[122]
Ca	0,41	6,02	2,17	Inside	[125]
Ca	1,28	5,1	5,7	Inside	[123]

Table 2.1: Ancilotto parameter λ_A calculated according to Eq. 2.22 for different elements. The values of helium density and surface tension are $\rho_{He} = 2,18 \cdot 10^{28} \, \text{m}^{-3}$, $\sigma_{He} = 3,54 \cdot 10^{-4} \, \text{N/m}$ respectively [126–128]. Values of ε and r_{min} are taken from the references given in the table.

prominent example is Ca, for which the interior locations are predicted for different Ca-He interaction potentials (Tab. 2.1), whereas the experiment gives evidence for a surface location of the atom [119]. The Ancilotto parameter strongly depends on the chosen He-dopant interaction potential, i.e., values ε and r_{min}. For Mg surface and interior locations can be predicted.

The Ancilotto parameter only predicts whether an atom is solvated or not. However, clusters of same atoms may have different solvation properties. Prominent examples of this phenomenon are Na$_N$ and K$_N$ clusters. Being alkali metal atoms, these elements are located on the surface of the droplet ($\lambda_A < 1.9$, see Tab. 2.1). It has been demonstrated, that few-atoms alkali clusters can be found on the surface as well [11]. Theory, however, predicts that beyond a critical size, clusters completely immerse into the droplet [129]. It has been shown, that the critical size increases with the mass of the element. Indeed, experiments have obtained a critical numbers of 21 for Na$_N$ and around 80 for K$_N$ in good agreement with theory [130, 131]. The immersion of initially surface located atoms can also be triggered by embedding of another element into the droplet [132].

Foreign atoms in the droplet have an impact on the helium environment. Due to the
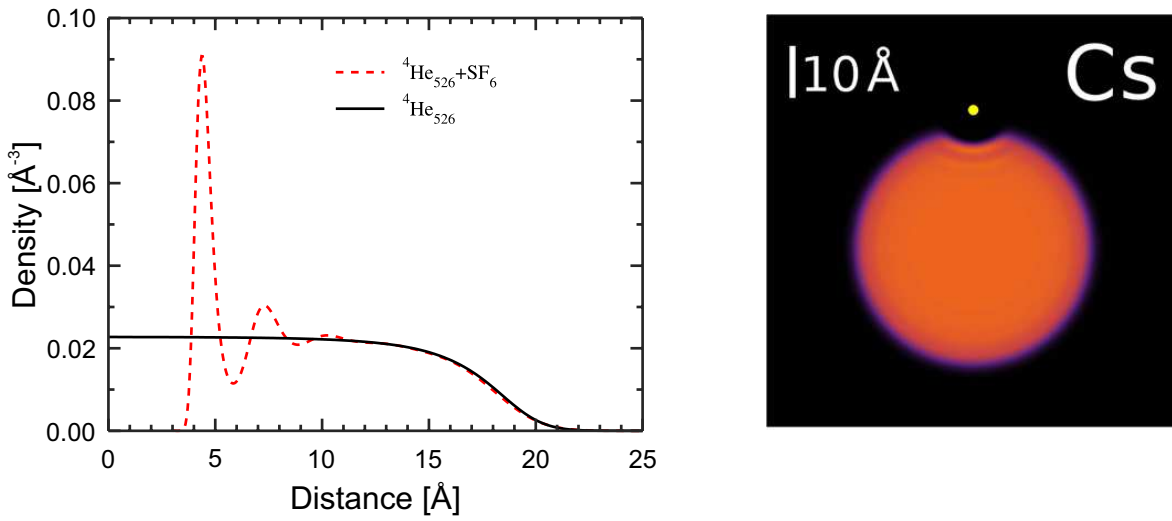
Figure 2.7: (Left) Calculated density profile of pure (black solid line) and SF_6 doped droplets (dashed red line). The presence of the impurity causes a density oscillation. (Right) Calculated two-dimensional density distribution of a droplet with an impurity located on the surface. Adapted from [78, 133]

van der Waals (vdW) interaction, helium atoms localize around the impurity [78, 113]. As an example, the calculated helium density in the vicinity of SF_6 molecule is shown in Fig. 2.7, left. The helium density around the impurity changes and forms solvation shells. For the surface located atoms, there is no complete spherical shell, but the atom resides in a so-called dimple state (Fig. 2.7, right), where only a part of the nearest He atoms are affected by the dopant [24, 107, 134].

3 Properties of particles attached to He droplets

Particles embedded in He nanodroplets are affected by the surrounding liquid helium, due to the dopant-helium interaction. For the present work, the change of the optical properties, for example, absorption, are of interest. Qualitatively, the behavior of the optical properties can be described by the standard bubble model. Besides the absorption, other effects may take place, such as a decrease of the ionization threshold. Upon the interaction of laser light with the dopant, the formation of dopant-helium complexes, as well as dynamical processes can be induced. In this chapter, a brief description of the optical properties of the impurities is given. At the end of the chapter, experimental and theoretical results on embedded Mg are summarized.

3.1 Standard bubble model

The optical properties of atoms and molecules in liquid helium differ from the gas phase. The atomic absorption resonance is blue shifted and asymmetrically broadened when compared to the free atom, whereas the emission line is narrow and shows up close to the free atom transition. The general features of the optical spectra can be explained in terms of the standard bubble model (SBM) [135]. The SBM has been originally proposed to explain the spectra of atoms and ions embedded in bulk liquid helium but also explains spectral features in nanodroplets.

Liquid helium creates a so-called 'bubble'-like defect around the impurity, due to the repulsive part of the vdW interaction of the dopant with surrounding helium. The energy state of the electron of the impurity-bubble system can be calculated as:

$$E_{tot} = \langle \psi_{tot} | H_{tot} | \psi_{tot} \rangle \tag{3.1}$$

where ψ_{tot} is the wave function of the system and H_{tot} is Hamiltonian which describes the interaction. By neglecting the many-body interactions, the Hamiltonian H_{tot} can be expressed as

$$H_{tot} = H_{He}^{pair} + H_{imp-He}^{pair} + H_{imp} \tag{3.2}$$
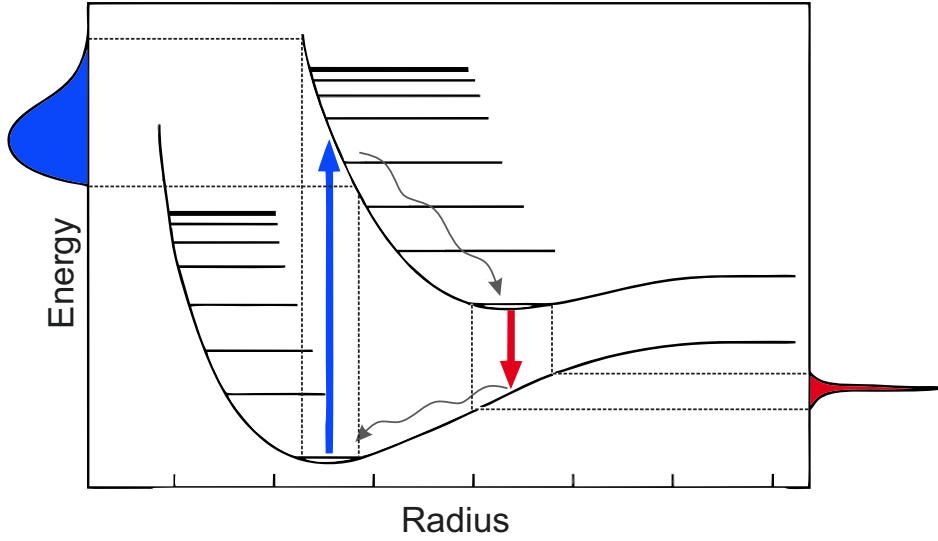
Figure 3.1: Schematic configuration diagram of an atomic impurity in a bubble defect in liquid helium. The blue arrow corresponds to an optical excitation from the ground into an excited state. The red arrow indicates the transition from the excited to the ground state. The typical shapes of absorption and emission spectra are shown on the sides of the diagram. Adapted from [135]

where H_{He}^{pair} and H_{imp-He}^{pair} describe the pair interactions between He atoms and impurity and helium atom, respectively. H_{imp} is the Hamiltonian of the free impurity itself. The energy shift of the impurity with respect to bare atoms can be expressed as:

$$\Delta E = \int U^{pair}(r) \cdot \rho(r) d^3r + E_{liq} \tag{3.3}$$

where $U^{pair}(r)$ is the pair interaction potential of the impurity and the helium atom, $\rho(r)$ is the density distribution around the bubble region, E_{liq} is the kinetic energy of the liquid in the vicinity of the bubble. The latter includes several components, such as surface energy, volume kinetic energy, and pressure volume work. A similar treatment can be applied to the excited state. Taking into account the Frank-Condon principle, the transition frequency shift can be expressed:

$$\Delta \nu = \frac{1}{h} \int (U_f^{pair}(r) - U_i^{pair}(r)) \rho(r) d^3r \tag{3.4}$$

where indices i and f corresponds to initial and final states, respectively.

The origin of the different shifts in emission and absorption is caused by the dissipation of energy into the surrounding helium. For a schematic view, Fig. 3.1 shows an energy diagram of the ground and excited state of an atom located inside liquid

helium. The He-dopant interaction differs in the excited state, which in general affects the equilibrium configuration and the size of the bubble. An electronic transition can be accompanied by bubble excitations. As a consequence of the Frank-Condon principle, the excitation energy shifts with respect to the gas phase, and the process ends up in an excited state of the bubble. Later, the bubble relaxes to its equilibrium configuration within a ps-time scale. For the emission, the transition is vertical and shifts only slightly relative to the free atom.

The SBM only gives a rough estimation about the shape of the spectral line, due to several reasons. The model does not include many-body interactions, the impact of the atomic state symmetry on the bubble shape is not taken into account. In addition, liquid helium is assumed to be a continuous, incompressible medium, and the description of the total energy is based on classical microscopic terms. In order to overcome these problems more sophisticated methods have to be considered [136–140]. Nevertheless, the SBM provides a helpful picture of the absorption and emission of impurities in liquid helium.

3.2 Particles in He droplets

Since the helium droplet isolation technique has been established, investigations have been focused on the properties of particles in the ultracold environment. This includes different experimental techniques, for example, mass spectroscopy (MS) [25, 31, 97, 141], photoelectron spectroscopy (PES) [32, 142–144] and laser induced fluorescence (LIF) [11, 12, 145], as well as theory [118, 146–149]. In the present work, the electronic and optical properties of Mg atoms and their complexes are in the focus. Therefore, most of this section concentrates on the features of a single embedded particle. The properties of Mg in helium nanodroplets will be discussed in the next section.

As it has been discussed in the previous chapter, the impurity could either reside on the surface of the droplets or be immersed inside. The location of the impurity has an impact on the optical properties. Similar to bulk liquid helium, a completely solvated atom creates a bubble state, which leads to blue-shift in the absorption spectra and an asymmetrical broadening. For example, the absorption spectrum of embedded Ag atom near the $5^2P_{1/2,3/2} \leftarrow 5^2S_{1/2}$ transitions is shown in Fig. 3.2, left. The absorption lines are shifted by 500-600 cm^{-1} (60-70 meV). The shifts vary for different elements, but in general are in a range between 10 and 100 meV [12, 115].

For atoms on the surface, the absorption is only slightly shifted in comparison to
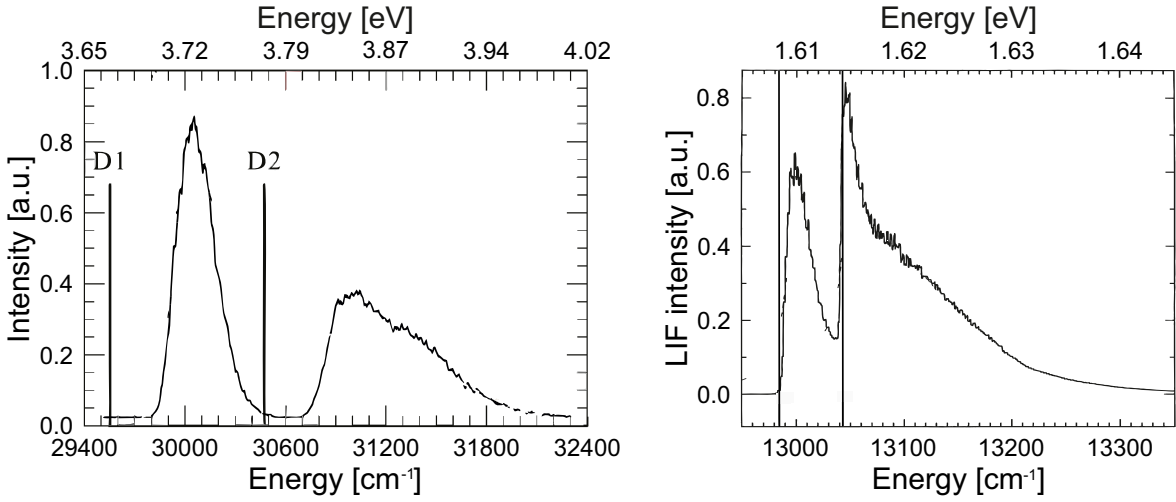
Figure 3.2: (left) Absorption spectrum of Ag atom in helium droplets in the vicinity of the D1 ($5^2P_{1/2} \leftarrow 5^2S_{1/2}$) and D2 ($5^2P_{3/2} \leftarrow 5^2S_{1/2}$) transition. (right) Absorption spectra of K atoms on helium droplets ($4^2P_{1/2} \leftarrow 4^2S_{1/2}$ and $4^2P_{3/2} \leftarrow 4^2S_{1/2}$ transitions). The solid vertical lines correspond to the free atom transitions. Adapted from [24, 150].

the completely solvated atoms. The reason is the weaker total He-dopant interaction, due to the lower number of helium atoms near the impurity. The shift depends on the pair interaction between the droplet and particle, as well as on the depth of the dimple. Moreover, the broadening could be extended even in the low energy part of the spectrum, due to the vibrational motion of the atom within the dimple [111]. As an example, the absorption spectrum of potassium atom is shown in Fig. 3.2, right.

The helium surrounding not only causes a modification of the electronic structure of the embedded particles. Another phenomenon is the reduction of the ionization potential of the dopant, which has been demonstrated for the first time by photoelectron spectroscopy on aniline doped droplets [151]. The kinetic energy of the photoelectrons emitted from the molecule inside the droplets is higher by about 100 meV compared to the gas phase. Moreover, the change of the value of the IP depends on the droplet size. This has been interpreted as a decrease of the vertical ionization threshold and attributed to polarization effects from the surrounding helium. The droplet radius dependence of the IP has been described as

$$IP(r) = IP_\infty - \frac{e^2(1 - \epsilon_{He}^{-1})}{8\pi\epsilon_0 r} \tag{3.5}$$

where IP_∞ is the IP in bulk liquid helium, ϵ_0, ϵ_{He} are the dielectric permittivity of free

space and helium droplet, respectively, e is the elementary charge. Similar effects have been observed in pure droplets [152], where the photoelectron peaks show a shoulder towards higher kinetic energies, i.e., indicating a decrease of the IP compared to the atom. The change of the IP of surface located atoms has been observed for alkali doped droplets. The shifts were found to be in the range of about 5 meV for Rb and Cs [153], 14 meV for Li [154] and 15 meV for Na [33]. For Ba doped droplets, the direct ionization of the atoms shows a shift of 25 meV, while in the ionization through an intermediate state, the observed shift is only 12 meV [155]. This effect has been attributed to the change between the Ba-He interaction for the excited state compared to the ground state. In the excited state, the system undergoes a relaxation to the equilibrium configuration before the second photon is absorbed. The rearrangement of helium around the dopant leads to a configuration which is different to the ground state and, thus, has an impact on the value of the IP shift.

The ionization of particles in helium droplets does not only produce impurity ions but also leads to the formation of dopant-He_n exciplexes or 'snowballs', which can be observed by mass spectrometry [8, 156, 157]. These structures consist of a positively charged particle with attached He atoms, as a result of the strong interaction between the He atoms and positive ions. An example is shown in Fig. 3.3. Moreover, it has been found that similar structures can be produced not only by ionization but also after excitation, if the interaction of the excited particle with He is attractive [158]. The formation of snowballs has to be taken into account in REMPI[1]-PES when the time delay between excitation and ionization is sufficient for exciplex formation. This will reflect in the photoelectron spectra, since the detected electrons may originate from all neutral particles. The number of attached He atoms may also serve as an indicator for the location of the impurity in the droplet. Snowballs formed from a dopant on the surface contain only a few atoms, whereas for solvated particles, the snowball size is expected to be large [156].

Excitation and ionization of atoms attached to droplets can also drive dynamics. One of the prominent examples is the desorption of alkali atoms upon the photoabsorption [108, 133, 154, 160–162], due to the repulsive interaction between the excited alkali atom and the droplet. A similar situation may also take place for embedded atoms, like, Ag and Cr [27, 115, 150, 163, 164], where after the photoexcitation, atoms are expelled from the droplets. Note that the analysis of kinetic energies of expelled Ag atoms has been used to reveal the Landau critical velocity in nanodroplets [165]. The ionization of the

---

[1]Resonance-enhanced multiphoton ionization
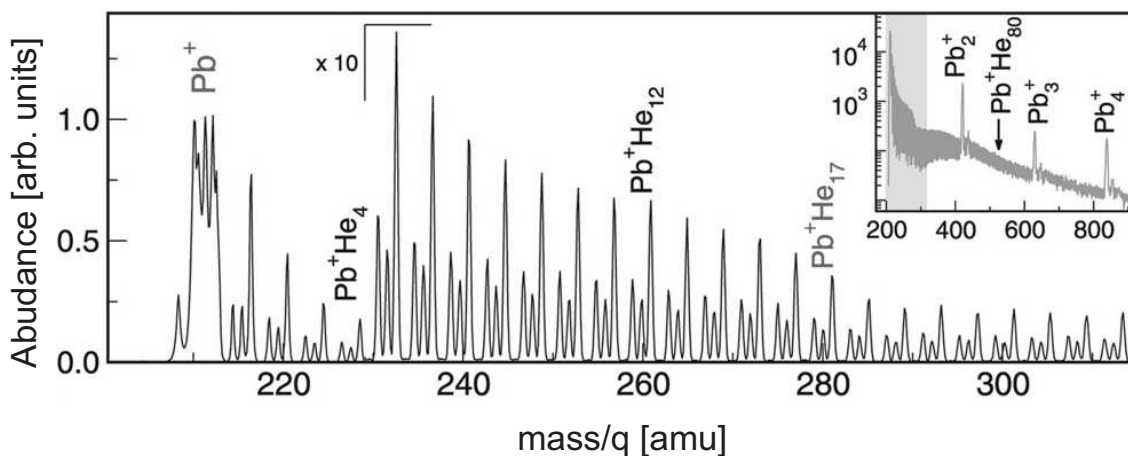
Figure 3.3: Mass spectrum of lead clusters in helium droplets after femtosecond ionization. Prominent signals of Pb^+He_n snowball complexes are visible together with Pb_m^+ clusters. From [159].

surface located species may also lead to the opposite process, e.g. immersion of atoms into the interior of the droplets [166, 167].

Besides atoms, helium droplets can serve as an ultracold matrix for studies on molecules, e.g., rotational and vibrational spectroscopy [15,30,168,169], electronic spectroscopy [170–173], LIF-spectroscopy [105, 174], studies on solvation properties [175], dissociation dynamics [176–178] and properties of molecular clusters [179, 180]. Rotationally resolved IR spectroscopy of embedded OCS molecules has been used to reveal the temperature of the droplets, i.e., 0.37±0.05 K [23]. The superfluidity of helium nanodroplets has been probed by conducting experiments on OCS-doped droplets as well [29]. It has been found, that in the IR absorption spectrum, rotational lines show only a minor shift and a small broadening compared to the gas phase and has been interpreted as almost free rotation (with very weak interaction of the molecule with helium), giving evidence for the superfluid nature of helium even at the nanoscale.

Helium nanodroplets may serve as a medium to create structures which cannot be formed by the other methods. An illustrative example is an observation that polar molecules arrange as a long linear chain [46], which is not the lowest-energy configuration in the gas phase. Recently, evidence for the formation of the linear configuration of OCS trimers has been observed in laser induced alignment experiments [181]. Another example of a unique molecular structure is cyclic water hexamer, representing the smallest ice structure [47]. Alkali clusters on the surface of the helium droplets [48,182,183] are formed in high-spin states, since for the low-spin configuration, the release of bind-

ing energy is high and leads to a strong evaporation of helium, which reflects in the desorption of the alkali clusters. The energy release in high-spin states is significantly lower and therefore clusters remain on the surface.

Recently it has been shown, that dopants located on the surface and in the interior of the droplet do not form clusters, but find each other as separated atoms [49]. In particular, upon the pick-up of Rb and Sr, SrRb molecules are not formed, but Rb is located on the surface of the droplets and Sr is solvated. The formation of RbSr is possible by the excitation of Sr, which enhances the interaction between the atoms. This triggers the motion of the atoms towards each other, and finally creating the SrRb molecule. Besides these examples, another unusual structure could be formed by doping the droplets by Mg atoms.

3.3 Magnesium in helium droplets

Magnesium is an alkaline earth element of the 2nd group of the periodic table. These elements have two valence electrons in the closed electronic s-shell. The Mg ground state electronic configuration $3s^2$ corresponding to a singlet 3^1S_0 state. The corresponding binding energy is 7.64 eV, which also determines the ionization potential (IP). Like in the other alkaline earth metals, the excited states are grouped by singlet and triplet configurations. A simplified level scheme is shown in Fig. 3.4. The two lowest lying excited states are triplet $3^3P_{0,1,2}$ and singlet 3^1P_1, having the binding energies of 3.3 eV and 4.93 eV, respectively [184]. The transition $3^1P_1 \leftarrow 3^1S_0$ is optically allowed, whereas the intercombination transition $3^1P_1 \leftarrow 3^3P_{0,1,2}$ is forbidden by selection rules. But for the alkaline earth metals, starting from Mg the probability of the latter transition is non-zero and increases for heavier atoms. The energy of $3^1P_1 \leftarrow 3^1S_0$ transition is 4.35 eV, which can be used to realize a single wavelength resonant two-photon ionization (R2PI) scheme, since the sum energy of two photons is higher than IP.

Besides the single electron excitation, doubly excited states can also be observed in Mg [185]. For example (see Fig. 3.4), absorption of a 4.25 eV photon by Mg atom in the $3s^13d^1(1^1D_2)$ state leads to the excitation into $3p^13d^1(^1D_2^o)$ level [184]. The doubly excited states form a new group of levels, which merge to the new ionization threshold, which is excited state of the ion.

Being embedded in helium droplets, Mg atoms shows specific properties. Experiments have been carried out on the spectroscopy of Mg atoms and clusters in helium
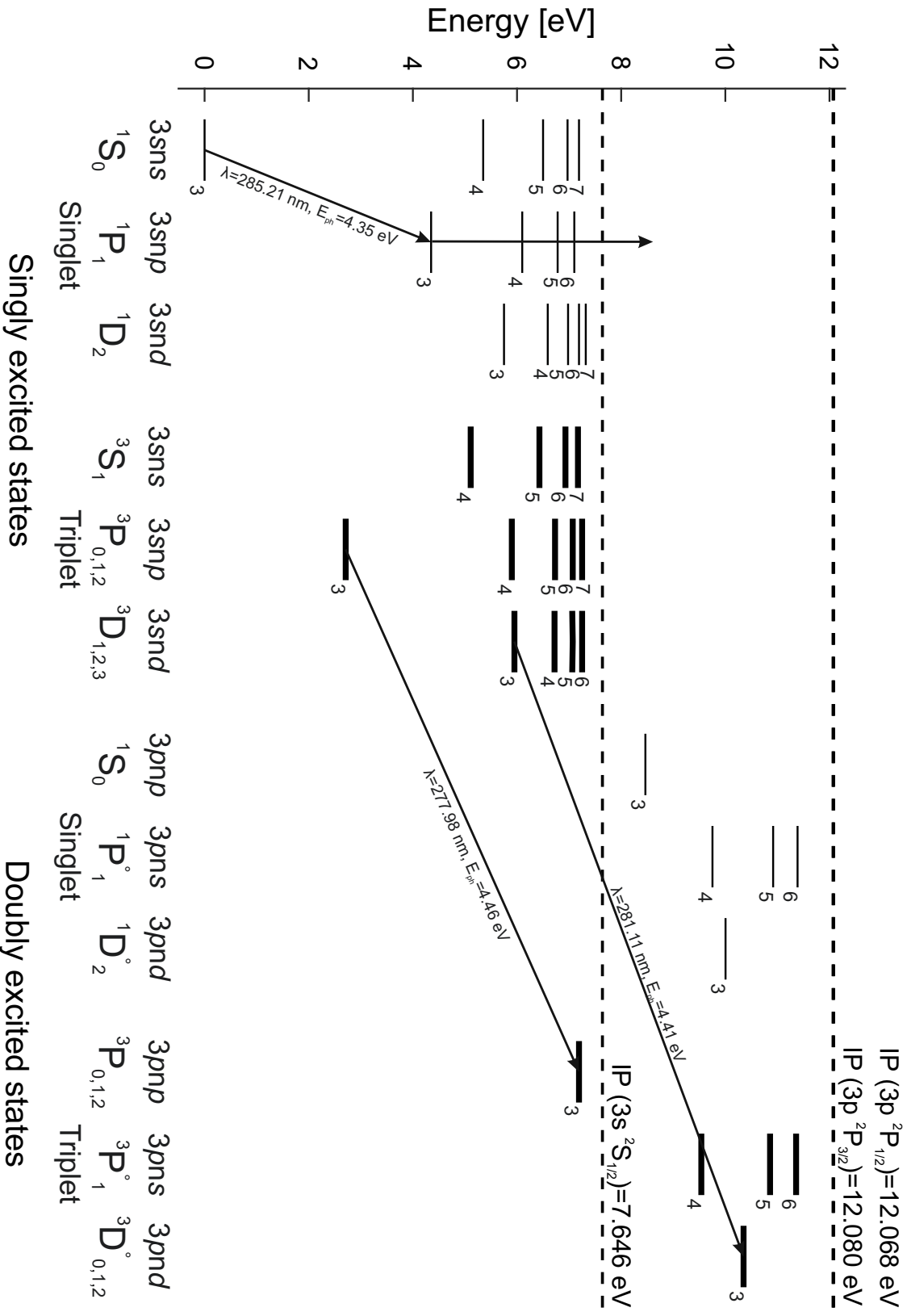
Figure 3.4: Energy level diagram of Mg. Singlet and triplet S, P, and D single and doubly excited states are shown. The arrows indicate transitions important for the present work. Excited states and transition energies, as well as values of IP, are taken from the NIST database [184].

Figure 3.5: LIF spectra of Mg atoms in bulk liquid helium (black solid line) and helium droplets (red dashed line). The dotted line corresponds to the free atom transition. Adapted from [186, 190, 193].
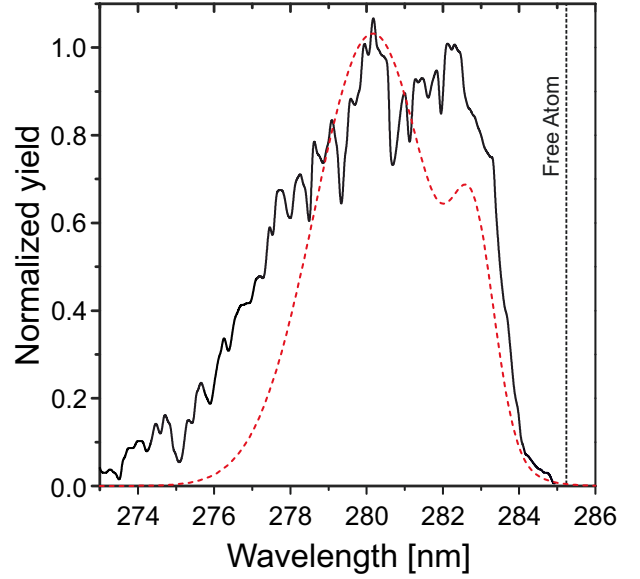
droplets [35, 51, 186–189] and in bulk liquid helium [190, 191]. First investigations of Mg-doped droplets have been conducted by Reho *et al.* [186]. In these experiments, the excitation spectra close to the $3^1P_1 \leftarrow 3^1S_0$ atomic transition (wavelength λ=285.2 nm, photon energy E_{ph}=4.35 eV) have been studied by LIF. A broad absorption (full width half maximum (FWHM) of 82 meV) blue-shifted by about 80 meV relative to the bare atom transition has been observed. Moreover, the shape of the spectral line exhibits a double peak structure, with centers at λ=283.1 nm and λ=279.1 nm, see Fig. 3.5. The lifetime of the excited state was found to be about 20% longer, relative to the free atom value. The spectral shift and increase of the lifetime have been attributed to the interior location of Mg in the droplet. The shape of the spectrum has been explained in terms of quadrupole deformation of the bubble surrounding the impurity, which arise from the non-symmetrical electron distribution of 3^1P_1 state. The findings are in good agreement with investigations on Mg in bulk liquid helium [190, 191], where the line shape, as well as the spectral shift, show a similar order of magnitude. The peak position, however, differs from the theoretical SBM calculations [146] and quantum Monte-Carlo simulations [192], where the absorption has a single peak at 278.3 nm and 279.9 nm, respectively.

Przystawik *et al.* [51] utilize R2PI in combination with mass spectrometry in order to reveal the absorption spectrum. In contrast to LIF, the R2PI and mass spectrometry technique has an advantage, since different products of the ionization can be monitored selectively. An example of a mass spectrum is shown in Fig. 3.6. The spectrum contains
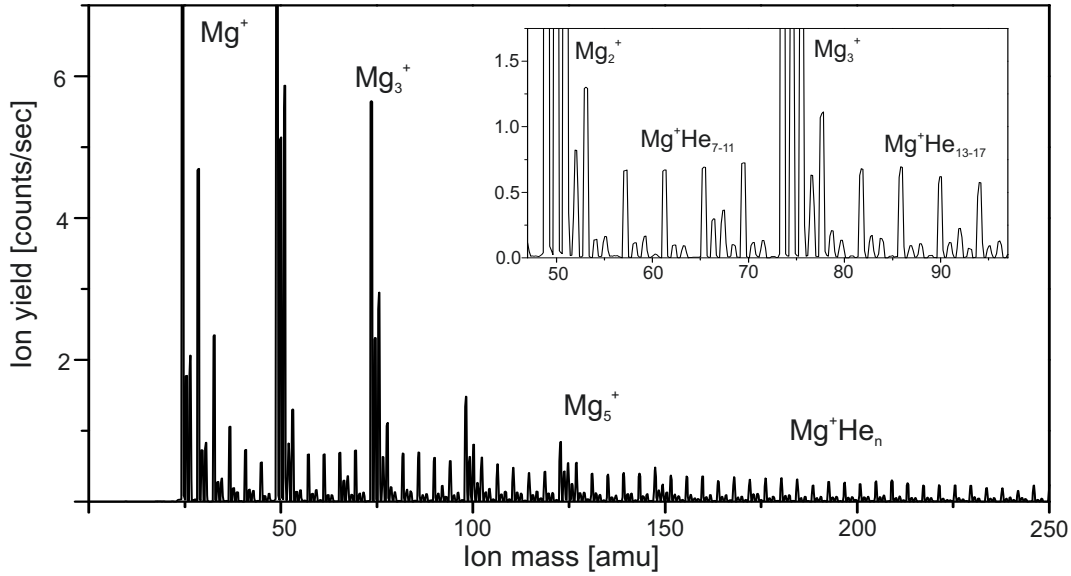
Figure 3.6: Mass spectrum of Mg in helium droplets ($\overline{N}_{He}$=6·10^3), ionized by R2PI at $\lambda_{laser} = 276$ nm. Besides the atoms and clusters, a prominent signal of MgHe$_N$ snowballs is visible, which extends up to $N \geq 50$. Adapted from [194].

signals from Mg$^+$ atom, Mg$_N^+$ and Mg$^+$He$_N$ snowballs, with N extending to values of more than 50. The absorption of Mg doped droplets has been investigated in the wavelength range between 276-286 nm and for different doping conditions, i.e., as a function of $\overline{N}_{Mg}$. The main findings can be summarized as follows:

(i) The atomic spectra have been monitored by MgHe$_{50-53}^+$ ion signal, which were assumed to be produced only in the droplet interior, see Fig. 3.7, left. At low doping conditions, $\overline{N}_{Mg} = 0.1$ (only single atom), absorption has a single blue-shifted and broadened peak centered at 279 nm. The shift of the spectrum agrees well with theoretical predictions [146, 192]. With increasing number of atoms ($\overline{N}_{Mg} = 2$), the spectrum changes and shows a second peak, located closer to the free atomic transition. With the further increase of the doping level, the peak at 279 nm vanishes and only the second peak remains.

(ii) The signal of cluster ions (Mg$_N^+$, $N \geq 2$) shows a similar response as the Mg snowballs at high doping conditions and remains the same up to at least Mg$_{15}$, see Fig. 3.7, right. This result shows that *all* magnesium clusters in the range 2-15 exhibit the same absorption spectrum. This is different from the well-known size-dependence of small particles and nanoclusters [195] in general and calculated absorption spectra of Mg clusters in particular [196].
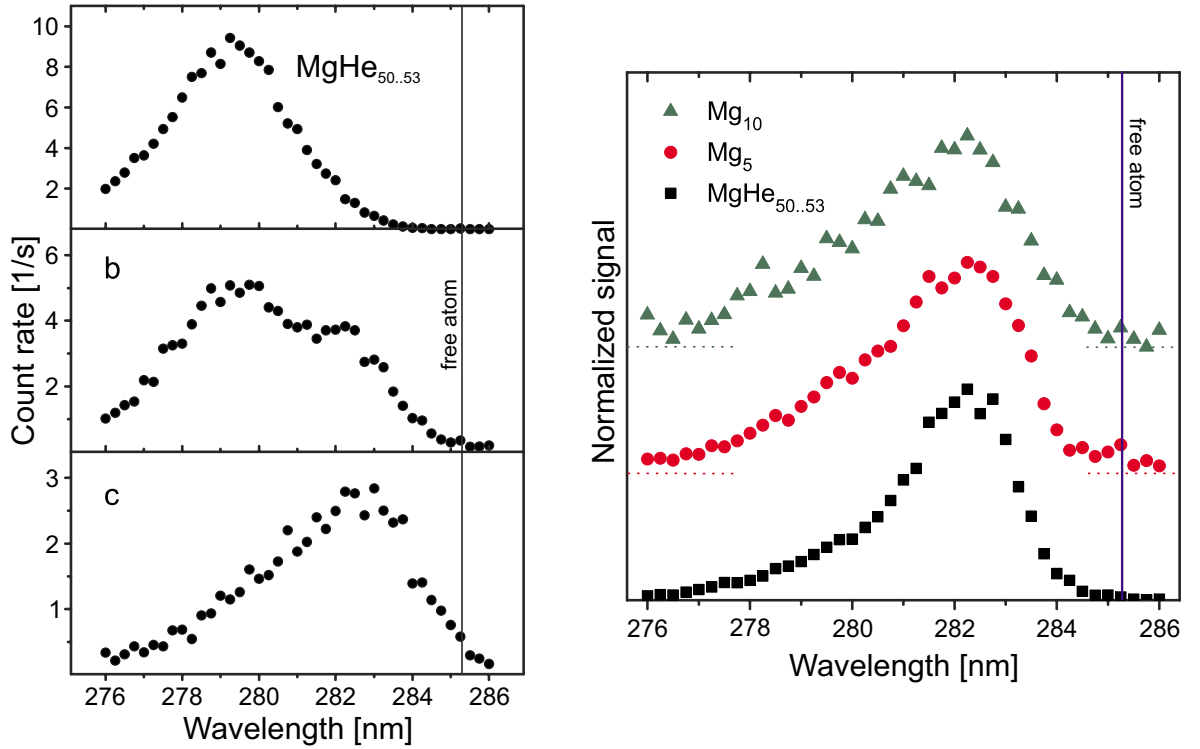
Figure 3.7: (left) R2PI spectra of Mg embedded in He droplets with size $\overline{N}_{He}$=6000. (a) For low doping conditions ($\overline{N}_{Mg}$<1), a single absorption peak centered at about 279 nm is obtained; (b) $\overline{N}_{Mg} = 2$, an additional absorption feature shows up at 282 nm; (c) $\overline{N}_{Mg} = 4$, only the peak at 282 nm is present in the spectrum. (right) R2PI spectrum obtained by monitoring the yield of clusters with different sizes, compared to the signal obtained from snowball ions. All selected spectra are similar to MgHe$_N$ (left panel, bottom). Adapted from [51]

(iii) Both of these findings lead to the conclusion, that instead of compact clusters, Mg atoms form a metastable network of isolated atoms separated by a layer of helium. This reflects in the absorption spectrum, which shows a single-atom like response. The shift of the spectral line compared to the single atom is caused by the interaction between the Mg atoms. Additional evidence has been provided by the calculated potential energy curve of two Mg atoms in liquid helium (Fig. 3.8, left), which shows a potential well at a distance of about 10 Å. Despite the fact, that the depth is only 4 K, the temperature of the droplet (0.37 K) and fast thermalization of the impurity after the pick-up, allow for a stabilization of Mg in the loosely bound structure. The separation distance of 10 Å is about 3 times larger than in the free Mg dimer [197]. The interplay between Mg-Mg and Mg-He interactions leads to the formation of a network
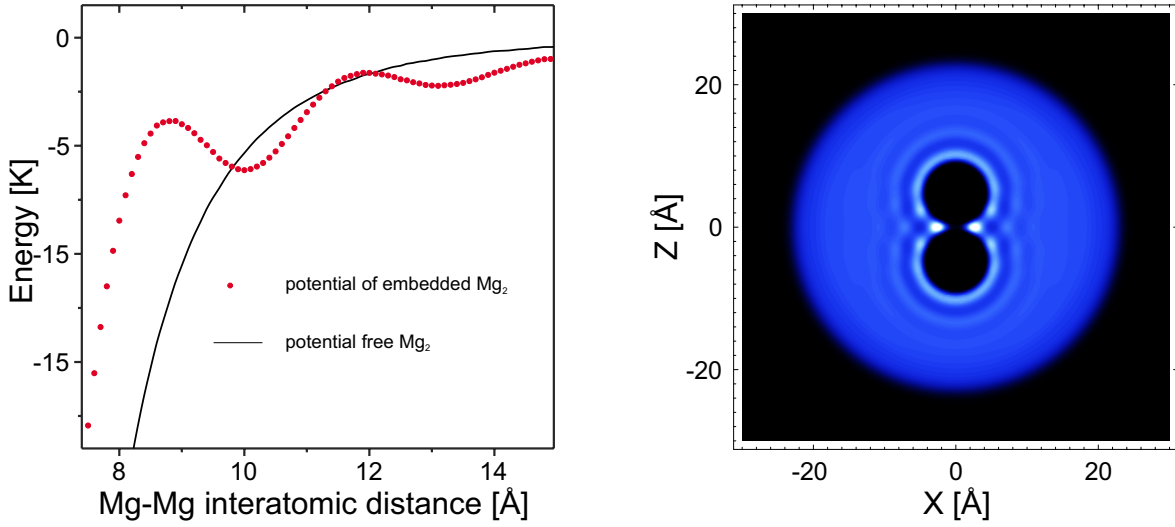
Figure 3.8: (left) Interaction potential of two Mg atoms. The black solid line corresponds to the free Mg dimer. Red dots is the calculated potential of two atoms in the presence of liquid helium. Note that in the latter case, the potential is changing, showing a prominent minimum at a distance of 10 Å. (right) Helium density around two Mg atoms calculated by DFT. Both atoms are separated by a layer of helium and surrounded by solvation shells. Adapted from [51, 149].

of separated atoms, i.e., a *foam*.

Later, driven by the experiments, the existence of this structure has been confirmed by Hernando *et al.* by DFT simulations [149]. The authors simulated the configuration of two Mg atoms within small droplets ($N_{He} = 1000$). They also reported about the presence of an energy barrier, which prevents the formation of a compact magnesium dimer. The estimation of the mean lifetime of the structure, gives a value up to 0.1 ms, depending on the initial angular momentum of the system. In contrast to DFT, recent theoretical investigation provided by the path-integral method [198] showed no evidence of a metastable network formation beyond two Mg atoms. Therefore, a final theoretical picture is still missing.

The experimental findings in [51] are supported, when potential curves of the ground and excited states of free Mg dimer are taken into account. The structure of the $X^1\Sigma_g^+$ ground and $A^1\Sigma_u^+$ excited states of free Mg_2 has been obtained with high precision, by the combination of a photoassociation with Fourier-spectroscopy [197, 199]. The values of the interatomic distances of around R_{gr}=3.9 Å, R_{ex}=3.1 Å and potential depths E_{gr}=50 meV, E_{ex}=1.17 eV have been obtained for ground and excited states, respec-

tively. The $A^1\Sigma_u^+$ excited state is relevant, because the $X^1\Sigma_g^+ \leftarrow A^1\Sigma_u^+$ transition is responsible for the absorption in the photon energy range used in the Mg foam experiments. In the wavelength region 276-285 nm, photoabsorption will lead to the excitation in high rovibrational levels of the $A^1\Sigma_u^+$ electronic state lying close to the dissociation limit. One can expect that the probability of this transition is low, due to the Frank-Condon overlap. According to the potential energy curves, more probable transitions would take place at photon energies at least 0.5 eV lower (about 3.8 eV) than used in the droplet experiments (around 4.35 eV). Even if the probabilities of transitions to high rovibrational states are still significant enough, the absorption spectrum, nevertheless, should extend with increasing a Frank-Condon factor and therefore will be reflected in the broadening of the absorption line deeper in the low energy region, with the width comparable to depth of potential curve (about 1 eV). In contrast to this, no absorption has been observed at the photon energies lower than 4.3 eV. Moreover, no vibrational structure has been observed in the absorption, even when the photon energy steps in [51] were low enough (about 3 meV) comparable to the vibrational quanta (about 24 meV).

An additional feature of the Mg foam is attributed to the dimensions and the growth process. Opposite to large $MgHe_n^+$ snowballs, the small snowballs and $MgHe^+$ in particular have a different line shape [193], see Fig. 3.9. The peak is located close to the free atomic transition and broadens towards shorter wavelengths. This has been assigned to Mg atoms located at the droplet surface. When the number of Mg atoms in the droplet is large, the dimension of the foam may be in the order of the droplet size. Thus, a part of the atoms could reside close to the droplet surface. In this case, the absorption spectrum should have a similar structure to the surface located atoms (see Fig. 3.2), which was observed indeed (Fig. 3.9, red). Another possible origin of a surface location of Mg atoms is a non-symmetrical growth of the foam.

The fragile equilibrium between the foam atoms may be destroyed by small perturbations, e.g., by photon absorption and will lead to a rapid collapse of the foam. The dynamics of the foam collapse has been studied by pump-probe experiments with femtosecond NIR[2] laser pulses [189]. The chosen laser intensity of 10^{11} W·cm^{-2} implies condition for multiphoton ionization (MPI). Two different schemes have been applied: (i) Direct ionization by a strong pump pulse and a weaker probe pulse; (ii) The weak pump pulse was utilized for the photoexcitation of the foam, whereas the strong probe pulse ionizes the atoms. In both cases, a strong enhancement of the ion signals has been

---

[2]NIR - near-infrared
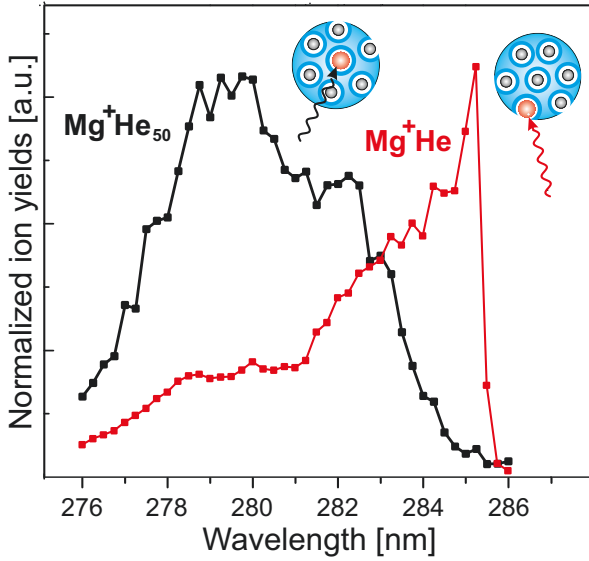
Figure 3.9: R2PI spectra of Mg doped droplets monitored at Mg^+He_{50} and Mg^+He snowball channels. Comparable to large snowballs, Mg^+He shows a response similar to that of surface located atoms. Adapted from [193].

observed near the zero delay. From these features, the timescale of the collapse was estimated to be in the range of ps, with a characteristic time constant of τ_{col}=350 fs. At longer time delays, in case (i) no specific time dependence of the ion signal has been observed. Ionization by the leading pulse increases the yields of Mg_n^+ and $MgHe_N^+$ fragments, but the efficiency of the ionization by the second pulse is low. Whereas for (ii), the drop in the ion yield has been observed, indicating that initial photoexcitation leads to the formation of compact neutral clusters by the collapse with subsequent ionization of them by the probe pulse. The decrease in the ion yield has been addressed to decreasing of the MPI probability for the compact cluster relative to the foam.

The results obtained in [51] (see Fig. 3.7), are not in contradiction with the LIF studies (Fig. 3.5) [186, 190]. In the bulk helium experiments, the authors applied laser ablation from a Mg target located inside the liquid helium. This method provides only a rough control on the number of atoms deposited into the medium. Thus, the LIF signal may contain contributions of single or multiple atoms and clusters, which cannot be separated. In the droplet experiments, the number of pick-up atoms can be controlled by the partial pressure of the dopant. Taking the experimental parameters from [186], i.e. pick-up length L=25 mm, pick-up pressure $P_{Mg} = 10^{-2} - 10^{-1}$ Pa, and the droplets size range $N_{He} = 10^3 - 10^4$ atoms, one can estimate the minimum mean number of atoms in the droplets. From Eq. 2.13 and using upper and lower limits for P_{Mg} and N_{He}, a value of $\overline{N}_{Mg} = 0.4 - 20$ can be obtained. The exact experimental conditions are not described, but even at $\overline{N}_{Mg} = 1$ the probability to pick-up several particles is significant. Therefore, one can expect, that in addition to single atoms, a

foam also contributes to the signal.

All the results obtained for small Mg ensembles in droplets are not in contradiction to the early studies on Mg clusters in nanodroplets [187, 188, 200]. In these experiments, electronic shell effects, as well as the interaction of Mg doped droplets with strong femtosecond laser pulses were under investigation. Since non resonant-enhanced ionization in strong fields or electron-impact ionization (EII) were applied, the signals of Mg clusters have been observed, whereas the signatures of the foam may be covered. Besides this, another possibility arises from direct ionization of the pure Mg clusters formed in spontaneous collapse of the foam. This situation will be addressed later.

4 Shell structure and ionization potential of atomic clusters

Atomic clusters[1] represent a specific form of matter, being intermediate between single particles and bulk material. In general, clusters consist of a countable number of atoms, starting from more than two and up to several thousands of consistuents [195,201]. Apparently, the physical properties of clusters depend on the chosen element. For example, rare gas cluster will show different behavior compared to the metal ones. In addition, the studies on clusters are appealing, since the size of the system has an impact on physical and chemical properties. Each additional atom counts, affecting on cluster characteristics. Examples are ionization potential (IP) [202], electron affinity (EA) [203], electronic [204] and magnetic [205] properties, cluster geometry [206], etc. On the other hand, in the limit of a large number of constituents, the cluster properties should converge to the corresponding characteristics of bulk.

As an example for the size dependence, mass spectra of Xe_N and Na_N are shown in Fig. 4.1. Clearly, clusters with specific sizes are more abundant in the spectra. This indicates, that clusters with specific sizes either are more stable and, thus, more abundant, or they show especially large or small ionization cross section. The numbers of atoms which correspond to more abundant sizes are called 'magic numbers'. However, the origin of these features are different for Xe_N and Na_N.

The binding of atoms in xenon clusters is caused by vdW interaction. The magic numbers in vdW clusters are attributed to geometrical structure, i.e., the most stable clusters have a closed geometrical shell. The most pronounced peaks at 13, 55, 147 agree well with the number of atoms in closed-shell Mackay icosahedra [207,208]. That is

$$N(i) = 1 + \sum_{k=1}^{i}(10k^2 + 2) \tag{4.1}$$

where i is the number of icosahedral shell. The Mackay icosahedra represent non-

---

[1]Cluster may also be formed from molecules. In this chapter general properties of clusters will be discussed using atomic clusters as an example.
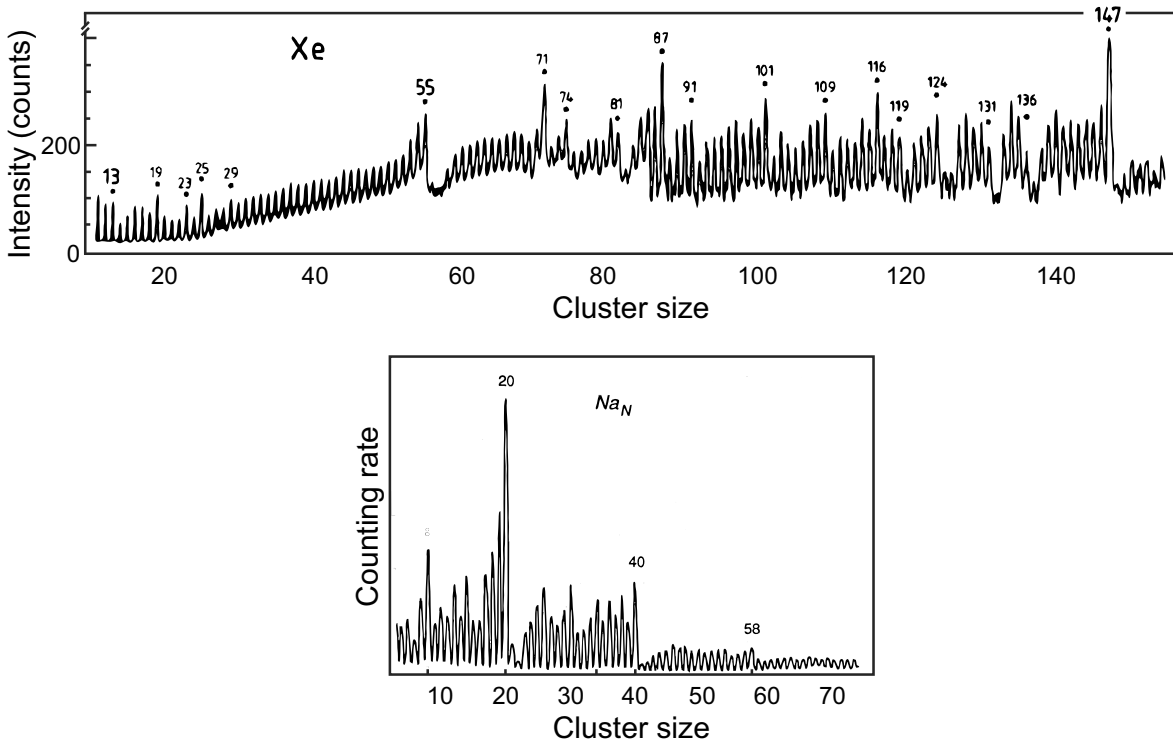
Figure 4.1: Mass spectra of Xe_N (top) and Na_N (bottom) clusters. Magic numbers are indicated. Adapted from [204, 207].

crystalline structures, i.e., it cannot be obtained as a cut from a crystalline piece, being fcc[2] for solid noble gases. The reason is related to the minimization of cluster total energy, which can be divided to volume and surface contributions. In small clusters, atoms located on the surface give a significant contribution to the total energy [206]. Among the different morphologies, the icosahedra structure has the lowest fraction of surface atoms [209]. This is valid at least to cluster sizes up to 10^5. With increasing size the geometry modifies to, e.g., cuboctahedral. The presence of peaks in addition to the main magic numbers has been assigned to the partial closing of shells, e.g. for $N=19$, the icosahedron with $N=13$ and a cap of 6 atoms. This is also reflected in the minimal total energy and therefore in enhanced structural stability. Note that besides noble gas clusters, evidence for geometrical shells have been observed for clusters of other elements, for example, small Ba and large Mg and Ca clusters [210–212].

In the case of Na_N, magic numbers have been observed as well (Fig. 4.1, bottom), that are 8, 20, 40, 58. These features differ fundamentally from the magic numbers

---

[2]Face Centered Cubic

observed in noble gas clusters and have been assigned to electronic shells, i.e. instead of closed geometrical shells, the most abundant clusters have a closed electronic shells [204]. The effect of electronic shell closing has been observed for cluster of other elements [9, 213–217]. Besides electronic shells, geometrical shell closing may also take place. For example, the evidences for the transition from electronic to geometrical shell closing has been observed in Na_N and Al_N clusters [218–220]. Moreover, both electronic and geometrical structures can affect on the properties of small clusters [221, 222].

Electronic shell structure

The experimentally observed magic numbers of Na_N clusters can be explained within a semi-empirical model, based on the assumption, that valence electrons are confined in a spherical potential [204]. In the case of Na the Wood-Saxon potential gives a good agreement with the experiments:

$$U(r) = -\frac{U_0}{1 + e^{(r-r_0)/\eta}} \tag{4.2}$$

where U_0 is the potential depth, r_0 is the effective radius of the cluster, η is the parameter which determines the variation of the potential at the edge of the cluster sphere. The solution of the Schrödinger equation gives discrete electronic levels, which are characterized by the radial quantum number n and the angular momentum ℓ. For a given ℓ, levels are $2(2\ell+1)$ degenerated as a result of Pauli principle and, therefore, correspond to the maximum number of electrons which can occupy given nℓ-shell.

Clusters of size N with a number of electrons sufficient to completely fill the shells are expected to show increased stability, similar to atoms [204]. For clusters with size N+1, the valence electrons of the additional atom will occupy a state with a higher energy, which will be reflected in a lower stability. This will lead to a reduced abundance in the mass spectra. For example, the strongest peak in Fig. 4.1 correspond to Na_{20}. This cluster contains 20 valence electrons, which corresponds to completely filled 1s, 1p, 1d, 2s shells. For Na_{21}, an additional electron will occupy 1f shell, which manifests itself in a significant drop of the yield of Na_{21} when compared to Na_{20}. The energy difference between nℓ-levels depends on details of the potential, see Fig. 4.2, left.

The spherical approximation of the cluster potential is valid for closed shell systems. Open-shell clusters may be distorted [195], which will be reflected in the electronic shells. The electronic structure of non-spherical cluster has been investigated by Clemenger [223], whereas the model has been adapted from nuclear physics (Nilsson
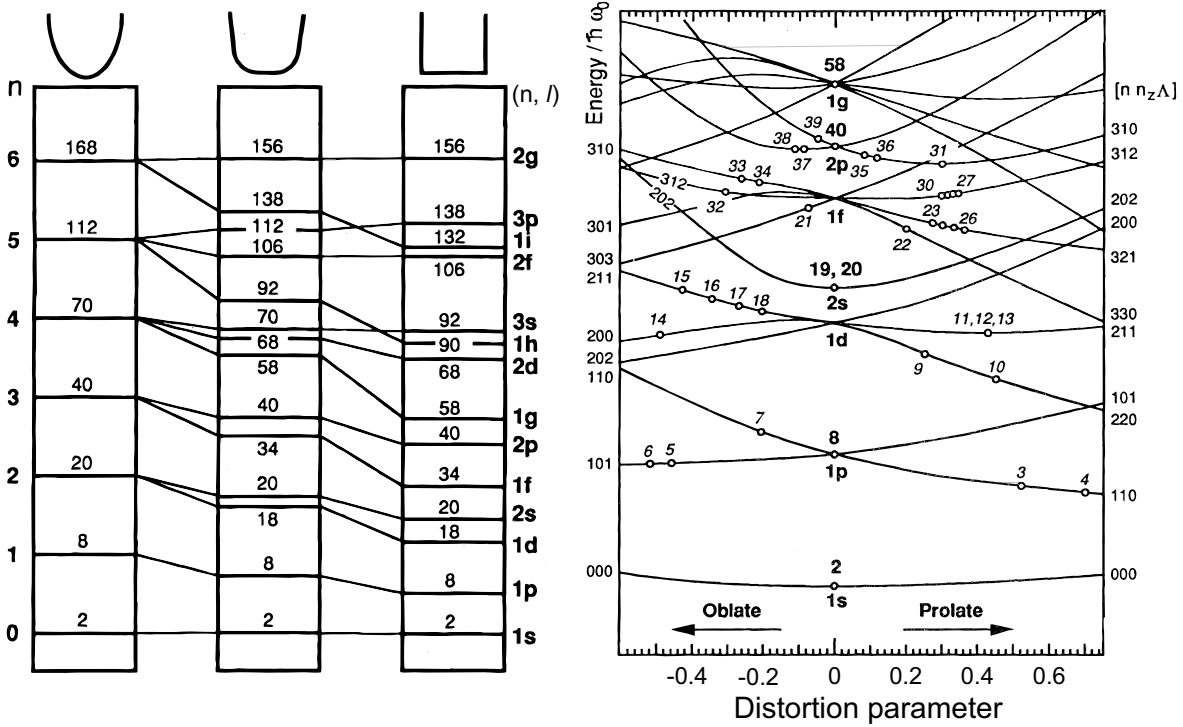
Figure 4.2: (Left) Electron energy level occupation diagram for three spherical potentials. From left to right: harmonic, Woods-Saxon and square well potential. (Right) Clemenger-Nilsson diagram, which shows the positions of electron energy levels in dependence on the distortion parameter. $\xi=0$ corresponds to spherical systems, whereas $\xi<0$ and $\xi>0$ correspond to oblate and prolate shapes, respectively. Adapted from [195].

model) used to determine the shapes of nuclei [224, 225]. In the Clemenger-Nilsson model, the single-particle potential is approximated as a three-dimensional harmonic oscillator, where the deviation from the spherical shape is defined by a distortion parameter ξ. This allows adjusting the shape of the potential, while the volume of the cluster is constant. In the ellipsoidal potential, the degeneracy of the single-electron states removes, leading to a splitting of the electronic levels with different ℓ for given n. The value of the splitting depends on how strong the shape of the cluster deviates from spherical, i.e. ξ (see Fig. 4.2, right). The Clemenger-Nilsson model reproduces the observed peaks of Na clusters with $N \geq 12$ with a good agreement. For clusters with $N \leq 12$ the Clemenger-Nilsson model shows discrepancies, since the ellipsoidal approximation is not applicable to the clusters with only a few atoms.

A more sophisticated way to treat the electronic structure of simple metal clusters is the jellium model. In this model, the ionic core structure is ignored and replaced

by a uniform positive background in a finite volume [226]. For a cluster of size N, the ionic charge is distributed within the sphere[3] with a radius of $R_{cl} = r_{ws}N^{1/3}$, where r_{ws} is Wigner-Seitz radius. Electrons are treated self-consistently in the field induced by the ionic background, within a mean-field approximation. DFT calculations based on jellium model reproduce in general the electronic shell structure of clusters [195, 226, 229, 230]. Semi-empirical and jellium calculation have a good agreement at least for cluster sizes N<500 [231].

Ionization potential

In the frame of the present work, the size dependence of the ionization potential of metal clusters is of particular interest. Starting from the single atom, the IP generally shows a decrease with increasing number of atoms per cluster. With N$\to \infty$, the value of IP is expected to approach the value of bulk work function [232, 233]. The electronic shell structure also plays a role and manifests in the oscillations of IP, e.g. the IP increases for closed electronic shells. The change of the IP has been observed in a variety of studies [202, 234–238]. Examples of the IP of clusters are shown in Fig. 4.3.

A simple way to estimate the size dependence of the IP is based on the assumption, that a cluster can be described as a conducting metal sphere [195]. In this model (CSM[4]), the problem of the determination of the IP comes down to a classical problem to determine the energy which is required to remove an electron from a neutral sphere. This energy consists of two contributions: (i) The work function, that is the energy to remove an electron from the metal; (ii) The electrostatic energy which reflects the interaction energy of an electron remaining charged sphere. The value of the energy can be calculated as [239]:

$$IP = W + \alpha \frac{e^2}{R_{cl}} = W(\text{eV}) + \alpha \frac{14.375}{\text{R}_{cl}(\text{Å})} \tag{4.3}$$

where W is the bulk work function, e is the elementary charge, R_{cl} is the radius of the sphere and α is the slope parameter. Here it is reasonable to also notice the electron affinity (EA), i.e. the energy which is required to remove an electron from the

---

[3]In general, the jellium background is not necessary spherical and can be arbitrarily deformed. The deviations of the jellium potential from spherical is assumed in the spheroidal jellium model [227, 228].

[4]Conducting sphere model
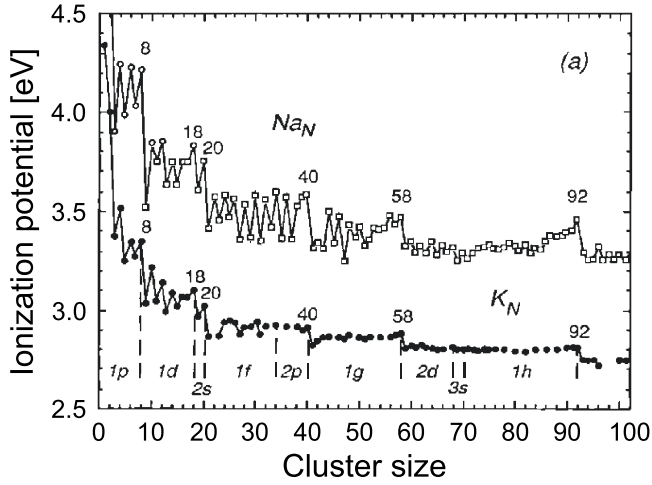
Figure 4.3: (Left) Ionization potential of Na and K clusters. Adapted from [195].

negatively charged cluster. The EA can be calculated as

$$EA = W - \beta \frac{e^2}{R_{cl}} = W(\text{eV}) - \beta \frac{14.375}{\text{R}_{cl}(\text{Å})} \tag{4.4}$$

where β is the slope parameter similar[5] to Eq. 4.3. In the classical model $\alpha = \beta = 0.5$. In general, the value of α and β can vary and depend on the material [240]. Thus, no unique value can be applied to all of the cluster systems. Nevertheles, values of α and β are typically in the ranges $\frac{3}{8} \leq \alpha \leq \frac{1}{2}$ and $\frac{1}{2} \leq \beta \leq \frac{5}{8}$, whereas the difference $\alpha - \beta$ is small for the same element [239]. The deviation of the α and β from the classical values are due to quantum mechanical effects, e.g., correlation and exchange energies [239].

The correction to Eqs. 4.3 and 4.4 can be provided, by adding a factor δ to the cluster radius. The parameter δ determines the electron spill-out effect [240, 241]:

$$IP = W + \alpha \frac{e^2}{R_{cl} + \delta} \tag{4.5}$$

$$EA = W - \beta \frac{e^2}{R_{cl} + \delta} \tag{4.6}$$

In general, the theoretical values reproduce the experimental trends for clusters of simple metals. However, a large deviation has also been reported. For example, for small Ni_N and Co_N, clusters a good agreement is only obtained when lower values of W are assumed [235, 236]. This has been attributed to the difference of packing

---

[5]Note, that here neutral and singly negatively charged spheres are assumed for the calculations of IP and EA, respectively. This model can be extended to multiply charged positive and negative clusters, see for example [240].

or surface structure of clusters with respect to the bulk. A similar situation has been observed for Nb_N clusters [242]. The better agreement with CSM has been obtained by comparison with EA measured in Nb_N^- [203]. By applying a fit of CSM to experimental data of EA(Eq. 4.6)), values of α and δ have been obtained. The dependence of the IP calculated by Eq. 4.5 with extracted α and δ gives a good agreement with experiment. A strong deviation of α from 0.5 observed in these experiments has been assigned as an indication of quantum corrections of the IP. For Hg_N clusters, a strong deviation from the model has been observed for sizes N≤70 [243]. Clusters of these sizes have been found to be non-metal. Between 13≤N≤70 shows evidence for a transition from vdW to covalent bonding. For N>70 the development of the IP merges the results obtained by CSM. Based on these observations, it has been concluded that Hg_N with N ≥70 are metallic[6].

_____

[6]Note, that PES on Hg_N^- anions shows that metal-nonmetal transition takes place at about N=400 [244].

5 Experimental setup

Figure 5.1 shows a schematic view of the experimental setup. The helium droplets source is located in the source chamber (SC). Due to the high gas load during the operation, the SC is equipped with two turbomolecular pumps, with pumping speed[1] of 2650 l/s and 3200 l/s (Leybold MAG W 2800 C and MAG W 3200 CT, respectively). After the formation, droplets pass the skimmer (Beam Dynamics, Inc., 500 μm opening diameter) and enter the differential pumping chamber (ZK1), pumped by a 685 l/s turbomolecular pump (Pfeiffer HiPACE 700). This chamber allows to reduce the vacuum pressure between the SC and the following chamber. After passing ZK1 the helium beam enters the pick-up chamber (PC) in which the vacuum conditions are maintained by the pump of the same type as in ZK1. The pick-up chamber is equipped with a resistively heated oven filled with Mg. In addition, a gas inlet is installed, which allows a doping of droplets by gases, e.g., Xe. A mechanical shutter in PC allows to block the droplet beam in order to acquire signals of bare dopant atoms or background. After the next differential pumping stage (ZK2, 210 l/s, Pfeiffer TMU 261 P), the molecular beam passes the interaction region (pump Pfeiffer Balzers TPU 260, 230 l/s) of home-built magnetic-bottle photoelectron spectrometer (MB-PES) where it intersects with the laser beam. Finally, in the last chamber, the beam enters the ionization region (IC) of a commercial reflectron Time-of-Flight (TOF) mass spectrometer (KAESDORF), where it can interact with the laser radiation as well. The vacuum conditions in the TOF are maintained by two turbomolecular pumps with pumping speeds 520 l/s (Pfeiffer Balzers TPU 520) and 230 l/s (Pfeiffer Balzers TMU260 U) in the ionization region and flight tube, respectively. In addition, the source and pick-up chambers are separated from the spectrometer chambers by a pneumatic valve. The prevacuum is provided by a multi-stage Roots pump (Pfeiffer ACP40, 10 l/s) in SC and turbomolecular pumping stations (Pfeiffer HiCUBE 80, 67 l/s) for the rest of the vacuum machine. Tab. 5.1 summarizes the typical values of vacuum pressure in standby and operation conditions. Note, that when the PC is filled with gas, the pressure in the TOF chamber is reduced, as a result of evaporative cooling of the droplets.

---

[1]Here and in following a values of pumping speed is given for N_2.
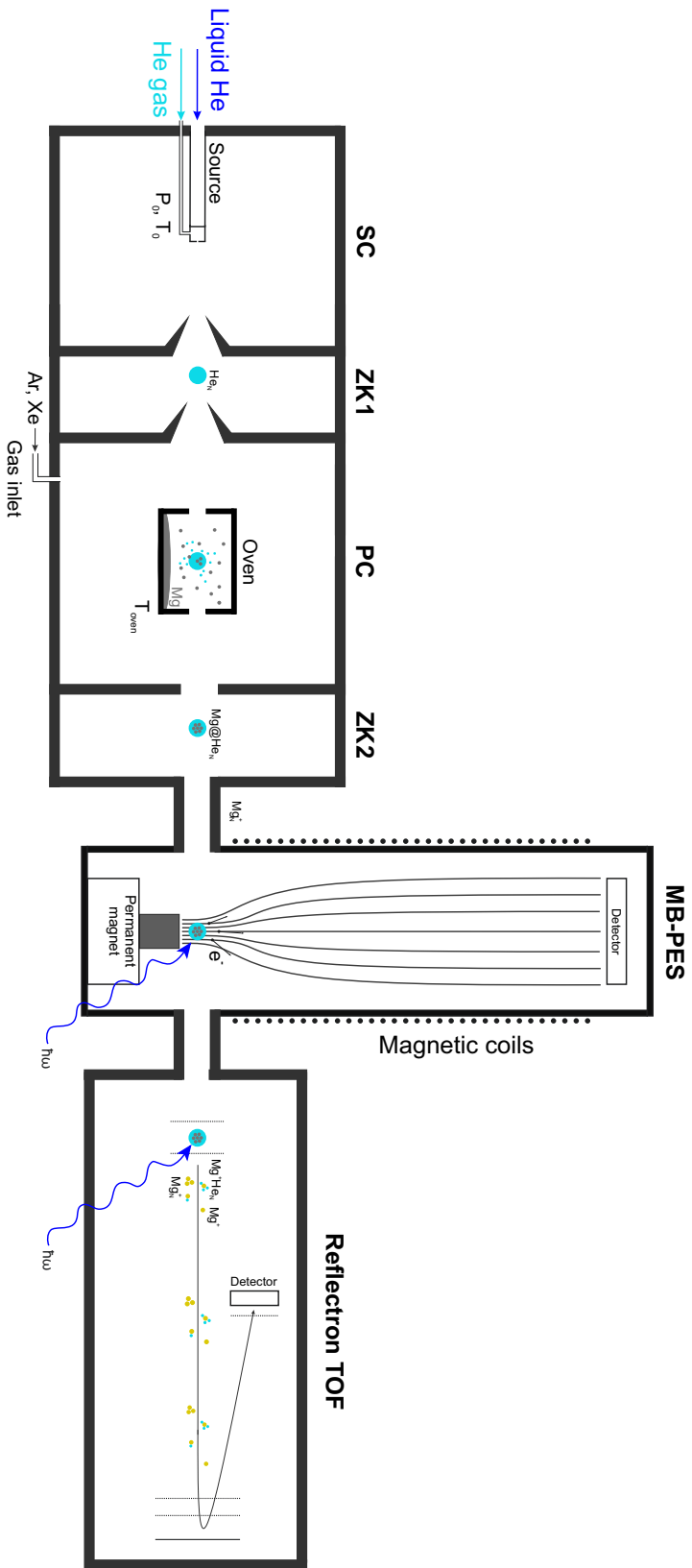
Figure 5.1: Schematic view of the experimental setup, not to scale. SC - source chamber, ZK1 and ZK2 - differential pumping chambers, PC - pick-up chamber, MB-PES - magnetic bottle photoelectron spectrometer, TOF - time-of-flight spectrometer. Parts of the setup and vacuum conditions are described in the text.

Chamber	SC	ZK1	PC	ZK2	IC	ToF
P standby, mbar	$5.4 \cdot 10^{-5}$	$4.7 \cdot 10^{-7}$	$2.3 \cdot 10^{-7}$	$5.4 \cdot 10^{-8}$	$1.7 \cdot 10^{-10}$	$3.4 \cdot 10^{-10}$
P operation, mbar	$3.9 \cdot 10^{-4}$	$8.2 \cdot 10^{-7}$	$2.3 \cdot 10^{-7}$	$5.1 \cdot 10^{-8}$	$2.1 \cdot 10^{-8}$	$4.1 \cdot 10^{-9}$

Table 5.1: Typical values of the pressures in the vacuum chambers in standby and operation. The values of the vacuum pressure in the operation regime are given for T_0=10 K. Note, that pressure change slightly with T_0.

Helium droplet source

The physical principles of the He droplet production are described in Sec.2.1. In the present experiments, helium gas (AirLiquide, Alphagas 2, 99.9999% purity) expands through a flat nozzle with a diameter of 5 μm (electron microscope aperture, Plano GmbH, Mod. A0200P). The stagnation pressure P_0=20 bar is kept constant for all experiments. The droplet sizes are controlled by a temperature T_0. The source is
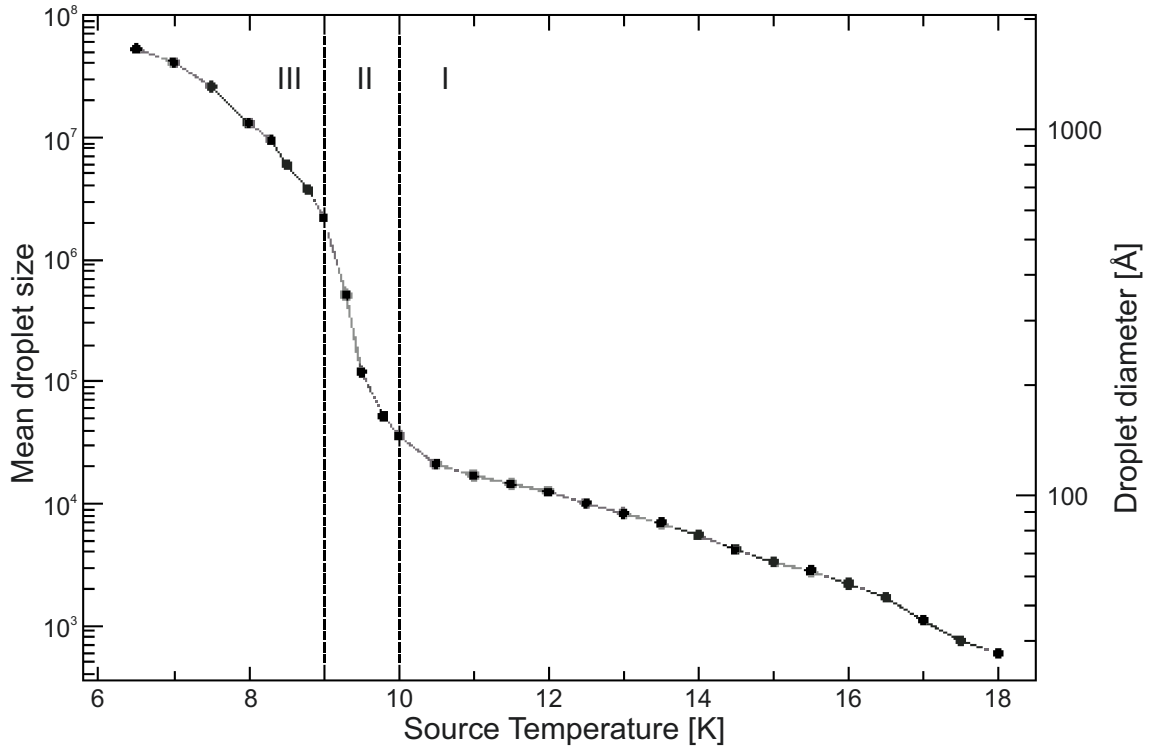
Figure 5.2: Mean droplet size (left y-axis) and diameter (right y-axis) as a function of the source temperature at P_{He}=20 bar. The dashed lines highlight different expansion regimes (see Ch. 2). Adapted from [245].

connected to a flow cryostat (CRYO Industries of America, Inc., Mod., RC 102), cooled down by liquid helium. The temperature T_0 is measured by a Si-diode thermometer (Scientific Instruments, Mod. SI-410). The value of T_0 can be changed through a variation of the liquid helium flow or via heating the source by a resistive heater placed on the coldhead. The heating power is adjusted by PID[2] temperature controller (CryoVac GmbH, Mod. TIC 303M), which allows to maintain the temperature stability in the range of ± 50 mK. A variation of the temperature leads to a change in the average droplet size $\overline{N}_{He}$. Fig. 5.2 shows the dependence of $\overline{N}_{He}$ as a function of T_0 for P_0=20 bar. In the present work temperatures between 9.5 K to 15 K have been used, which corresponds to sizes from $\overline{N}_{He}$=1.2·10^5 to $\overline{N}_{He}$=3·10^3, respectively.

Pick-up region

Doping of the helium droplets takes place in the pick-up region. To achieve this, the droplet beam passes through the resistively heated oven. The construction of the oven is shown in Fig. 5.3, left. Magnesium granules (Alpha Aesar, 99.95% purity) are placed in the stainless steel cartridge (length L=3.5 cm), which is located inside a cylindrical heating element. The construction is surrounded by a protective cooling shield to avoid overheating and helps to reduce temperature fluctuations. The temperature of the oven T_{oven} is measured by a type-K thermocouple.

The pick-up probability depends on the particle density n_{dop} in the pick-up region. The value of n_{dop} can be calculated by Eq. 2.15. The pressure P_{dop} can be obtained from the semi-empirical dependence of pressure on temperature [246]:

$$\lg(P_{dop}) = 5.006 + A + BT_{oven}^{-1} + C\lg(T_{oven}) + DT_{oven}^{-3} \tag{5.1}$$

where A, B, C, D are coefficients specified for given material, P_{dop} in Pa, and T_{oven} in K. For Mg the coefficients are[3] A= 8.489, B= -7813, C= -0.8253 and D =0. The calculations of P_{dop} by Eq. 5.1 have an accuracy of $\pm 5\%$ or better. The pressure-temperature diagram of Mg and corresponding values of $\overline{N}_{Mg}$ (for N_{He}=3.6·10^4) are shown in Fig. 5.3, right. In the present work the temperature of the oven is changed from 231 °C up to 380 °C, giving values of the average doping from $\overline{N}_{Mg}$=0.1 to $\overline{N}_{Mg}$=120, depending on droplet size. Note, that the oven is suitable not only for Mg, but other metals as well, e.g. Ag.

---

[2]Proportional–integral–derivative

[3]The coefficients are defined for the temperatures below the melting point of Mg, that is 650 °C.
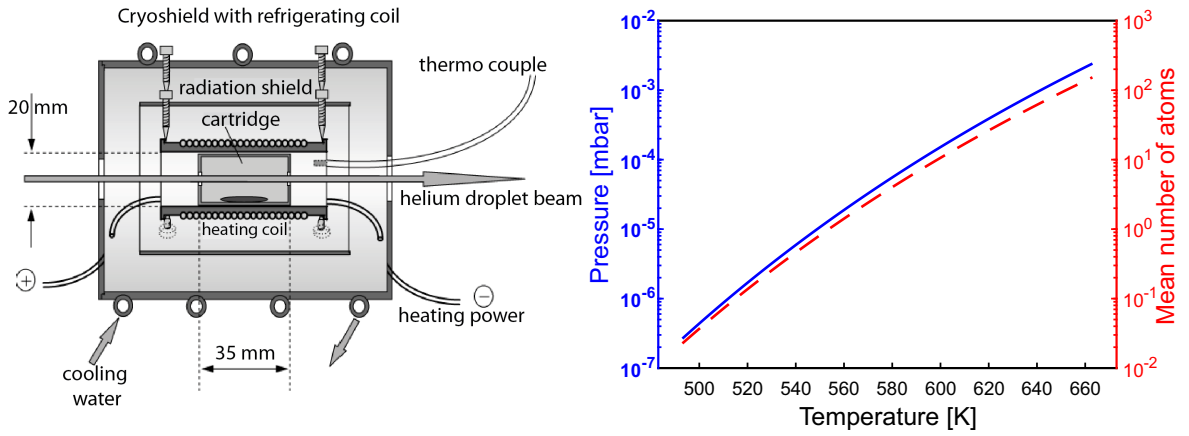
Figure 5.3: (a) Scheme of the oven construction. Adapted from [247,248]. (b) Vapor pressure of Mg (blue, left y-axis) and corresponding values of $\overline{N}_{Mg}$ for droplet size N_{He}=3.6·10⁴ (red, right y-axis)

Besides the oven, the pick-up chamber is equipped with a gas valve, which allows for doping with gas phase particles, e.g. Xe, Ar, etc. In this case, $\overline{N}$ can be obtained by Eqs. 2.13 and 2.15 taking into account L=21 cm and room temperature.

Magnetic-bottle photoelectron spectrometer

The idea and first application of a magnetic-bottle photoelectron spectrometer (MB-PES) have been introduced in the beginning of 1980's by Kruit and Read [249,250]. In the MB-PES, electrons produced upon ionization, start to move in strong inhomogeneous, cylindrically symmetric bottle-shaped magnetic field and later guided by a weak magnetic field to the detector. This leads to a strong increase of electron collection efficiency, giving an opportunity to provide spectroscopy on low density targets.

The construction of the spectrometer used in present the work is schematically shown in Fig. 5.4. The magnetic field is produced by two magnets: a permanent magnet (magnetic flux density $B_p \approx 400$ mT) and a magnetic coils ($B_f \approx 0.6$ mT) wound around the flight tube. The length of the flight tube is 0.95 m. At the end of the flight tube, the electrons are detected by the microchannel plate (MCP). The time-of-flight information is recorded by the multichannel analyzer (FAST ComTec GmbH, mod. 7886) installed in the computer. The electron flight time from the interaction region to the detector is used to determine the kinetic energy of emitted electrons. The magnetic field $\vec{B}_E$ of the earth can affect the electron motions. For compensation, the flight tube is placed between Helmholtz coils, which produce a magnetic field anticollinear to $\vec{B}_E$.
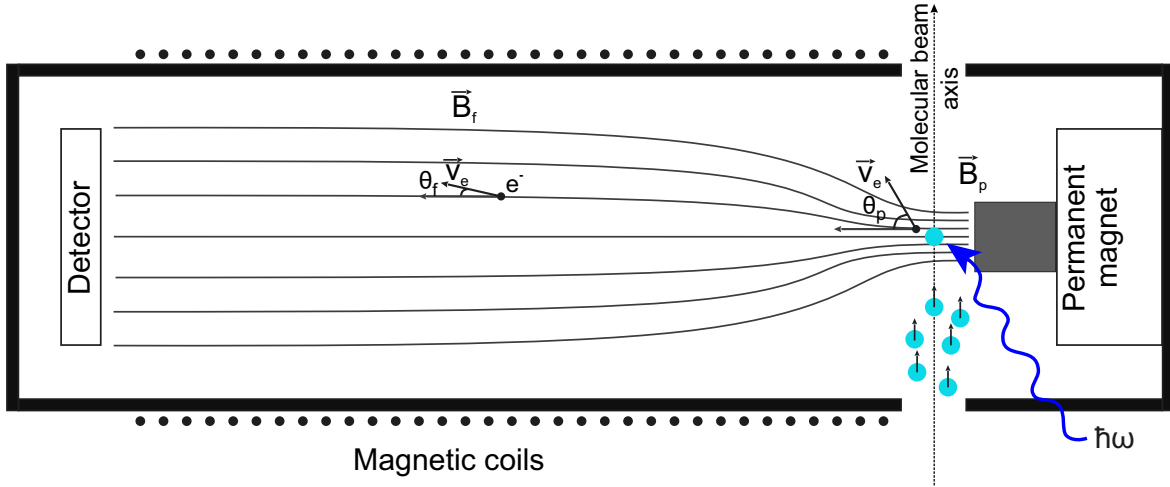
Figure 5.4: Schematics of the magnetic-bottle photoelectron spectrometer used in the experiment.

Electrons moving in a magnetic field undergo a spiral motion, caused by the Lorentz force. For an electron initially located in the strong inhomogeneous magnetic field region, with velocity $\vec{v}_e$ at the angle θ to the spectrometer axis (Fig. 5.4), the angular frequency ω and radius of the orbit r are:

$$\omega = \frac{e|\vec{B}|}{m_e} \tag{5.2}$$

$$r = \frac{|\vec{v}_e| \sin\theta}{\omega} \tag{5.3}$$

where e is the elementary charge and m_e is the electron mass. The corresponding angular momentum $\mathcal{L}$ of the electron is:

$$\mathcal{L} = I \cdot \omega = mr^2\omega = \frac{m^2 |\vec{v}_e|^2 \sin^2\theta}{eB} \tag{5.4}$$

The value of $\mathcal{L}_p$ in the inhomogeneous field is conserved [250] and, therefore, equal to the angular momentum in the flight tube $\mathcal{L}_f$. Hence:

$$\frac{m^2 |\vec{v}_e|^2 \sin^2\theta_p}{eB_p} = \frac{m^2 |\vec{v}_e|^2 \sin^2\theta_f}{eB_f} \tag{5.5}$$

which leads to

$$\sin\theta_f = \sin\theta_p \cdot \left(\frac{B_f}{B_p}\right)^{\frac{1}{2}} \tag{5.6}$$

The magnetic field B_p produced by the permanent magnet is significantly stronger than B_f. Therefore, the angle θ_f in the flight tube is smaller than θ_p. For the spectrometer used in the present work, the electrons emitted perpendicular to field $\vec{B}_p$ nearly parallelize in the flight tube, and

$$\theta_f = \arcsin\left(\sqrt{\frac{0.6\,\mathrm{mT}}{400\,\mathrm{mT}}}\right) = 2.2° \tag{5.7}$$

The best theoretical resolution of MB-PES can be calculated as [251]:

$$R = \frac{B_p}{B_f} \tag{5.8}$$

and for B_f and B_p is $R \approx 670$. Nevertheless, the resolution is lower, due to the several factors: (i) The electrons are collected from 4π solid angle of emission. That implies, that the electrons emitted towards the magnet require an additional time to turn towards the detector, which will affect the observed flight times. (ii) Not complete screening of the magnetic field of Earth. (iii) The limiting time resolution of the acquisition device.

Reflectron Time-of-Flight mass spectrometer

The operation principle is based on the acceleration of charged particles in an electric field and measurements of their flight times τ_{ion} after passing a known distance. For a fixed acceleration voltage, the flight time of the particle is determined by the mass m_{ion} and charge q_{ion}, or more precisely by it mass-to-charge ration m_{ion}/q_{ion}. In particular, when the particle is singly ionized, the value of τ_{ion} allows to determine the mass.

The resolution of the TOF spectrometer can be affected by several factors [252], e.g. (i) Ion energy spread, due to finite ionization volume. (ii) 'Turn-around' effect due to the initial velocity distribution of ions. The ions which move in the direction opposite to the acceleration field require additional time for deceleration and turning towards the detector. (iii) Length of the ionizing pulse and rise time of the acceleration pulse. (iv) The time response of the detector. A compensation of most effects can be obtained by a combination of the Wiley-McLaren acceleration scheme with a reflectron.

In the extraction region, the ions which pass the higher potential will have higher velocities, but they need a certain time to leave the acceleration unit. In contrast, the ions which start their movement closer to the end of the extraction region, escape at earlier times, but with lower velocities. This leads to compensation of (i) at a certain

distance of L_f which is equal to the length of the acceleration region. The distance L_f can be largely increased by application of the two-stage acceleration, proposed by Wiley and McLaren [253]. In this scheme, the focus point L_f is determined by the ratio of the fields strengths of both stages. The 'turn-around' effect can also be compensated by application of delayed extraction, i.e. introduction of a time delay between ionizing and extraction pulses. It allows ions to reach a new position, at which the acceleration provided by the extraction field allows to reach a detector position with the same flight times. The resolutions $R = m_{ion}/\Delta m_{ion}$ of several thousand have been reported [254, 255].

The reflecton type TOF spectrometer, has been proposed by Mamyrin *et al.* [256]. The compensation of the energy spreading of the ions is realized by introducing an electrostatic reflecting system in the flight tube. The ions with higher velocities move deeper in the reflecting field than the slower ones. Hence, it requires more time for fast ions to leave the reflector. By an appropriate choice of the reflector voltages, it is possible to achieve a condition when all the ions reach the detector simultaneously. Values of R$\geq$10^4 can be achieved for such spectrometers [252].

Laser systems

The main light source for the photoelectron spectroscopy studies is a dye laser. The concept of such laser is based on using a solution of an optical dye as the active medium for laser light generation. Optical dyes have wide absorption and fluorescence spectra, which allow to achieve tunable radiation. Fig. 5.5 shows a typical electronical level scheme of dye molecules. For the molecule in the singlet ground state S_0, the absorption of photons may lead electronical excitation. Since singlet-triplet transitions are forbidden, the excitation is allowed only within the singlet system. Due to the Franck-Condon principle, a limited number of the vibrational states in S_1 will be occupied. After a short time ($\tau_{relaxation} \approx 100\,\text{fs}$), the molecule is relaxes radiationless to the lowest vibrational state of S_1, from which the radiative transition to S_0 occurs [257]. The possible transitions to different vibrational states of S_0 lead to the wide emission spectrum. The high density of rovibrational states is the reason of wide and unstructured absorption and emission spectra[4] [257]. As an example, Fig. 5.5 shows absorption and

---

[4]Note, that radiationless transition between singlet and triplet states can also take place, e.g. $S_1 \rightarrow T_1$. This process is called intersystem crossing and caused by the collisions between molecules in the solution. A molecule in T_1 state may also absorb photon, i.e. a $T_1 \rightarrow T_2$ excitation. When the absorption $T_1 \rightarrow T_2$ lying in the same spectral region as $S_1 \rightarrow S_0$, it can absorb a fluorescent
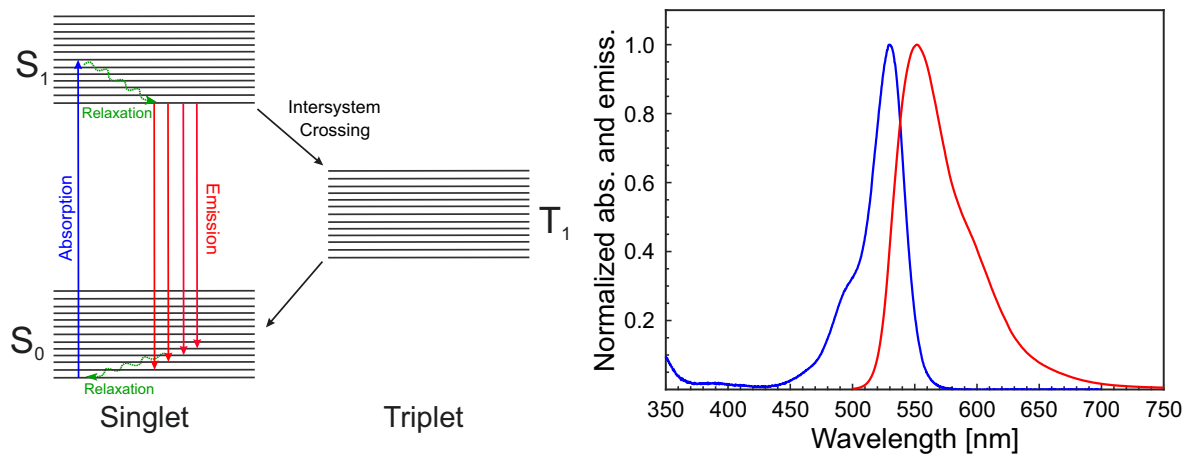
Figure 5.5: (Left) Electonical level scheme of optical dyes. Arrows indicate different processes: absorption (blue), emission (red), relaxation (green) and intersystem crossing (black). (Right) Absorption (blue) and emission (red) spectra of Rhodamine 6G in methanol. Spectra are taken from PhotochemCAD 3 database [258].

fluorescence spectra of Rhodamin 6G dye.

As an active medium, optical dyes allow to realize laser light generation within the wavelength region of the fluorescence, due to fast vibrational relaxation time [257]. It leads to an effective population of excited state S_1 and meanwhile fast depletion of rovibrational states of S_0. Hence, a population inversion can be achieved. The tuning of the laser wavelength is realized by introducing a dispersive element in the resonator, which selects photons with the chosen wavelength for amplification. The possibility to tune a laser wavelength opens great opportunities to use dye lasers for spectroscopy. The main disadvantage is a relatively short wavelength region which is covered by a single dye. Covering a broad spectral region requires a change of dyes, which makes such experiments challenging.

In present experiments, a dye laser (LAS GmbH, mod. LDL-20505) is operated with Rhodamine 6G in methanol. The emission is tunable in the range 558-575 nm. The UV-light is produced by second harmonic generation in a BBO[5] crystal installed at the laser output. It allows to create radiation between[6] 280 nm and 287 nm. As a pump source, the second harmonic (532 nm) of Nd:YAG laser (Spectra-Physics, mod.

---

light. This process decreases the efficiency of the laser light generation in dye lasers.

[5]Beta-Barium Borate

[6]The wavelength range in the UV-region is shorter than allowed by fundamental wavelengths due to inefficient SHG near the edges of fluorescence spectrum.

Quanta-Ray Pro-290) is used. The repetition rate is defined by the pump laser (20 Hz). Pulses with a length of τ_{las}=10 ns and energies up to 50 μJ can be produced.

In the second laser system, an optical parametrical oscillator (OPO) is used to produce tunable radiation. The operation principle is based on the non-linear optical process called parametric light generation [257]. When a strong laser wave (pump) with frequency ω_p propagates in the nonlinear medium the energy may be transferred to two light waves with frequencies ω_s (signal) and ω_i (idler) red-shifted relative to ω_p. That can be represented as a conversion of the photon with energy $\hbar\omega_p$ into two photons with energies $\hbar\omega_s$ and $\hbar\omega_i$. The energy conservation requires that

$$\hbar\omega_p = \hbar\omega_s + \hbar\omega_i \tag{5.9}$$

whereas the momentum conservation requires

$$\vec{k_p} = \vec{k_s} + \vec{k_i} \tag{5.10}$$

where $\vec{k_p}$, $\vec{k_p}$ and $\vec{k_p}$ are the wave vectors of pump, signal and idler, respectively. The relation Eq. 5.10 is called phase matching condition. These conditions can be realized in anisotropic crystals, e.g. BBO. Depending on the propagation directions of the participating waves, two schemes can be realized: (i) Collinear, when pump, signal and idler waves propagate in the same direction. (ii) Non-collinear, when the directions are different. Tuning of the wavelength is achieved by changing the phase matching conditions, e.g. by rotating the crystal.

In OPO laser system used in this work (EKSPLA NT242-SH/SFG) the OPO cavity is pumped by a 3rd harmonic of Nd:YAG laser. For parametric generation, a type II BBO crystal is used. The light produced by parametric generation can be tuned in the range 400-2600 nm by rotating the OPO crystals. The signal and idler beams are separated by a Rochon prism installed at the output of the OPO cavity. The radiation in the UV-wavelength region is produced by SHG in type I BBO crystal from the OPO signal beam. The separation of fundamental and second harmonics is realized by a second Rochon prism. The system operates at a repetition rate of 1 kHz, a pulse length of τ_{las}=10 ns and pulse energies up to 5 μJ, depending on the wavelength. The spectral linewidth $\Delta\lambda \approx$0.2 nm at $\lambda_{las} \leq$286 nm.

6 Results

In the present chapter experimental results on the spectroscopy on Mg doped helium droplet are presented. R2PI-photoelectron spectra at the foam resonance are shown in dependence on droplet size, average doping and laser pulse energy. In addition, electron spectra recorded as a function of laser wavelength are presented. At the end of the chapter, ToF mass spectra are shown for wavelengths down to 215 nm. The dependencies of the cluster signals on the photon energy are used to determine the vertical IP of Mg clusters.

6.1 Photoelectron spectroscopy on Mg ensembles

The R2PI scheme of the present experiment represents a 'virtual pump-probe experiment', where absorption of the first photon leads to the excitation of a single foam atom, whereas the second photon of the same laser pulse probes the product of the triggered dynamics. It is obvious, that a full time resolution cannot be achieved. Thus, the signal will contain contributions from all processes taking place on the time scale of the laser pulse, that is 10 ns.

In the first set of experiments, the foam was probed under different initial conditions. The laser wavelength was keep constant at λ_{foam}= 282.5 nm (photon energy E_{ph}= 4.39 eV), corresponding to the maximum of the absorption. By changing the doping conditions from single to tens of atoms, possible size effects are probed, whereas the impact of the helium matrix is studied by varying the average droplet size from $\overline{N}_{He}$= 3.3·10^3 to $\overline{N}_{He}$= 1.2·10^5. As a next step, photoelectron emission has been recorded as a function of laser wavelength λ_{laser} within the foam absorption line, i.e., between 275 and 285 nm. The obtained information can uncover possible contributions of different excitation pathways, which has not been revealed by ion mass spectroscopy.

Dependence on doping conditions and droplet size.

Examples of photoelectron spectra are shown in Fig. 6.1 for different average doping and a droplet size of $\overline{N}_{He}$= 5.2·10^4. The laser pulse energy was fixed at E_{las}=7 μJ. At
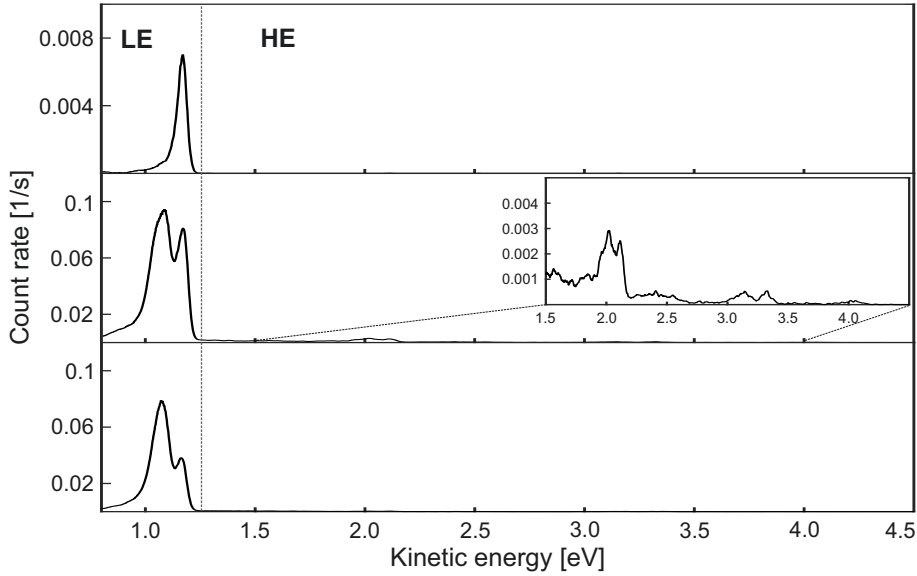
Figure 6.1: Photoelectron spectra of Mg doped droplets at λ_{foam}, for $\overline{N}_{He}$=5.2·10^4 and pulse energy E_{las}=7 μJ. (Top) Low doping $\overline{N}_{Mg}$=0.1. (Middle) Intermediate doping $\overline{N}_{Mg}$=17. (Bottom) High doping $\overline{N}_{Mg}$=80. Dashed line drawn to separate LE and HE regions (see text).

low doping conditions $\overline{N}_{Mg}$=0.1 (Fig. 6.1,top), a single peak at E_{kin}=1.17 eV can be identified. The doping conditions correspond to the pick-up of single atom. Therefore, the peak represent ionization of a single embedded Mg atom. With increasing number of atoms, a second broad feature (LE) shows up close to the single atom peak at E_{kin}=1.09 eV (Fig. 6.1, middle). In addition, a weak structured signal (HE) has been observed at E_{kin} ≥1.2 eV. The peaks center at 2 eV, 2.12 eV, 3.14 eV, 3.3 eV, 4.05 eV (Fig. 6.1, inset). This features appears only under conditions, when multiple atoms are present in the droplets. At high Mg load (Fig. 6.1, bottom), peaks close to 1 eV can be observed, but no evidence for electrons with high kinetic energy is found.

To obtain the information about the dependence of the electron signal on the doping conditions, spectra have been recorded at different $\overline{N}_{Mg}$. As an example, the results for $\overline{N}_{He}$=5.2·10^4 are shown in Fig. 6.2 (left), where twenty-four spectra are combined. The x-axis corresponds to the average number of Mg atoms per droplet, calculated according to the pick-up statistics for given droplet size and oven temperature. The y-axis corresponds to the kinetic energy of the emitted electrons. The electron yield is shown by color in a logarithmic scale. In the LE-part of the spectra, the peak with kinetic energy E_{kin}=1.17 eV appears at the lowest doping conditions ($\overline{N}_{Mg}$=0.1). With

Figure 6.2: (Left) Photoelectron spectra, presented as a two dimensional intensity plot for different average doping and droplet size $\overline{N}_{He}$=5.2·10^4. For the presentation, twenty four spectra are combined and smoothed. Yields are presented using a color log scale. All spectra are integrated over 8000 laser pulses, with E_{las}=7 µJ. (Right) Electron yields (linear scale) at selected kinetic energies E_{kin}=2.12 eV (blue circles), 3.14 eV (red squares), 4.05 eV (green diamonds) as function of average doping for droplet size $\overline{N}_{He}$=5.2·10^4.

increasing $\overline{N}_{Mg}$ the yield $Y(1.17\,\text{eV})$ increases and broadens. The broadening can be attributed to the appearance of the second peak with E_{kin}=1.09 eV, which became clearly resolved at $\overline{N}_{Mg}$=12. At the same value of $\overline{N}_{Mg}$ the yield $Y(1.17\,\text{eV})$ is highest and decreases with the further increase of $\overline{N}_{Mg}$, peak with E_{kin}=1.17 eV dominates in the spectra. After $\overline{N}_{Mg}\approx$80 the yield of both peaks significantly drops down.

The emission of HE-electrons ($E_{kin} \geq$1.2 eV) becomes visible when the average number $\overline{N}_{Mg}$ exceeds a value of one. The total signal increases with $\overline{N}_{Mg}$ up to a maximum value at $\overline{N}_{Mg}$=25. For high doping the HE signal vanishes and only the low energy peaks remain. In the range 1.2 eV$\leq E_{kin} \leq$1.9 eV, the signal is broad and not structured. For E_{kin}>1.9 eV, clearly resolved peaks are observed. Note, that after the appearance of all photoelectron peaks, no additional features or shifts are observed with the change of $\overline{N}_{Mg}$. To demonstrate the dependence of the emission of electrons certain E_{kin}, the photoelectron yields have been integrated for the corresponding peaks. Selected results are shown in (Fig. 6.2 right). The yields differ for each peak and decrease with increasing E_{kin}, but have a maximum at the same value of $\overline{N}_{Mg}$. Additionally, peaks centered at higher kinetic energies appear at slightly higher values of $\overline{N}_{Mg}$, but reach their maximum values at the same $\overline{N}_{Mg}$, after which the signals decrease.
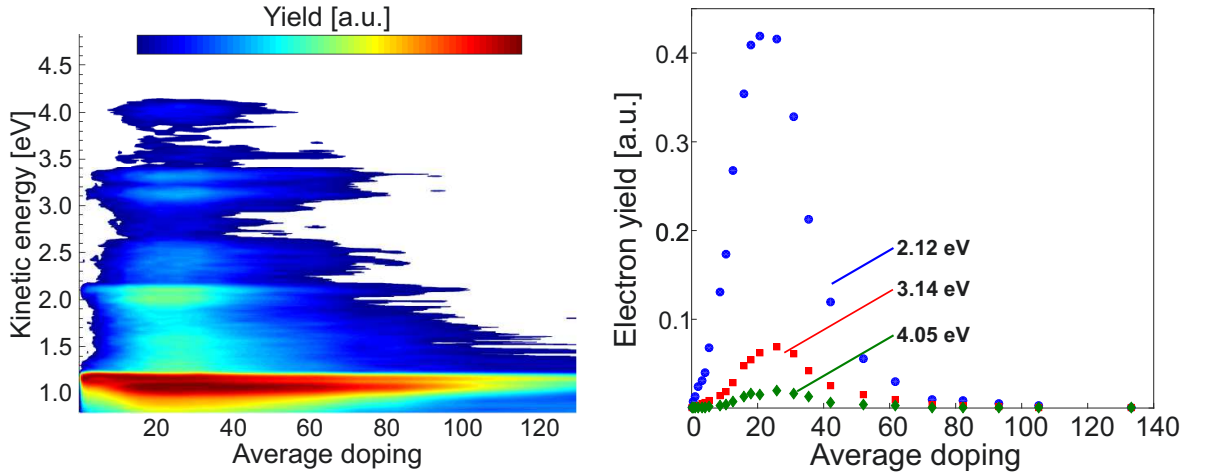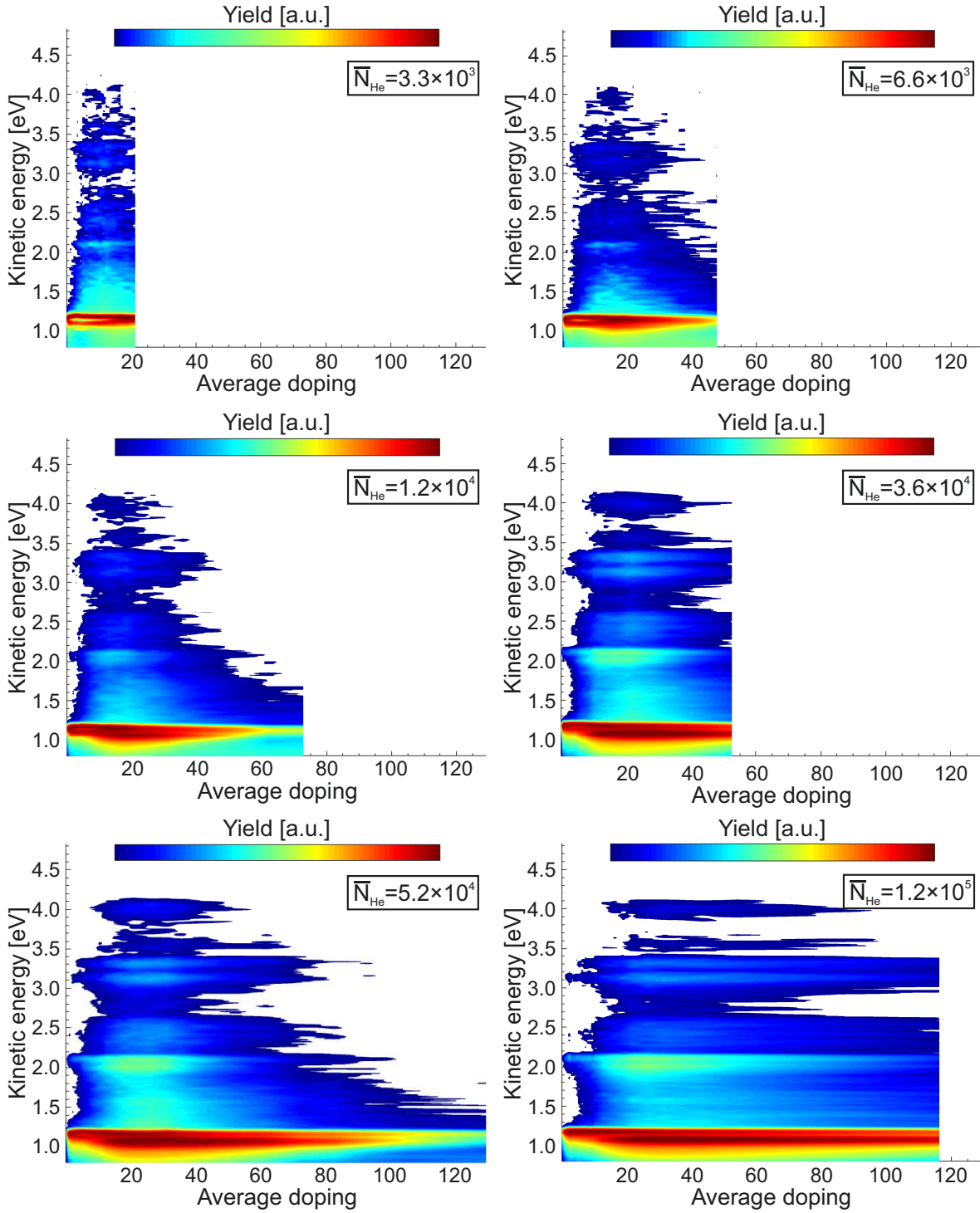
Figure 6.3: (Left) Series of photoelectron spectra, presented as a two-dimensional intensity plot for different average doping and selected droplet sizes. For the presentation, 17 to 24 spectra are combined and smoothed. Yields are presented using a color log scale. All spectra are integrated over 8000 laser pulses, with $E_{las}=7\,\mu$J. The splitting of the lines for small droplets is due to detector saturation.

Figure 6.4: Total photoelectron yield ($E_{kin} \geq 1.2$ eV) for droplet sizes $\overline{N}_{He}$=5.2·10^4 (blue circles), 1.2·10^4 (red squares), 5.7·10^3 (green diamonds).
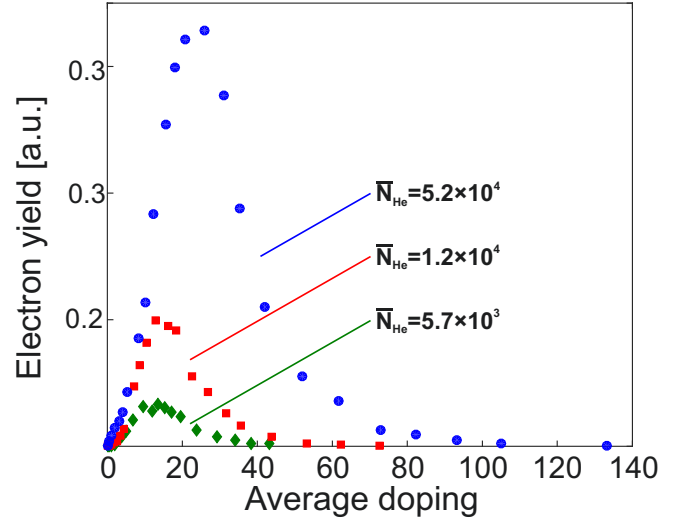
To reveal the impact of droplet size, similar measurements have been conducted for droplets with $\overline{N}_{He}$=3.3·10^3-1.2·10^5 (Fig. 6.3). Generally, the shape of the spectra is similar and independent on the droplet size. No additional features or shifts of the photoelectron peaks are observed. The doping range where the HE electrons are detected, as well as the lowest doping level at which the HE emission can be observed, depend on $\overline{N}_{He}$ and increases with droplet size. In order to determine the dependence of the lowest doping level and effective doping range, within which the HE emission is observed, the total photoelectron yields of HE electrons ($E_{kin} \geq 1.2$ eV) as a function of $\overline{N}_{Mg}$ have been extracted. The results for chosen $\overline{N}_{He}$ are shown in Fig. 6.4. Clearly, the doping ranges strongly depend on $\overline{N}_{He}$. In addition, the yield is higher for larger droplets.

Dependence on laser pulse energy

To investigate the impact of the laser pulse energy on the emission of HE-electrons as well as the contribution of multiphoton processes beyond the R2PI scheme, spectra have been recorded at different laser pulse energy E_{las}. Examples are shown in Fig. 6.5, left. The increase of E_{las} leads to an increase of the total photoelectron signal, whereas no additional features can be observed. For low pulse energies, the HE features are weak, but the double peak near 1 eV is pronounced. With increasing E_{las}, the signals in both LE and HE regions rise. Moreover, at high pulse energies, the LE peak structure became more complex and intensities became comparable to the high energy region. This effect is caused by the saturation of the detector and has been cross-checked on
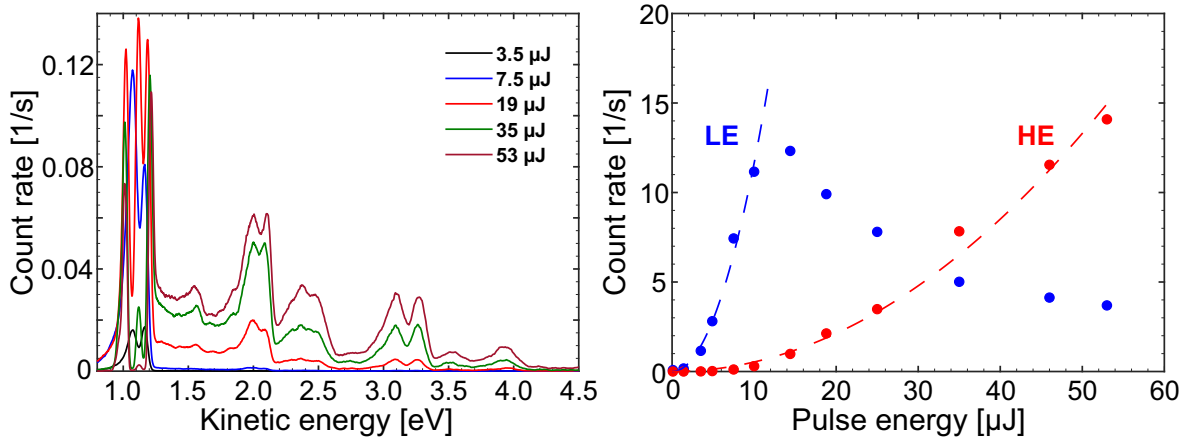
Figure 6.5: (Left) Photoelectron spectra at different laser pulse energies recorded for droplets size $\overline{N}_{He}$=5.2·10^4 and an average doping $\overline{N}_{Mg}$=12. Spectra are integrated for 20000 shots for E_{las}=3.5-7.5 μJ, 10000 shots for E_{las}=19 μJ and 5000 shot for 35-53μJ. (Right) Total photoelectron yields at $1\,\mathrm{eV} < E_{kin} < 1.2\,\mathrm{eV}$ (LE, blue) and $E_{kin} \geq 1.2\,\mathrm{eV}$ (HE, red). The dashed lines correspond to fits with a square function. Both, the multiple peaks in the LE region and the decrease of photoelectron LE signal are due to a saturation of the detector.

bare Mg atoms. At the atomic resonance, the LE photoelectron structure becomes similar when the laser power or the Mg vapor pressure is too high. The integrated yields of both LE and HE electrons are shown in Fig. 6.5, right. For HE electrons, the yield scales with laser power as E_{las}^2. For the LE features, a similar dependence can only be observed below E_{las}= 10 μJ, beyond which the detector is saturated. Such dependence of photoelectron signal is anticipated for R2PI.

Wavelength dependence

The results of photoelectron spectroscopy presented above have been achieved at a wavelength λ_{foam}=282.5 nm, whereas the absorption of the Mg foam is broad and takes place in a wavelength range between 275 nm to 284 nm (photon energies E_{ph}=4.49-4.34 eV, respectively). As it has been shown in Ch. 3, the mass spectrometry shows no specific features for different wavelengths [51] within the absorption. PES, however, can provide additional information or possibly reveal specific ionization pathways. Thus, total electron yields for both LE and HE regions have been recorded as a function of λ_{las}, see Fig. 6.6. Photoelectron emission takes place within a wavelength range of 275-285 nm. Similar dependencies on λ_{las} are found for HE and LE electrons, reflecting the fact that the photoemission process of LE and HE electrons has a similar intermediate

Figure 6.6: Total yields of LE (blue) and HE (red) electrons as a function of laser wavelength λ_{las} normalized on the laser pulse energy. The peak at λ_{atom}=285.25 nm corresponds to the free atom resonance (see right arrow) and can only be observed in the LE range. The foam transition at λ_{foam}=282.5 nm is depicted by the arrow. Droplet size $\overline{N}_{He}$=5.2·10^4, average doping $\overline{N}_{Mg}$=10.
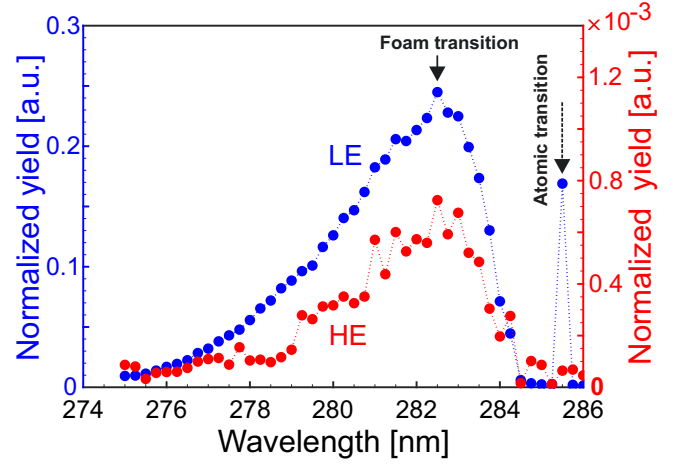
step. The achieved results are in perfect agreement with the absorption profile observed by ion TOF spectroscopy [51], see Fig. 3.7.

In general, with the change of the wavelength, the photoelectron spectra show similar structure as observed at λ_{foam}. However, new peaks show up at λ_{laser}=281 nm (F_{281}), 279 nm (F_{279}), 278 nm (F_{278}) at kinetic energies of E_{kin}^{281}= 2.61 eV, E_{kin}^{279}= 1.86 eV and E_{kin}^{278}= 3.60 eV, respectively. The corresponding spectra are shown in Fig. 6.7. The peaks F_{278} and F_{281} possibly overlap with the signal of other features, which are also visible at the foam resonance. The feature F_{279} remains in the spectra within the wavelength region 278-281 nm, whereas all the other features appears only a specific λ_{laser}. Similar spectral features have also been observed at different doping conditions.

Monitoring the electron yields corresponding to the features F_{281}, F_{279} and F_{278} with respect to the wavelength, provide additional information about the response on the laser wavelength. For F_{281}, a wavelength scan has been conducted with a step size of $\Delta\lambda$=1·10^{-3} nm (dye laser). The result is shown in Fig. 6.8, left, where three peaks can be resolved. According to the fit based on Gaussian functions, three transitions are revealed which center at 281.20 nm, 281.12 nm, and 280.99 nm, with corresponding FWHM $\Delta\lambda_{281.2}$=0.043 nm, $\Delta\lambda_{281.12}$=0.082 nm and $\Delta\lambda_{280.99}$=0.055 nm, respectively. A scan in the vicinity of 279 nm reveals, that F_{279} centers at 279.5 nm (Fig. 6.8,b) and has a width of $\Delta\lambda$=1.5 nm (ΔE_{ph}=24 meV). The feature F_{278} only appears at λ_{las}=278 nm. Note that the dye laser does not provide an efficient emission in this wavelength region λ_{las}<280 nm. Therefore the scans have been conducted with the OPO laser using a wavelength step size of $\Delta\lambda$=0.2 nm.
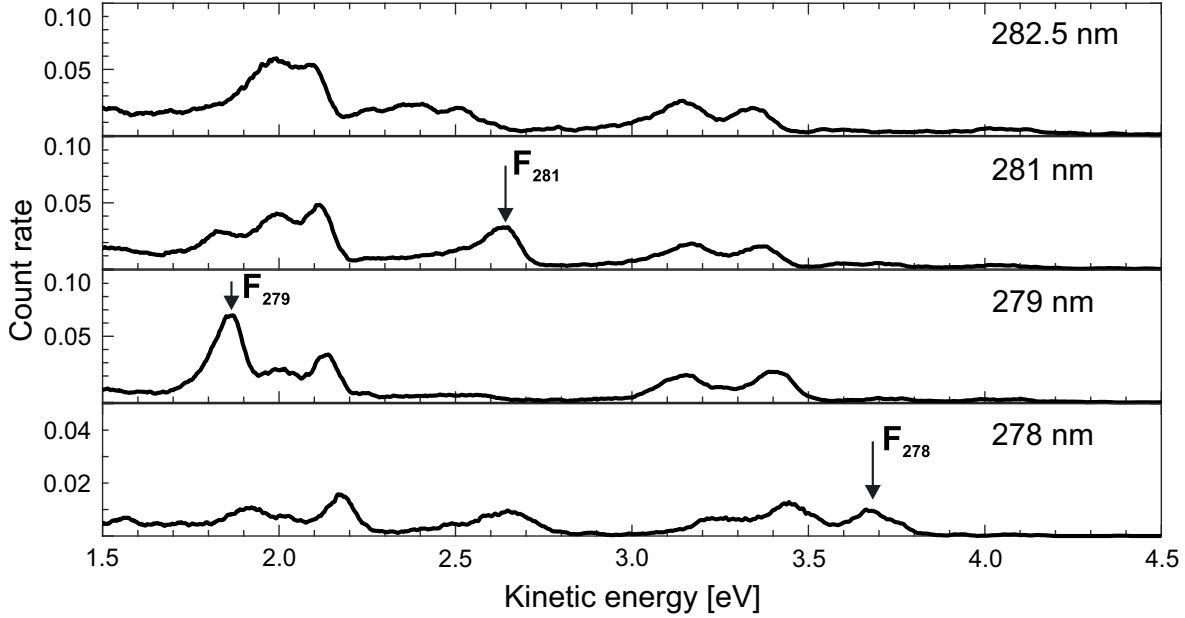
Figure 6.7: HE-part of the photoelectron spectra recorded at selected wavelengths. The spectrum taken at 282.5 nm is shown as a reference. Photoexcitation at wavelengths of 281 nm, 279 nm, 278 nm leads to new features at $E_{kin}(F_{281})$=2.61 eV, $E_{kin}(F_{279})$=1.86 eV, $E_{kin}(F_{278})$=3.60 eV, respectively. Droplet size $\overline{N}_{He}$=1.2·10^5, average doping $\overline{N}_{Mg}$=20.
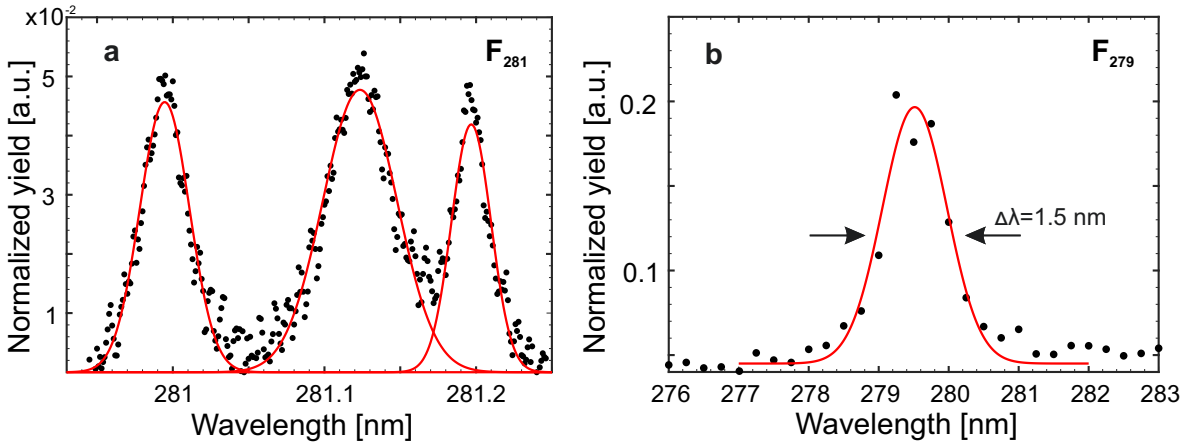
Figure 6.8: (a) Yield of peak F_{281} as a function of laser wavelength near λ_{laser}=281 nm. Black circles correspond to experimental data. (b) Yield of the feature F_{279} as a function of λ_{laser} (black) with $\Delta\lambda$=0,2 nm. The red solid lines correspond to fits with Gaussian functions.

6.2 Direct ionization of Mg cluster at high doping conditions

The optical response of the foam has been observed to depend on the laser wavelength [51]. According Fig. 6.6, the emission shows a similar dependence on the laser wavelength for LE and HE electrons. All of the characteristical signatures can be attributed to a foam inside He droplets. On the other hand, the HE features depend on $\overline{N}_{Mg}$ and disappear at high doping condition (Fig. 6.3). To a reveal the possible formation of compact Mg_N clusters at high droplet load, the optical response has been probed at shorter wavelengths, $\lambda_{las} < 272$ nm, i.e., far from the foam resonance. If clusters are formed, an enhanced ion yield is anticipated.

In the present experimental setup, photoelectron spectroscopy cannot be used for two reasons. (i) Clusters are not mass selected. Thus, photoelectron spectra will contain contributions of different Mg_N, making an assignment to specific sizes impossible. (ii) One can expect, that clusters can be ionized by single photon absorption at photon energies of about 5 eV. Hence, the electron kinetic energy will have energies in the meV range. Unfortunately, the photoelectron spectrometer used in the experiment has a low detection efficiency for low energy electrons. These problems can be overcome by mass spectrometry, since it can simultaneously detect all Mg_N^+ ions.

Examples of mass spectra recorded at the foam resonance and at $\lambda_{las} = 254$ nm (4.88 eV) are shown in Fig. 6.9 for $\overline{N}_{He} = 5.2 \cdot 10^4$. At $\overline{N}_{Mg} = 26$, corresponding to the maximum of the HE electron emission (see Fig. 6.4, top left), the spectrum recorded at λ_{foam} shows a pattern which includes a Mg_N^+ clusters with N≤12, as well as a Mg^+He_N progression. This spectrum is similar to the one shown in Fig. 3.6 and typical for mass spectroscopy experiments on Mg foam. With further increase of $\overline{N}_{Mg}$ the total ion yield and cluster sizes decreases. At high doping level, e.g., $\overline{N}_{Mg} = 67$ (Fig. 6.9, bottom left), practically no signal from clusters can be observed. Only a weak monomer signal is present. The decrease of the ion signals correlates with the absence of HE electron emission.

In contrast to the λ_{foam}, spectra recorded at shorter wavelength show different behavior. For $\overline{N}_{Mg} = 26$, larger clusters with N up to 30 are observed (Fig. 6.9, right top) . In addition, no evidence for snowballs is obtained. With increasing of Mg load, the cluster progression extends to larger sizes. For example, $\overline{N}_{Mg} = 67$, signals of Mg_N with N as large as 56 are observed (see Fig. Fig. 6.9, right bottom).

To reveal the doping dependence of Mg cluster formation, the total yields of Mg_N^+ has been extracted for both wavelength as a function of average doping see Fig. 6.10. The
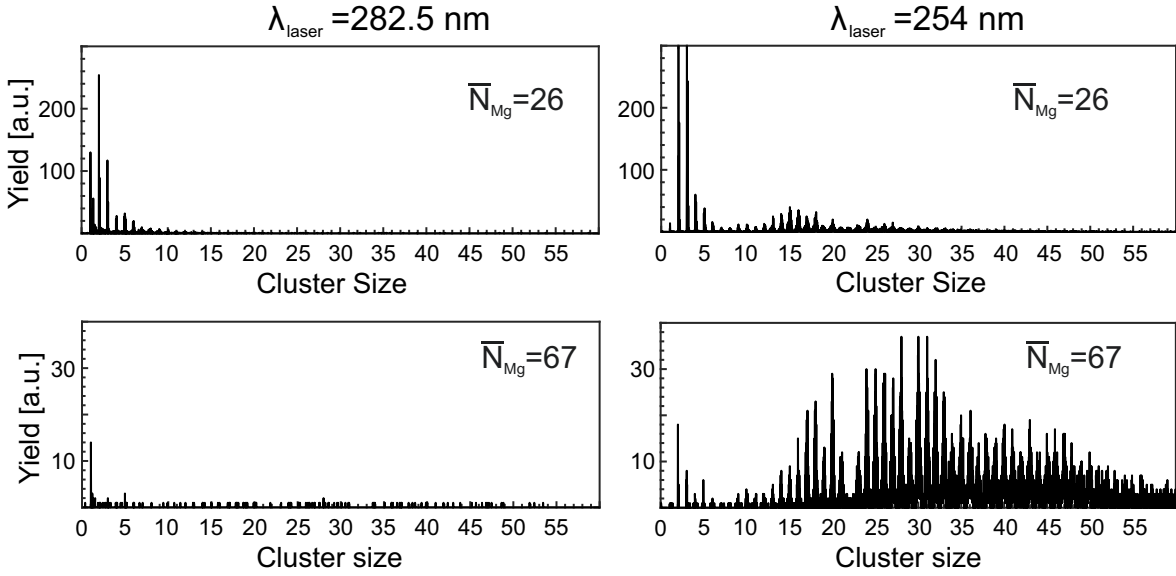
Figure 6.9: Mass spectra of Mg doped droplets for different doping conditions and $\overline{N}_{He}=5.2 \cdot 10^4$, recorded at λ_{foam} (left) and $\lambda_{laser}=254$ nm (right). Signals of Mg$_N$ up to $N=55$ are observed at highest doping conditions.

ion yield Y_{foam}^{ion} at λ_{foam} increases with $\overline{N}_{Mg}$ and maximizes at $\overline{N}_{Mg}=12$ and drops with further increase of $\overline{N}_{Mg}$. In contrast, the yield at shorter wavelength starts to rise when $\overline{N}_{Mg}=10$, i.e., near the maximum of Y_{foam}^{ion} and gradually increases with $\overline{N}_{Mg}$. At the high doping conditions only the signal at $\lambda_{las}=254$ nm is observed. Similar behavior has been observed for different droplet sizes. Only the value of $\overline{N}_{Mg}$ at which the signal of large clusters can be observed and the largest cluster size appear to depend on $\overline{N}_{He}$. This indicates, that the process of cluster formation has the same origin independent on the droplet size.

The formation of Mg$_N$ at high doping level opens an opportunity to study properties of free Mg clusters. The signals of different Mg$_N^+$ as a function of the photon energy E$_{ph}$ gradually increase with E$_{ph}$ up to the level where they maximize and remain constant, see Fig. 6.11. The photon energies, at which the signal levels out, differ for various Mg$_N$. Note, that in the photon energy region $4.5\,\text{eV} \leq \text{E}_{ph} \leq 5.8\,\text{eV}$ no specific absorption features are observed. Thus the obtained ionization efficiency curves allow to determine the IP of Mg clusters. One of the methods is based on fitting the experimental data by an error function (red dashed lines in Fig. 6.11) and will be discussed in the next section.

Figure 6.10: Dependence of the total ion yield on the average doping level taken at laser wavelengths λ_{foam}=282.5 nm (red) and λ_{las}=254 nm (blue). The helium droplet size is $\overline{N}_{He}$=5.2·10^4. Dotted lines are plotted to guide the eyes.
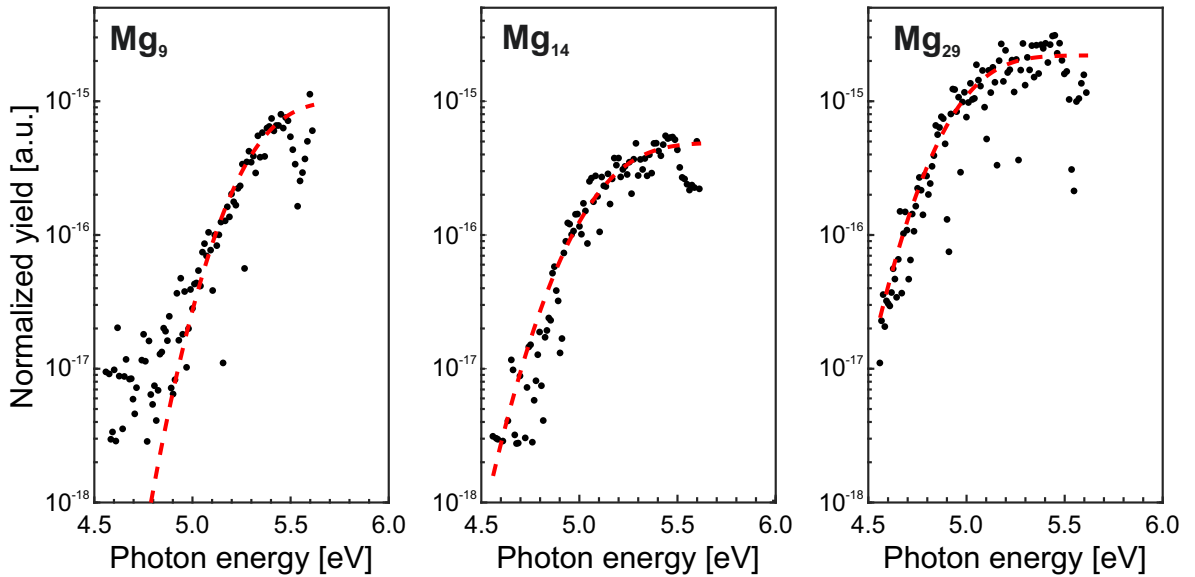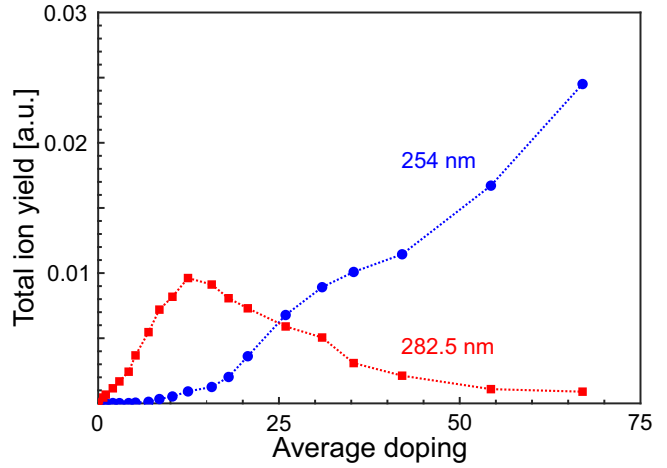
Figure 6.11: Ionization efficiency curves for different clusters. Black dots - experimental data, dashed red lines correspond to the fit, see Ch. 7 for details. The yields are plotted on a logarithmic scale.

7 Discussion

7.1 Photoelectron spectra

Resonant two-photon ionization of Mg atoms in helium droplets at the foam resonance wavelength λ_{foam}= 282.5 nm leads to the emission of electrons with kinetic energies in the range between 1.0-4.5 eV. The spectra show a clearly resolved peak structure, providing evidence, that ionization originates from different excited states. According to the used R2PI scheme, the first photon excites electrons into the 3^1P_1 state of foam atom, whereas the absorption of a second photon leads to ionization. The two-photon regime is confirmed by the dependence of the electron yield Y_e on E_{las}, that is, $Y_e \propto E_{las}^2$ (see Fig. 6.5). Assuming that the target is ionized by a single photon, the electron binding energy E_{bin} in the transient state can be obtained as

$$E_{bin} = E_{ph} - E_{kin} \tag{7.1}$$

where E_{ph} is the photon energy.

Single embedded Mg atom

Examples of photoelectron spectra in the LE region as a function of binding energy are shown in Fig. 7.1. As a reference, the R2PI spectrum of bare Mg atom at laser wavelength λ_{free}=285.2 nm, which corresponds to a free atom resonant transition (Fig.7.1, top). The binding energy E_{bin}^{free}=3.30 eV agree well with that of the 3^1P_1 state. At low doping conditions ($\overline{N}_{Mg}$=0.1) the single peak is centered at E_{bin}=3.22 eV (Fig.7.1, middle). The pick-up statistics predicts that the probability to pick-up more than a single atom is about 0.5 %. Thus, the origin of the electron emission can be assigned to R2PI of single Mg atoms isolated in the droplets and a possible contribution of multiply doped droplets to the PES can be neglected. The peak position shows a shift of about ΔE_{bin}= −80 meV relative to the free atom. This indicates, that the IP is lowered by the helium environment. The value of the shift ΔE_{bin} is in the order of magnitude which is typical for completely solvated atoms. For example, the IP of aniline in a droplet lowers by about 100 meV, whereas for alkali atoms, the IP is shifted by 5-20
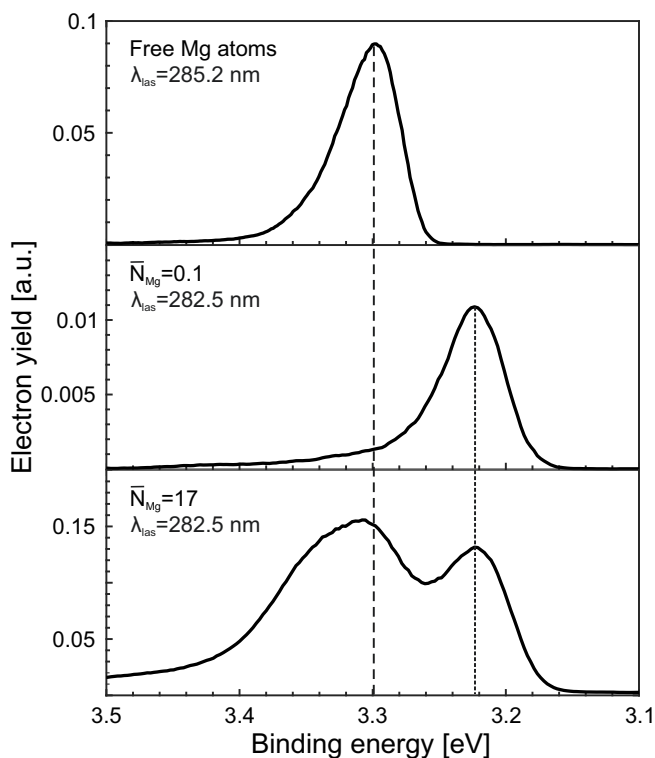
Figure 7.1: The LE region of photoelectron spectra at different doping conditions as a function of binding energy. (Top) The spectrum of bare Mg atoms. (Middle) Single atom doping, $\overline{N}_{Mg}$=0.1. (Bottom) High doping conditions, $\overline{N}_{Mg}$=17. The dashed line indicates the binding energy E_{bin}^{free} of an electron in free atom. Note, that a different wavelengths was used to record spectra of free and embedded atoms, i.e., 285.2 nm and 282.5 nm, respectively.

meV (see Ch. 3). Up to now, the question of Mg atom location is still under discussion. The calculated Ancilotto parameter λ_A, does not provide a clear prediction, since it strongly varies with respect to chosen Mg-He interaction potential (see Tab. 2.1). The calculations predict an interior location [149, 192, 259]. However, experimental investigations give different results, depending on the applied method: LIF and absorption experiments [51, 186] show an interior location of Mg, whereas EII results [260] suggest that the Mg atom resides on the droplet surface. The conclusion of the EII experiments is based on the assumption, that for the surface located atoms Penning ionization gives a strong contribution. Hence, the interpretation of EII results strongly depends on the Penning ionization cross-sections, which may be overestimated. The results obtained in present work, together with light absorption experiments confirm complete solvation of Mg in He droplets.

High doping conditions

Another prominent feature centered at E_{bin}=3.31 eV appears, when droplets are doped with multiple atoms (Fig. 7.1, bottom). The comparison to the spectrum recorded for free atoms shows, that the peak position agrees well with E_{bin}^{free} (Fig. 6.1, top). In

addition, the peak is broadened. This points out, that for droplets doped contains several atoms, at least a part of the atoms is ionized outside the droplet after photoexcitation. The origin of the additional broadening can be attributed to the ionization of excited Mg^*He_n exciplexes. Indeed, a high abundance of Mg^+He_N ions has been reported [51] (see Fig. 3.6) in R2PI. Calculations have shown, that the interaction between the excited $Mg(3^1P_1)$ atom and He is stronger than in the ground state [192]. This implies that attachment of He to Mg^* is more favorable than in the ground state.

Both observed LE features represent the photoemission from the intermediate 3^1P_1 state which is directly accessible by single photon absorption. On the other hand, the HE peaks (see Fig. 6.1) cannot be associated with photoexcitation of Mg atoms at the chosen photon energy. Note, that the HE signatures appear only at conditions when more than one Mg atom is present in the droplet. Values of E_{bin}^{HE} range from 3 eV up to almost the vacuum level. As an obvious assumption, the appearance of the new peaks can be traced back to a possible ionization of clusters, if they are present in the nanodroplets. Indeed, clustering of atoms will reflect in the electronic structure. Consequently, a change in the electron emission as a function of size is expected. Moreover, a wide distribution of cluster sizes will simultaneously be probed in the interaction region. Thus, clusters of different size will give a contribution to the signal. This may lead to a change of the electron spectra comparable to the single atom.

The pick-up dependence of the PES can be used to reveal a possible contribution of clusters. Results are presented in Fig. 7.2, a, for an average droplet size of $\overline{N}_{He}=5.2 \cdot 10^4$ atoms. Initially, the yield of HE electrons increases with the number of Mg atoms and maximizes in the region of a few tens of $\overline{N}_{Mg}$. At high droplet load the HE signal vanishes and only the atomic features remain, but with a significantly lower yield. This dependence does not support the picture of the ionization of compact Mg_N, due to the absence of any new photoelectron peaks at different $\overline{N}_{Mg}$. Lines at lower binding energies only appear at higher doping condition. After the signal shows up, the peaks remain unchanged in their energy positions. This suggests that the observed electrons originate from one and the same particles, that is Mg atoms.

Highly excited states of Mg atoms

To reveal a contribution of atomic excited states, the spectra are compared with the level diagram of Mg [184] (Fig. 7.2, c). Although the spectral resolution is limited, several HE photoelectron features can be assigned to ionization from weakly bound atomic states. Both, singlet and triplet states with the principal quantum number

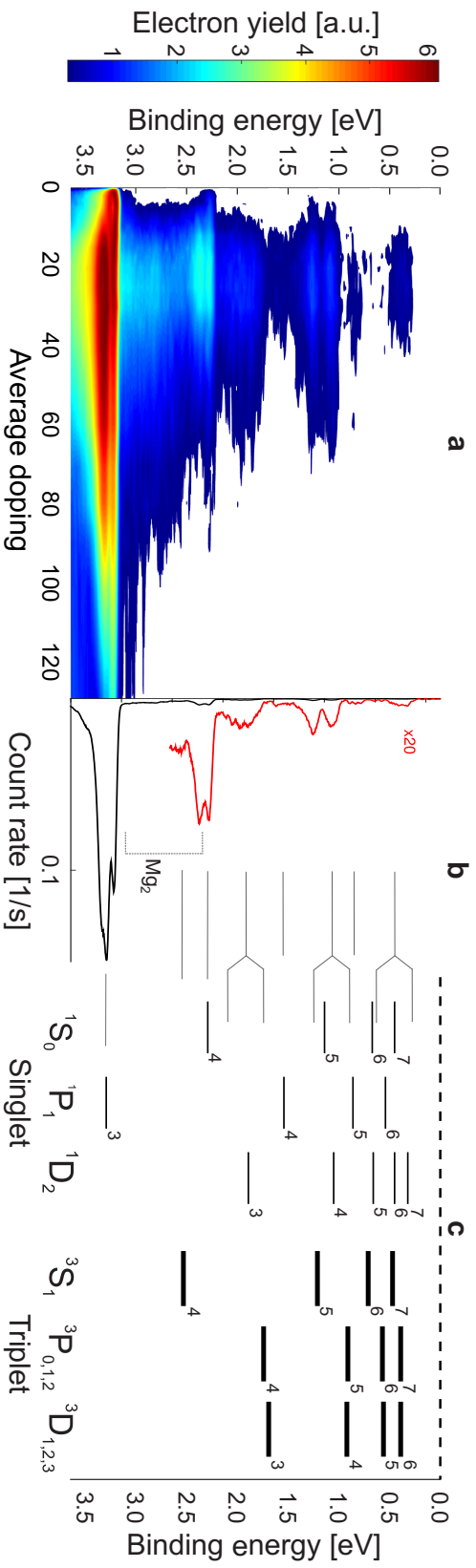**Figure 7.2:** Comparison of the photoelectron spectra (a) with an energy level diagram of Mg atoms[1](c). Panel (b) corresponds to a single spectrum recorded $\overline{N}_{Mg}$=30. Note, that in contrast to Figs. 6.2 and 6.3, the y-scale shows the electron binding energy. Only levels from which single photon ionization possible are depicted. The average droplet size is $\overline{N}_{He}$=5.2·10^4.

n up to 7 contribute to the photoelectron signal. Sharp resolved peaks cannot be obtained due to several reasons. (i) For $E_{bin} < 2$ eV, the density of the states increases, i.e., the energy differences between the levels decreases. The resolution of MB-PES is not sufficient to resolve every peak, since the close lying photoelectron features overlap. (ii) The ionization of snowballs can contribute. Additional helium atoms will lead to a slight shift of the atomic levels due to the weak Mg-He interaction. It is anticipated, that the resulting spectra will have a similar shape with probable small shift and/or broadening. Nevertheless, the observed values E_{bin} agree fairly well with the binding energies of excited states of Mg atoms.

The decrease of the relative intensities with increasing E_{bin} (see Fig. 6.2, right), can be associated with electron relaxation. For excited atomic states, the typical values of the lifetime are in the range of nanoseconds. In the experiment, the time between excitation and ionization is determined by the duration of the laser pulse ($\tau_{laser} = 10$ ns). Thus, a time delay of several nanoseconds is enough for relaxation to occur. This leads to a more efficient photoemission from more strongly bound states. The singlet and triplet systems will undergo relaxation to their lowest electronic states, since singlet-triplet transitions are forbidden by selection rules. On a long time scale, electrons from initial singlet states will find themselves in the ground 3^1S_0 state. Moreover, a part of the atoms will decay through 3^1P_1, which, together with direct ionization, will give an additional contribution to the electron yield at $E_{bin} = 3.3$ eV. For the triplet system, the lowest state is $3^3P_{0,1,2}$ (not shown in the diagram in Fig. 7.2) with $E_{bin} = 2.71$ eV. Due to the low probability of a transition into the singlet ground state, electrons can accumulate in this metastable state, which has a lifetime of milliseconds. However, the photon energy $E_{ph}^{foam} = 4.39$ eV is not sufficient to ionize atoms from this electronic state, and therefore $3^3P_{0,1,2}$ state cannot be probed by a single wavelength experiment.

A broad electron distribution is obtained in the range between 3.0-2.4 eV, with two peaks centered at 2.29 eV and 2.38 eV. Only the feature at 2.29 eV can be attributed to an atomic level, i.e. 4^1S_0. The 4^3S_1 state cannot be assigned to the peak at 2.38 eV, since the corresponding binding energy is 160 meV off[2]. A possible origin is the ionization of excited Mg_2, in particular from $A^1\Sigma_u^+$ and $(1)^1\Pi_u$ [199]. Taking the ionization potential $IP(Mg_2) = 6.35$ eV into account, the corresponding binding energies are $E_{bin}^{dimer}(A^1\Sigma_u^+) = 3.1$ eV and $E_{bin}^{dimer}((1)^1\Pi_u) = 2.85$ eV. Note, that $(1)^1\Pi_u$ state has been

---

[1]This figure has been published in [261].

[2]The photoelectron emission from 4^3S_1 state can also take place, but the peak is covered by the broad signal.

examined indirectly, and therefore the significant deviation of value of $E_{bin}^{dimer}((1)^1\Pi_u)$ can be expected. Theory predicts a value of $E_{bin}^{dimer}((1)^1\Pi_u)$=2.57 eV [262]. Nevertheless, the provided photon energy is sufficient for ionization of Mg_2^* from both states.

The ionization from the $A^1\Sigma_u^+$ state can give a contribution to the broad electron signal, since different rovibrational levels can be initially occupied. The energy of the photoelectrons will be close to those emitted from atomic 3^1P_1 state and, thus, can be covered by the atomic peak. On the other hand, the ionization from $(1)^1\Pi_u$ can lead to a peak at E_{bin}=2.38. Since the transition probability into the ground state is rather low, one can expect a long lifetime of the $(1)^1\Pi_u$ and, thus, a high ionization yield. The difference between E_{bin}=2.29 eV in the present experiment and the binding energy of $E_{bin}^{dimer}((1)^1\Pi_u)$=2.54 eV can be related to the uncertainty in available data of the $Mg_2((1)^1\Pi_u)$ potential and the IP of Mg_2. Taking this into account, the observed feature may be assigned to emission from $(1)^1\Pi_u$ state. It cannot be excluded, that small clusters can give a contribution to the signal in the envisioned energy range. However, no experimental data on the optical spectra and level structure of small Mg_N are available. This does not permit the assignment of the contribution of specific sizes to the broad photoelectron feature in the range 3.0 eV$\leq E_{bin} \leq$2.4 eV.

Photoelectron emission at different wavelengths

Total photoelectron yields Y_e are similar as a function of laser wavelength for HE and LE regions and no fine structure has been observed (see Fig. 6.6). Moreover, the wavelength dependence of Y_e is analogous to the R2PI spectrum obtained by mass spectroscopy (Fig. 3.7) [51]. The similarities in the absorption line shape and the peak positions implies that the all observed PES features correlate with the ion signal. Hence, the photoelectron emission originates from ionization of Mg, $MgHe_N$ and Mg_N. Photoemission spectra recorded within the absorption, show that the peaks remain at the same E_{bin}. However, several new peaks appear at λ_{las}=278 nm, λ_{las}=281 nm and in the region 279-281 nm, see Fig. 7.3.

Since the HE electrons are predominantly emitted from highly excited states of the Mg atom, the observed features may have similar origin. The features at F_{278} and F_{281} represent ionization of Mg atoms though additional intermediate states. Near 281 nm, the observed feature can be attributed to the 3s3d $^3D_{1,2,3} \leftarrow$ 3p3d $^3D_{1,2,3}^o$ transition, i.e. $^3D_1 \leftarrow {}^3D_1^o$ (281.178 nm), $^3D_2 \leftarrow {}^3D_2^o$ (281.112 nm) and $^3D_3 \leftarrow {}^3D_3^o$ (280.976 nm) [184]. A closer inspection of the F_{281} feature (Fig.6.8, a) reveals three peaks. The corresponding Gaussian fits shows peak positions at 281.20 nm, 281.12 nm and 280.99 nm. This
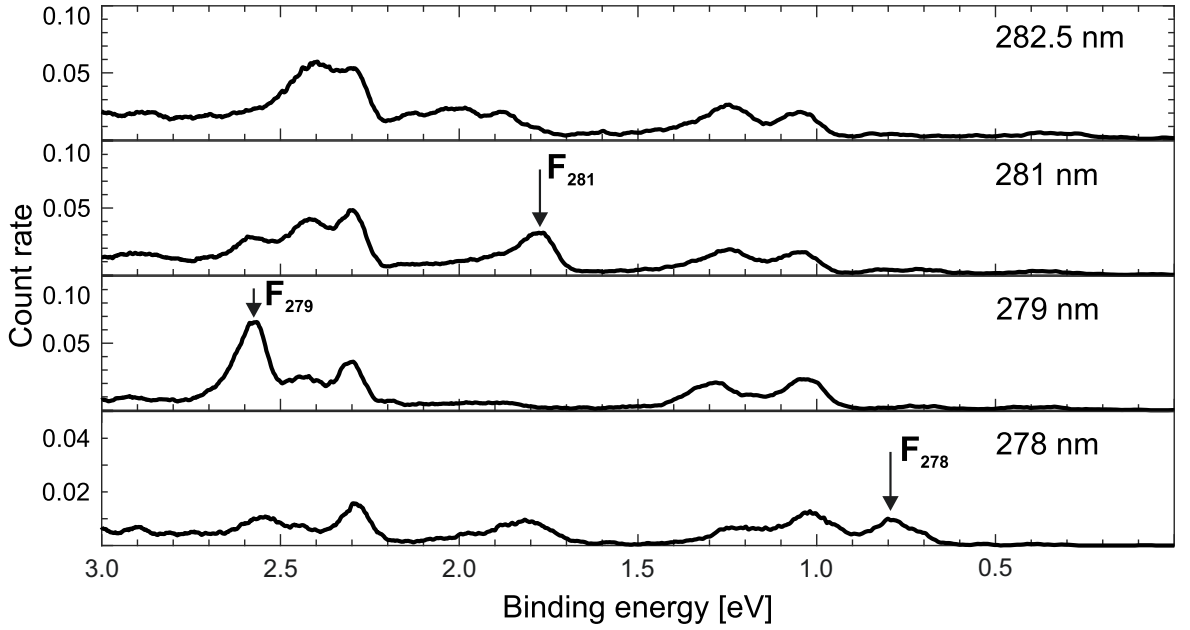
Figure 7.3: Photoelectron spectra recorded at different wavelengths within the Mg foam absorption. Note, that in contrast to Fig. 6.7, now the electron yield is plotted as a function of binding energy. Characteristic features observed at 281 nm, 279 nm, 278 nm are labeled by arrows. Values of the corresponding E_{bin} as well as responsible transitions are summarized in Tab. 7.1.

values are in good agreement with known transition wavelengths. With respect to E_{bin}, the observed value of $E_{bin}^{281}=1.78$ eV is only slightly shifted relative to the binding energy of the $3p3d\,^3D^o_{1,2,3}$ state[3] (1.71 eV). Another prominent feature F_{278} ($\lambda_{las}= 278$ nm) is observed at $E_{bin}^{278}=0.80$ eV. As in the previous case, it can be assigned to a second excitation from an already excited state $3s3p\,^3P^o_{1,2,3}$, i.e. $3s3p\,^3P^o_{1,2,3} \leftarrow 3p^2\,^3P_{1,2,3}$. In particular, two transitions can participate: $3s3p\,^3P^0_2 \leftarrow 3p^2\,^3P_2$ (277.983 nm) and $3s3p\,^3P^0_1 \leftarrow 3p^2\,^3P_1$ (277.982 nm). However, the value of E_{bin}^{278} of F_{278} is shifted by about 0.3 eV with respect to the binding energy of $3p^2\,^3P_{1,2,3}$ ($E_{bin}(3p^2\,^3P_{1,2,3})=0{,}48$ eV). A closer inspection near 278 is not possible, due to the limit in scanning range of the dye laser system. Despite this, the observed transition is sharp, which is characteristic for atoms and therefore the feature F_{278} can be assigned to the above mentioned transition.

---

[3]Note, that the photon energy is sufficient to ionize the Mg atom from the initial $3s3d\,^3D_{1,2,3}$ state. Levels of the doubly excited np3d sequence are lying above the ionization limit of neutral Mg and converge to an another IP, corresponding to the excited state of Mg^+ [185]. In the present case, the new value is $IP(Mg^+(3p\,P^0_{1/2}))=12.08$ eV. See also Fig. 3.4

Peak	E_{bin}, eV	λ_{las}, nm	$\Delta\lambda$, nm	Transition
		281,20 (281.178)	0.043	$3s3d\,^3D_1 \leftarrow 3p3d\,^3D_1^o$
F_{281}	1,78 (1.71)	281,12 (281.105)	0.082	$3s3d\,^3D_2 \leftarrow 3p3d\,^3D_2^o$
		280,99 (280.976)	0.055	$3s3d\,^3D_3 \leftarrow 3p3d\,^3D_3^o$
F_{279}	2.58	279.50	1.5	Possible Mg_n
F_{278}	0.80 (0.48)	278.00 (277.983)	-	$3s3p\,^3P_{1,2,3}^o \leftarrow 3p^2\,^3P_{1,2,3}$

Table 7.1: Summarized values of binding energies, wavelengths, peak widths as well as assigned transitions of photoelectron features F_{281},F_{279}, F_{278}. Binding energies and wavelengths given in brackets correspond to the expected values taken from NIST database [184].

In contrast to F_{278} and F_{281}, the feature F_{279} (λ_{las}=279 nm) at E_{bin}^{279}=2.58 eV cannot be associated with any Mg excitation. Moreover, the peak remains in the spectra within a broad wavelength range of $\Delta\lambda$=1,5 nm (see Fig.6.8, b). However, the value of E_{bin}^{279}, the wavelength dependence of Y_e and the observation of cluster ions, suggest that photoemission from small clusters can be responsible for F_{279} peak. In particular, the peak position can be associated with the electron emission from[4] Mg_2 (see above).

Excited Mg atoms after the photoabsorption

It is not possible to explain a population of highly excited states by absorption of any number of photons after the initial $3\,^1P_1 \leftarrow 3\,^1S_0$ photoexcitation. At λ_{foam} no additional transitions can take place [184]. High order nonlinear optical processes can be excluded as well, since the dependence of Y_e on laser wavelength shows a dependence characteristic for two-photon processes and no additional photoelectron peaks or energy shifts have been observed (see Fig. 6.5).

Excitation and ionization through doubly excited states of Mg atoms give additional evidence that the observed electron emission with low E_{bin} originates from highly excited states of Mg atoms. Both observed resonances confirm that atoms in triplet states are probed. Moreover, the $3s3p$ $^3P_{1,2,3}^o \leftarrow 3p^2\,^3P_{1,2,3}$ transition, indicate the presence of atoms in the lowest $3s3p$ $^3P_{1,2,3}^o$, from which atoms cannot be directly ionized by photons at λ_{foam}.

The results presented above strongly suggest that dynamical processes are triggered

---

[4]Unfortunately, the present experimental setup does not allow to clearly determine the origin of the F_{279} feature. The assignment to specific cluster size might be done by, e.g., electron-ion coincidence spectroscopy [263].

by photoexcitation. This can be related to the foam collapse [51]. The view is supported by the wavelength dependence of Y_e, being similar to the R2PI spectrum obtained by mass spectroscopy. In contrast to the studies based on ion spectra, the PES provides insight in the energy released in the collapse. According to the photoelectron signatures, an energy transfer up to several electronvolts to a single atom takes place. Possible involved mechanisms will be discussed in Sec. 7.3.

Dependence of HE emission on droplet size

The change of the average doping has no impact on the photoelectron spectra, except that the electron yields from weakly bound states depend on $\overline{N}_{Mg}$ (see Fig. 6.4). The shapes of the photoelectron spectra show no change with the droplet size. Only the doping range, within which the HE emission can be observed, varies with $\overline{N}_{He}$. That implies that the general process of the formation of highly excited atoms is independent on the size of the droplet. However, the number of participating atoms depends on $\overline{N}_{He}$.

The analysis of the data with respect to the pick-up statistics provides a tool to reveal the size of the foam, for which the photoemission from highly lying states can be observed. This method is suitable for two purposes: (i) Revealing a specific foam size N_{Mg} responsible for HE photoemission. It is anticipated, that the photoelectron yields will follow the pick-up probability of N_{Mg} for different $\overline{N}_{Mg}$. (ii) If the droplets contain foams of different sizes simultaneously contribute to the HE signal, the corresponding range $N_{min} \leq N_{Mg} \leq N_{max}$ can be revealed.

As discussed in Ch. 2, the probability to capture atoms by a single droplet P_k is determined by the Poisson statistics (Eq. 2.12). For the present work, it is assumed that the signal originating from a single foam size is proportional to P_k for an average doping $\overline{N}_{Mg}$. The values of $P_k(\overline{N}_{Mg})$ are calculated for droplets within the size distribution which is determined by the source conditions used in experiments. At source temperatures $T_0 \geq 10\,\text{K}$ ($\overline{N}_{He} \leq 3.6 \cdot 10^4$), the droplets are produced under sub-critical conditions and thus have a log-normal distribution. For temperatures of $9.8\,\text{K}$ ($\overline{N}_{He} = 5.2 \cdot 10^4$) and $9.5\,\text{K}$ ($\overline{N}_{He} = 1.2 \cdot 10^5$), the expansion conditions are critical and the distributions became bimodal. In this regime, the exact form of the distribution is undefined making a prediction challenging. However, a change of T_0 in the critical regime affects on the contributions of the log-normal and linear-exponential parts. Close to the subcritical regime, the log-normal part has a stronger impact. Hence, the size distribution for the lowest temperatures is assumed to be log-normal as well. The
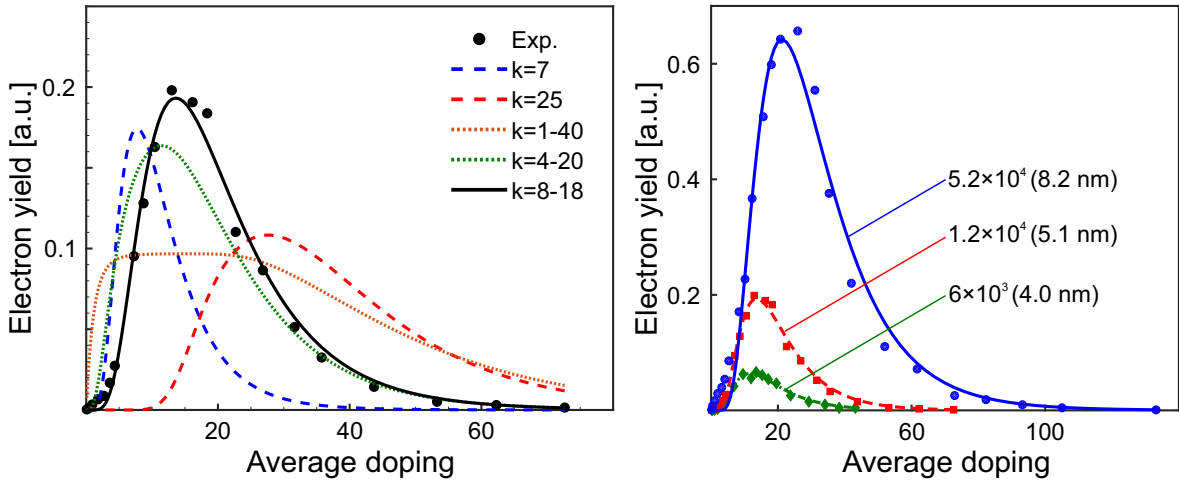
Figure 7.4: (Left) Total electron yield ($E_{bin} \leq 2.25$ eV) as function of $\overline{N}_{Mg}$ fitted with respect to the pick-up statistics for different numbers of Mg atoms and $\overline{N}_{He}$=1.2·10^4. The dashed lines correspond to single foam sizes, k=7 and 25. The dotted lines show fits which include foam size ranges, e.g. $1 \leq N_{Mg} \leq 40$ and $4 \leq N_{Mg} \leq 20$. The best fit ($8 \leq N_{Mg} \leq 18$) is shown by the black solid line. (Right) Total photoelectron yields ($E_{bin} \leq 2.25$ eV) for droplet sizes 5.2·10^4 (blue dots), 1.2·10^4(red squares), 6·10^3 (green diamonds). The numbers in brackets correspond to mean droplet radius r_{drop}. The best fits are shown as lines of the corresponding colors[5].

total probability of creating a foam with size N_{Mg} in the pick-up region is therefore taken as a superposition of the probabilities with respect to the abundance of each droplet size. The obtained function $P_k(\overline{N}_{Mg})$ is fitted to the experimental data. Note, that the foam size or size ranges are the only free parameters in the fitting procedure.

As a first step, only a single foam size N_{Mg} was used in the fit procedure. An example is shown in Fig. 7.4, left. Strong deviations of the predicted dependence to the experimental data for N_{Mg} in between 1 and 120 for all $\overline{N}_{He}$ are obtained. Hence, no specific foam size can be identified to be responsible for the observed HE features. The findings suggest, that different N_{Mg} contribute to the signal. In order to prove this, similar procedure including a size range $N_{min} \leq N_{Mg} \leq N_{max}$ has been applied. The results are shown in Fig. 7.4, left for a chosen size ranges together with the best fit. The optimal size range varies for different droplets sizes. The comparison of the optimal fits for different $\overline{N}_{He}$ shows that the size range depends on the droplet size (Fig. 7.4, right).

---

[5]Right panel of this figure has been published in [261].

$\overline{N}_{He}$	r_{drop}, nm	N_{min}	N_{max}
$3.3 \cdot 10^3$	3.3	5	15
$5.7 \cdot 10^3$	4.0	6	17
$1.2 \cdot 10^4$	5.1	8	18
$3.6 \cdot 10^4$	7.4	9	25
$5.2 \cdot 10^4$	8.2	12	29
$1.2 \cdot 10^5$	11.0	12	49

Table 7.2: Values of N_{min} and N_{max} extracted from the fits for different average droplets sizes $\overline{N}_{He}$. The corresponding average radii of the droplets r_{drop} are given in the second column.

Figure 7.5: Minimal (blue) N_{min} and maximum (red) N_{max} numbers of Mg atoms participating in high energy electron emission process as function of mean droplet radius. Solid and dashed lines correspond to the fit[6].
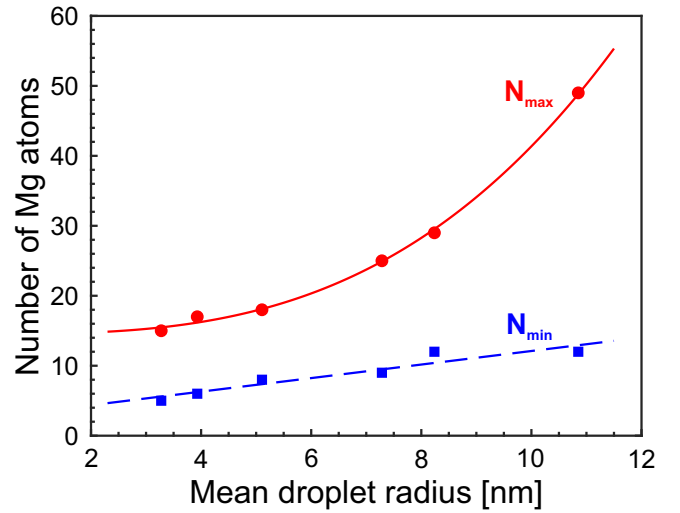
The obtained values of N_{min} and N_{max} extracted from the fits are summarized in Tab. 7.2 and shown in the Fig. 7.5 as function of droplet radius r_{drop}. The minimal number N_{min} indicates the onset of HE emission and is found to increase linearly with droplet radius. This implies, that a certain number of atoms is required to promote electrons in a highly excited states. In opposite to N_{min}, the value of N_{max} represents a limit, after which HE photoelectrons cannot be longer observed. N_{max} is attributed to the largest number of Mg atoms which can be stabilized in the foam within helium nanodroplets of a given size. Hence, one must assume, that adding additional Mg atoms to the foam after N_{max} leads to a spontaneous collapse. The resulting compact structure cannot directly be ionized at λ_{foam}, or the photoionization cross-section is strongly reduced and therefore photoelectron emission cannot be observed. Fig.7.5 shows that N_{max} strongly increases with the droplet size, i.e., proportional to r_{drop}^3.

7.2 Stability of Mg foam

The question of foam stability has been in the focus of theoretical works [149, 198], where calculations were performed for the situation of two and three embedded atoms. DFT simulations [149] show, that the lifetime of two weakly bound Mg atoms in a He$_{1000}$ droplet is in the range of few nanoseconds and can be up to[7] 0.1 ms, when the two-atom system has an angular momentum. Path integral method [198] calculations, applied to He$_{100}$ and He$_{200}$ droplets, show that for two atoms a short-living system can be created as well, whereas for three Mg atoms no stable configuration has been found. These partly contradictory results do not agree with the experiment and require more detailed studies. For example: (i) In both works, the droplet size was smaller than in the experiments. Moreover, in [198] the droplet radius is even comparable to the foam size. Droplets of more realistic sizes, e.g., which are used in the experiments would allow a direct comparison between theory and experiment. (ii) The choice of the Mg-He potential can have a strong impact on the calculated foam stability. (iii) Since the pick-up is a sequential process, every Mg atom will induce a rearrangement of the helium upon the collision and foam formation. Therefore, the simulation of the dynamics of the foam formation appears to be essential.

The experimental results show that droplets containing far more than two atoms give

---

[6]This figure has been published in [261].

[7]Note, that typical times which droplets need to arrive the interaction region after the pick-up is in the range of milliseconds.

a contribution to the photoelectron signal. Moreover, the value of N_{max} represents a stability limit and implies, that increasing the foam size modifies the total interaction between the constituents and leads to an unstable configuration or a reduced lifetime of the foam. For example, a decrease of the potential barrier height will lead to an increase of the probability of Mg tunneling through the barrier. When the depth of the potential well reduces to values close to $T_{droplet}$, the system can undergo a transition into a compact cluster. If the stability of the foam would be determined by N_{Mg} only, no dependence on droplet size is expected. However, this assumption is not supported by the experiment. Hence, one can conclude, that both N_{Mg} and N_{He} play a role in Mg foam stability.

Geometrical effects in Mg foam stability

Figure 7.5 shows, that N_{max} scales as r_{drop}^3, which indicates that the maximum number of Mg atoms participating in photoemission is related to the droplet volume V_{drop}. Therefore N_{max} can be attributed to the geometrical size of the foam. Assuming that Mg atoms are uniformly distributed in the droplet, the volume occupied by the foam can be estimated as

$$V_{foam} = \frac{4}{3}\pi r_{foam}^3 \tag{7.2}$$

where $r_{foam} = r_{Mg-Mg} \cdot N_{Mg}^{1/3}$. The ratio $\mathcal{R} = V_{foam}/V_{drop}$ is shown in Fig. 7.6 (blue) as a function of droplet radius. The value of $\mathcal{R}$ decreases from 0.43 to 0.04 for $N_{He} = 3.3 \cdot 10^3$ and $N_{He} = 1.2 \cdot 10^5$, respectively. For all droplet sizes, the foam is not large enough to completely occupy the droplet interior. The droplet surface layer of 6 Å may reduce the effective volume for foam formation. When the foam extends up to the surface layer, additional atoms have to localize in the surface region. A stabilization of these atoms is expected to be less favorable due to the lower helium density. The corresponding ratio[8] is shown in Fig. 7.6 (red). For the smallest droplets, the foam occupies about 80% of the inner droplet, whereas for the largest one it is only about 5%. Hence, foams with N_{max} do not completely occupy the droplet volume. As another possible structure, a planar configuration has to be considered. For the foam atoms located in the cross-section of the droplet, the value of N_{max} will scale as r_{drop}^2. In this case, the calculated values of the maximum foam atoms vary from 10 for $N_{He} = 3.3 \cdot 10^3$ up to 117 for $N_{He} = 1.2 \cdot 10^5$ and do not match to the experimental values of N_{max}.

---

[8]Here the droplet volume is calculated as $V_{drop} = \frac{4}{3}\pi(r_{foam} - r_{surf})^3$, where $r_{surf} = 6$ Å.
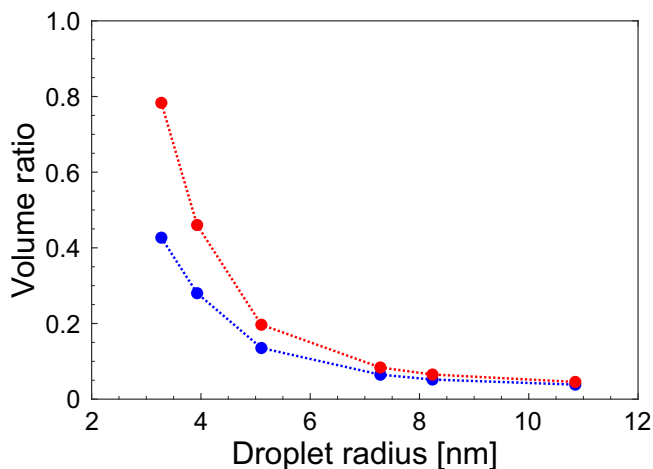
Figure 7.6: Ratio of foam volume V_{foam} to droplet volume V_{drop} as function of droplet radius, excluding (blue) and including (red) the surface layer. The volume of the foam is calculated by Eq. 7.2 taken N_{max} for a given droplet radius r_{drop}. The lines are used to guide the eyes.

That leads to the conclusion, that the geometrical size of the foam is not responsible for the N_{max} limit. It should be noted that for the above mentioned calculations a uniform distribution of atoms in the droplet has been assumed. Probably, the foam may growth non-uniformly or be displaced with respect to the droplet center. Evidence for non-symmetrical growth has been observed in [193], where surface located Mg atoms have been detected[9], even at doping conditions lower than in present work.

Another possible scenario, which can indirectly be related to the droplet size, is stabilization of Mg atoms in quantum vortices. Indeed, foreign atoms can enter and successfully reside in the vortex core [44, 85, 88]. When only a single atom per core in the vortex lattice is present, one can expect a system of weakly interacting and spatially separated atoms, similar to the foam. Thus, the number of atoms which can be stabilized is limited by the number of vortices N^v_{max}. Note, that N^v_{max} depends on the droplet size. For example, Ancilotto *et al.* have calculated that $N^v_{max} = 9$ vortices can be found in droplet of size $N_{He} = 1.5 \cdot 10^4$ [86]. Since vortices align parallel to the rotation axis and hit droplet surface perpendicularly, a scaling of N^v_{max} as r^2_{drop} is expected. Therefore aggregation of Mg atoms in vortices can be excluded[10].

---

[9]See also Ch. 3.3

[10]The possible formation of spatially separated structures in rotating droplets seems to be of high interest. Consequently, the optical response may have a foam-like signature giving specific features in PES similar to observed in this work. Thus, it opens an opportunity to an experimental observation of quantum vortices in small helium nanodroplets, which has not been reported so far.

Impact of doping process on foam stability

Evaporative cooling after the pick-up of atom leads to a decrease of droplet size. Ultimately, the helium shell is completely evaporated after a certain number of pick-up events. Reducing the droplet size may be an additional reason for the foam size limit N_{max}.

The total excess energy E_r transferred to the droplet can be estimated by Eq. 2.16. In the case of the foam, the main contribution to E_r is the collision energy, since the binding energy of atoms in the foam is $E_{bin}^{Mg-Mg}=4\,\text{K}$ (0.35 meV) and Mg-He binding energy $E_{bin}^{Mg-He}=40\,\text{K}$ (3.5 meV). The mean collision energy depends on the kinetic energies of the Mg atoms and the droplet speed (see Eq. 2.18). The lowest temperature of the oven used in experiments is $T_{oven}=504$ K, which corresponds to a mean kinetic energy of $E_{kin}^{Mg}=65$ meV, whereas for the highest $T_{oven}=662$ K it is $E_{kin}^{Mg}=86$ meV. For the helium beam a speed of about $v_{He}=300\,\text{m/s}$ can be assumed[11] ($T_s=15\,\text{K}$) [64]. Therefore, according to Eq. 2.16, the maximum energy transferred has a value of $E_r=100\,\text{meV}$. This corresponds to about $\Delta\text{N}_{He}=160$ evaporated atoms per one Mg atom.

When the droplet is doped by N_{Mg}^{max} atoms it looses $\Delta N_{He}^{tot}=\text{N}_{Mg}^{max}\cdot\Delta N_{He}$ atoms in total and reduces the droplet sizes from $\Delta N_{He}^{tot}=2.4\cdot10^3$ and $7.8\cdot10^3$ for $\overline{N}_{He}=3.3\cdot10^3$ to $\overline{N}_{He}=1.2\cdot10^5$, respectively. For all droplet sizes, these values are lower than the actual mean droplet size. The size reduction for the smallest droplets is significant, whereas for the largest droplets the impact on droplet size is negligible (about 6.5 %). Hence, evaporative cooling may affect the maximum foam size for small droplets, but no impact is expected for the large ones.

Another possible reason for foam destruction can be related to the dynamical processes triggered by collisions of Mg atoms with the nanodroplet. Theoretical investigations have have been conducted for Cs [264], Xe [265] and Ne [266] at different impact conditions. As a result of the collision, collective excitations, e.g., phonons, ripplons, rotons, vortices, are induced. This leads to strong density waves propagating through the droplet interior. In dependence on the droplet-dopant interaction and collision energy, different scenarios can be realized: (i) The dopant atom reflects back from the droplet surface at low collision energies; (ii) Particle pass through the droplet and expels from the opposite side; (iii) The dopant atom successfully coagulates and bounces

---

[11]For $T_s=15\,\text{K}$ the speed has a highest value. The speed of the droplet beam decreases with reducing the source temperature.
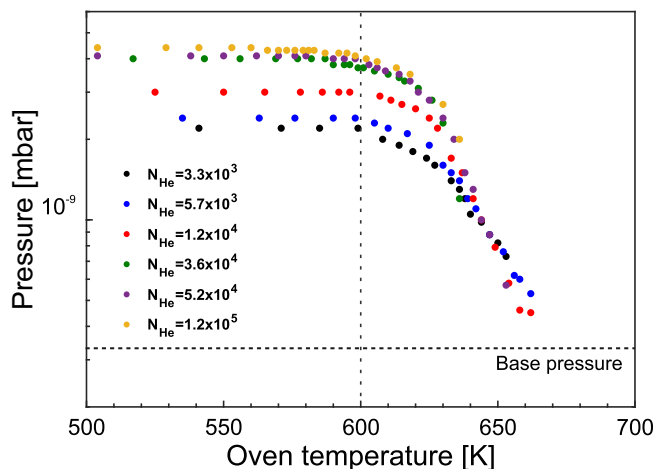
Figure 7.7: Vacuum pressure P_{TOF} in the TOF region as a function of oven temperature, for different droplet sizes.

between the inner surfaces of the droplet, while it speed reduces below Landau critical velocity.

It seems favorable, that at high collision energies, the impact of the Mg atom induces a strong disturbance in the droplet and the foam structure disintegrate. This would lead to the formation of a compact cluster. Consequently, the release of binding energy will lead to He evaporation. One can expect, that this process will induce a strong reducing of the droplet size. Hence one can expect to obtain evidence for this by monitoring the evaporation of He atoms.

The vacuum pressure P_{TOF} in the TOF-spectrometer chamber can serve as an experimental tool to measure a decrease of the droplet size [62]. The choice of the P_{TOF} is reasonable, since the helium droplet beam hits the end of the vacuum machine in the corresponding chamber (see Fig. 5.1), which leads to complete droplet evaporation. The detected partial pressure of He is related to the particle density of the molecular beam. Hence, a depletion of the droplet beam upon propagation is reflected in a decreasing[12] P_{TOF}.

For a given droplet size, only the kinetic energy of the Mg atoms, defined by the oven temperature, has an influence on the collision energy. The value of P_{ToF} as a function of the oven temperature T_{oven} is shown in Fig. 7.7. For all droplet sizes, no change in P_{TOF} is observed up to $T_{oven}^{crit} \approx 600\,\mathrm{K}$. But for higher temperatures, P_{TOF} rapidly decreases. This indicates an increase of droplet evaporation. The oven temperature dependence suggests, that for $T_{oven} > T_{oven}^{crit}$ the impinging Mg atoms produce a strong disturbance of the helium environment, which possibly leads to the foam collapse.

---

[12]Note, that a similar method has been used to obtain average droplet sizes [62] and sizes of embedded clusters [106].

Figure 7.8: Dependence of P_{TOF} on excess energy E_r for different dopant atoms. Droplet size $\overline{N}_{He}$=3.6·10⁴. (blue) Mg foam formation is assumed, i.e. the binding energy of Mg clusters is excluded from E_r. (red) Xe atoms. (green) Ag atoms. (black) Mg clusters formation is assumed, i.e. E_r is calculated by including the atomic binding energy in Mg clusters. Lines are used to guide the eyes.
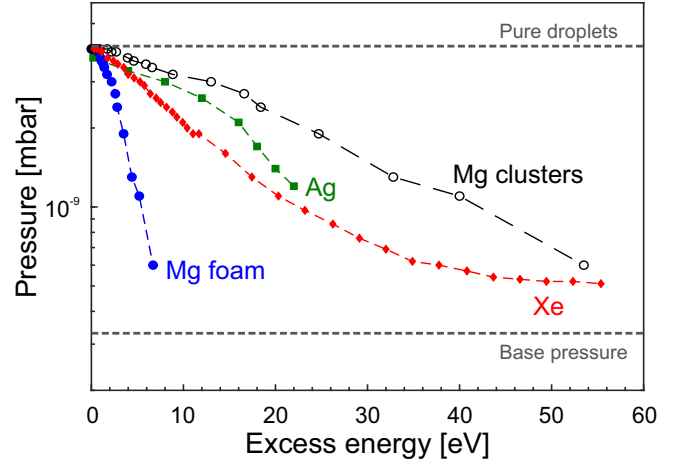
In general, evaporative cooling leads to a decrease of droplet size. Moreover, for different droplet sizes, the same T_{oven} will correspond to different $\overline{N}_{Mg}$. Higher values of $\overline{N}_{Mg}$ will be obtained for larger droplets for the same T_{oven}. In order to reveal the impact of evaporative cooling on P_{TOF}, the dependence of P_{TOF} on E_r is compared to other dopants (Xe, Ag) for the same droplet size $\overline{N}_{He}$=3.6·10⁴, see Fig. 7.8. Xenon was chosen because of two reasons: (i) The mean collision energy does not depend on the average doping, since no oven is required. (ii) The binding energy between Xe atoms is low and an evaporation of ΔN_{He}=250 atoms can be assumed [267]. The experimentally observed dependence $P_{TOF}^{Xe}(E_r)$ (Fig. 7.8, red) shows a gradual decrease starting from E_r=1.1 eV. At high doping level (E_r=40 eV) P_{TOF}^{Xe} levels out. The corresponding total number of evaporated atoms is ΔN_{He}=6.4·10⁴, which is higher than $\overline{N}_{He}$, indicating that all droplets in the beam are completely evaporated. The remaining difference between P_{TOF} and the base pressure is caused by an increase of the residual gas pressure in the TOF-chamber during the operation. In contrast to Xe, doping with silver atoms requires a high T_{oven}. In addition, the binding energy of Ag atoms in the clusters is higher. An excess energy of E_r=2 eV per Ag atom can be assumed [33], which corresponds to ΔN_{He}=3200. The P_{TOF}^{Ag} follows a similar behavior as in the Xe doping case (Fig. 7.8, green). But starting from E_r=4 eV, a difference between P_{ToF}^{Ag} and P_{ToF}^{Xe} is observed. The lower values of P_{TOF}^{Xe} are caused by spatial scattering of the He beam by Xe atoms [193], which impedes the total number of droplets reaching the end of the vacuum chamber. This lead to an additional decrease in P_{TOF}^{Xe}, since a higher number of collisions takes place compared to silver[13].

---

[13]For example, E_r=20 eV corresponds to a pick-up of 125 Xe atoms, but only 10 silver atoms.

For Mg foam, only the collision energy of $100\,\text{meV}$ is taken into account (Fig. 7.8, blue). The value of P_{ToF}^{Mg} rapidly declines with increasing E_r, reaching a lowest value[14] at E_r=6.7 eV. This energy value corresponds to $\Delta N_{He} \approx 1.1\cdot 10^4$. In contrast, for Xe doping the same value of P_{ToF} is reached at E_r=35 eV ($\Delta N_{He} \approx 5.6\cdot 10^4$). The number of evaporated atoms is not sufficient to completely evaporate a droplets with $\overline{N}_{He}$=3.6$\cdot 10^4$. The impact of the spatial scattering is expected to be lower in Mg than in Xe doping by two reasons: (i) The total number of collisions is lower for Mg doping (e.g. N_{Mg}=67 versus N_{Xe}=219 at P_{ToF}=6.2$\cdot 10^{-10}$ mbar.). (ii) The momenta of Mg atoms are smaller than for Xe. This implies, that an additional energy source, e.g. the spontaneous foam collapse in part of droplets, leads to an increase of E_r and therefore strong depletion of the helium beam.

Interestingly, the dependence of P_{TOF}^{Mg} on E_r provides additional confirmation of the foam formation hypothesis. If only Mg clusters would form, higher values of E_r have to be assumed, since the ground state binding energy E_{bin} of atoms in the clusters have to be taken into account. Taking into account spatial scattering, one can thus expect that $P_{TOF}^{Mg}(E_r))$ would have a values between $P_{ToF}^{Xe}(E_r))$ and $P_{ToF}^{Ag}(E_r))$. The dependence of P_{ToF} on E_r by including $E_{bin}(\text{Mg}_N)$ [268] to E_r is shown in Fig.7.8 (black). Clearly, the Mg doped He beam is less depleted compared to Xe and Ag doping. Hence, the actual energy release is much lower than predicted. Hence, Mg clusters do not form upon the pick-up of Mg atoms. Only with increasing of $\overline{N}_{Mg}$, part of the droplets is destroyed by the spontaneous collapse of the foam.

7.3 Light induced implosion of Mg foam

The results obtained by PES suggest an energy redistribution after photoexcitation, whereas the efficiency depends on the number of particles in the droplet. The stability of the foam is governed by the number of atoms as well. Combining the finding described above, two general scenarios of the behavior of the Mg doped droplets after the pick-up can be deduced, which are shown schematically in Fig. 7.9. (I) $N_{Mg} \leq N_{max}$, stable foam. Photoabsorption in this regime induces a collapse. The result of the collapse depends on N_{Mg}: (Ia) $N_{Mg} < N_{min}$. Photoelectron spectra show characteristic features (LE-emission), which are assigned to ionization from 3^1P_1 state of Mg atoms and Mg*He$_n$ snowballs. (Ib) $N_{Mg} \geq N^{min}$. HE photoelectron features show up, indicating ionization of Mg atoms from highly excited states ($E_{bin} \geq 3$ eV). (II)

---

[14]This value of E_r correspond to the highest doping achieved in the experiments for $\overline{N}_{He}$=3.6$\cdot 10^4$
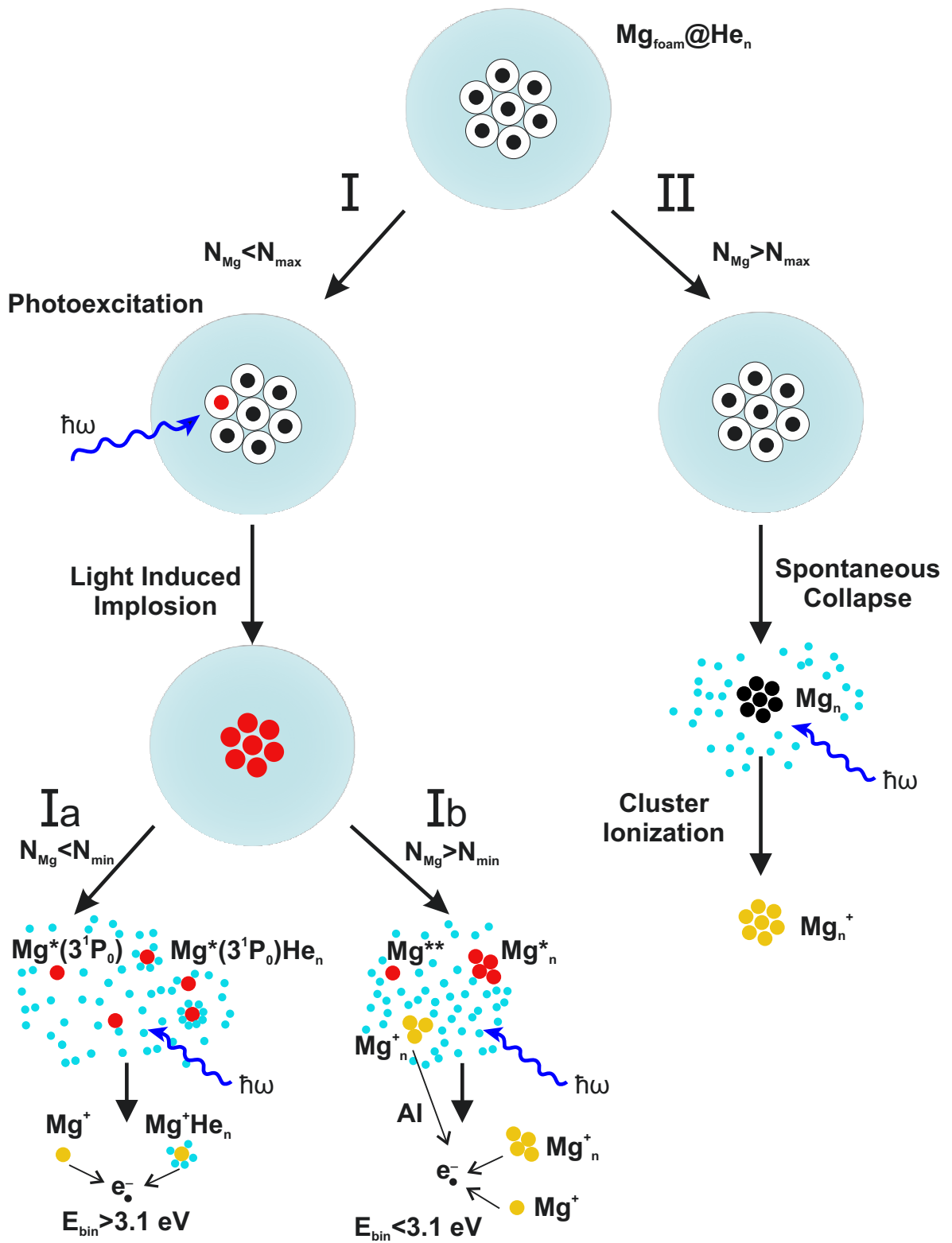
Figure 7.9: Schematic representation of the behavior of Mg foam at different initial conditions.

$N_{Mg} \geq N_{max}$. At high doping level, the foam becomes unstable. This is reflected in a spontaneous collapse, before the interaction of the foam with the laser light. The evidence for this process is found in observations of droplet depletion and the presence of Mg_n clusters observed by mass spectrometry. This will be discussed later, whereas the current section concentrates on the case (Ib).

The observation of atoms excited beyond 3^1P_1 state suggests an implosion scenario, i.e., an energy release in the range up to a few electronvolts during the collapse, which is transferred to the atom. The presence of N_{min} shows that a certain number of interacting atoms is required to induce the implosion, since the helium environment provides an energy dissipation pathway. This is supported by the observed dependence of N_{min} on the droplet size. A high amount of the energy dissipates by evaporation of He atoms. The excitation of collective surface and volume modes may also reduce the efficiency of the energy transfer to the Mg atoms. The minimal amount of energy needed to excite collective modes depends on droplet size and scale as r_{drop}^{-1} and $r_{drop}^{-3/2}$ for surface and volume modes, respectively (see Ch. 2). Thus, collective excitations are more favorable in larger droplets. The experimentally observed values of N_{min} only weakly depend on the droplet size (Fig. 7.5 and Tab. 7.2) and varies from $N_{min}=5$ for $\overline{N}_{He}=3.3 \cdot 10^3$ up to $N_{min}=12$ for $\overline{N}_{He}=1.2 \cdot 10^5$. This suggests, that only a minor fraction of the energy is transferred to the droplet.

The photoelectron yields from different excited states depend on $\overline{N}_{Mg}$, see Fig. 7.10. Photoemission from states with different E_{bin} do not appear simultaneously with respect to $\overline{N}_{Mg}$. Application of the analysis based on the pick-up statistics to Y_e allows to extract the values of N_{min}^{peak}, that is the number of atoms at which photoelectrons with certain E_{bin} appear (Fig. 7.10 (inset)). The values N_{min}^{peak} show a trend of increasing with decrease of binding energy and indicates, that above the N_{min}^{peak} threshold, additional atoms contributes and increase the amount of energy released in the implosion. Note, that a similar dependence has been observed for all droplet sizes. For most deeply bound state ($E_{bin}=2.25\,\text{eV}$), N_{min}^{peak} is equal to N_{min}.

A rough estimate of the release energy value E_r can be obtained assuming the Mg_2 binding energy in the excited state. Being initially located at a distance of $r_{foam}=10\,\text{Å}$, the two Mg atoms find themselves as a dimer in the $A^1\Sigma_u^+$ state after photoexcitation[16]. By association, a binding energy of $E_{bin}(A^1\Sigma_u^+)=1.17\,\text{eV}$ will be released. Taking this into account, a rough value of $E_r=1\,\text{eV}$ per atom can be assumed for larger foams.

---

[16] The $A^1\Sigma_u^+$ state results from a combination of initial 3^1S_0 and 3^1P_1 atomic levels, with the equilibrium distance of $3\,\text{Å}$ [197].

Figure 7.10: Electron signals from selected excited states as a function of average doping[15]. Solid lines correspond to the best fit, with respect to the pick-up statistics. (inset) The minimum number of Mg atoms, at which the photoemission from the excited states can be observed. Helium droplet size $\overline{N}_{He}=5.2\cdot10^4$.
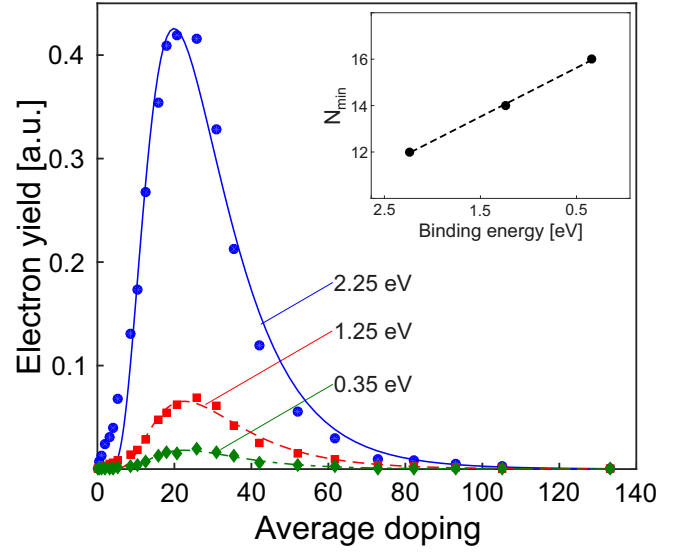
It seems to be reasonable source for atomic excitation, since, for example, the transition energy from 3^1P_1 to 4^1S_0 is $E_{tran}=1.05\,\text{eV}$. The released energy is $E_r^{tot}=E_r(N_{Mg}^{min}-1)=4\,\text{eV}$ for $N_{min}=5$ ($N_{He}=3,3\cdot10^3$) exceeds the value of E_{tran} by about $3\,\text{eV}$. Due to energy conservation, the part of the energy has to be transferred to the surrounding helium, which is sufficient to completely evaporate the droplet. In case of the larger foams, the binding energy changes with increasing N_{Mg}, and can be higher or lower than E_r. Excitation of multiple foam atoms can also takes place. Additionally, the value of E_r may strongly be enhanced when the imploding foam undergoes the nonmetal-to-metal transition [187, 269].

It is reasonable to consider the collisional excitation during the implosion. Collisions between ground state atoms at different collision energies of rare [270, 271] and mixed alkali and rare gas [272–274] atoms may lead to electronic excitations. In the present system, Mg atoms rapidly move towards each other after photoexcitation. In order to estimate the collision energies, the characteristic interatomic distance r_{Mg-Mg} and the collapse time of $\tau=350\,\text{fs}$ [189] can be taken into account. Thus, the mean speed of colliding atoms is $\overline{v}_{Mg}=2.9\cdot10^3$ m/s can be deduced, which corresponds to kinetic energy of $E_{kin}^{col}\approx1\,\text{eV}$. For N_{min} foam atoms, value of $E_{tot}^{col}=N_{min}\cdot E_{kin}^{col}$ is higher than $3.5\,\text{eV}$ even for the smallest droplets and sufficient to promote electrons to high lying states. Although the available energy is high enough to excite an atom, the efficiency is expected to be low, since the collision cross-section depends on the kinetic energy. The excitation cross-sections are low close to the transition energies and only reach

---

[16]This figure has been published in [261].

high values for several hundred electronvolts [271, 272]. In Ne-Ne and Ar-Ar collisions, the threshold energies might be even higher than the IP of corresponding atoms [270].

The enhancement of the excitation probability is found in collisions of initially excited atoms, known as energy pooling collisions (EPC) [275, 276]. In EPC, the excitation energy of an atom is transferred to another excited atom in the collision and can be described as

$$A^* + B^* \rightarrow A^{**} + B + \Delta E \tag{7.3}$$

where A* and B* are atoms in excited states, A** is the atom in the highly excited state, B - atom in the ground state and ΔE is the energy defect. Value of the ΔE represents the excess energy, as a difference of the excitation energy of A** state to the sum of the electron energies of A* and B* and determines the energy which would be transfered or taken from the kinetic energy of the colliding atoms[17]. The excitation probability for a given final state depends on the three factors: (i) The sum of the electron energies in the excited states before the collision; (ii) the temperature, i.e. E_{kin}^{gas} of the gas. When the value of ΔE is close to E_{kin}^{gas} the probability is increasing. (iii) the particle density n, since the rate of EPC scales as n^2. EPC has been discovered both experimentally and theoretically, for different targets, e.g. dense vapors alkali metals [277–282], their mixtures [283–285], alkali-earth metals and their mixtures [286–288], In [289], Hg [290] and others.

In the present system, it is possible that EPC takes place. If multiple Mg atoms are excited, the total electronic energy is high enough to excite electrons. Moreover, already for two atoms in 3^1P_1, $E_{tot}(3^1P_1)$=8.7 eV is higher than the IP of Mg. Hence all levels above 3^1P_1 can in principle be occupied as a result of an EPC. Since in the large droplets more particles are required for the excitation of highly excited states, the EPC probability will decrease. Thus it will be reflected in the lower relative intensities of photoelectron peaks for larger droplets. On the other hand, EPC has been discovered

---

[17]An illustrative example is EPC between Na atoms in $3^2P_{3/2,1/2}$ states [277]:

$Na(3^2P_{32,1/2})+Na(3^2P_{3/2,1/2}) \rightarrow Na(3^2S_{1/2})+Na(nL)+\Delta E$,
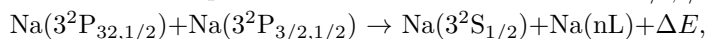
where $3^2S_{1/2}$ is the ground state configuration, and nL represents different excited states, e.g., 5S,6S,5D, etc. By comparing the energies required to populate different states with the sum of the excitation energies of initial $3^2P_{3/2,1/2}$, the values of the ΔE has been deduced. For the $5^2S_{1/2}$ state, the transition energy is lower than the total energy of electrons in $3^2P_{3/2,1/2}$ states. The corresponding value of $\Delta E_{5^2S_{1/2}}$= 88 meV is released as kinetic energy of atoms. In contrast, for $4^2D_{5/2,3/2}$ state, the transition energy is higher than E_{tot}, with $\Delta E_{4^2D_{5/2,3/2}}$=−79 eV. Hence it has to be provided by the kinetic energy of the atoms.

in binary collisions, whereas in foam collapse many atoms are involved simultaneously. For all experimentally observed highly excited states, the $\Delta E > 0$, having values in the range between 1.06 and 3.6 eV. In the collapse, the E_{kin}^{gas} can be replaced by E_{kin}^{col}. The estimation of the E_{kin}^{col} shows, that the total energy of the colliding particles is higher than ΔE. The presence of He atoms can affect EPC as well. In any case, it is anticipated, that the value of E_{kin}^{tot} will be close to $\Delta E = 3.6$ eV. This would reflect on a higher probability of excitation of deeply bound states, which has been observed in the experiment.

Together with EPC, associative ionization (AI) can take place [275, 290]. If the interaction of the two excited atoms is attractive, a dimer can be formed upon the collision. When the total electronic energy of the colliding atoms is higher then the IP of the product particle, further autoionization can occur and therefore result in the formation of ions. This reaction can be described as

$$A^* + B^* \rightarrow AB^+ + e^- \tag{7.4}$$
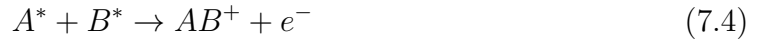
with estimated electron kinetic energy [291]

$$E_e = (E_A + E_B) - (IP_{AB} + E_{jv}) + \Delta E \tag{7.5}$$

where E_A and E_B are electronic excitation energies of colliding particles, IP$_{AB}$ is the ionization potential of the end product AB, E_{jv} is the internal energy of the ion AB$^+$ and ΔE is the energy defect. The total electronic excitation energy of two Mg atoms in 3^1P$_1$ state is already higher than the IP of a single atom. Taking into account the general decrease of IP of clusters with the cluster size, the energy is higher than the IP of Mg$_N$ cluster. Thus, energetically AI of Mg clusters in the implosion is possible. Note, that it does not exclude the potential single photon ionization of the clusters. At λ_{foam}, the direct ionization of Mg clusters in the ground state is not expected, since IP$>$E$_{ph}$. In the case of initially excited clusters, the ionization probability will depend on the lifetime of the excited state, having typical value in the range of femto- to picoseconds [8, 292]. Metastable electronically excited states have been found for other elements, but observed for specific sizes and laser wavelength [31, 32, 142], whereas all Mg$_N^+$ ions can be observed at single laser wavelength λ_{foam}. Hence, the probability that photoionization takes place at the laser conditions used in the experiment is low. On the other hand, AI only requires photoabsorption to produce initially excited atoms, and no subsequent photoabsorption is required. Both EPC and AI may provide a

rather good explanation of the features observed in the PES and the origin of Mg_n^+ in the mass spectra.

7.4 Ionization of Mg clusters formed by spontaneous collapse

Helium droplets that contain more than N_{max} magnesium atoms do not participate in the emission of HE electrons. As discussed above, this is attributed to the spontaneous collapse of Mg foam. Hence the formation of compact Mg clusters is anticipated. In order to prove it, the mass spectroscopy measurements in combination with the OPO laser system at $\lambda_{las} \leq \lambda_{foam}$ were performed. Direct ionization of clusters is expected, since the photon energies E_{ph} in this wavelength region is higher than the theoretically predicted values of the IP [268, 293–295].

Examples of corresponding mass spectra are shown in Fig. 6.9 (right) for two chosen doping conditions: $\overline{N}_{Mg}$=26 (maximum of HE-emission) and $\overline{N}_{Mg}$=67 (HE-emission significantly depleted). When the laser wavelength is adjusted to λ_{las}=254 nm, only clusters with N_{Mg} up to 26 are observed at $\overline{N}_{Mg}$=26, whereas at $\overline{N}_{Mg}$=67 sizes up to N_{Mg}=56 are clearly visible. The observed patterns show characteristic features of Mg_N mass spectra, for example, a significant drop in Mg_{22}^+ yield [187]. In addition, no signals of Mg^+He_N are observed. In contrast, spectra recorded at λ_{foam} (Fig. 6.9, left) show a different behavior. At $\overline{N}_{Mg}$=26 only clusters up to Mg_{12} are obtained, whereas no clusters are observed at $\overline{N}_{Mg}$=67. The recorded dependencies of the total ion yield Y_{tot}^{ion} (see Fig. 6.10) show strong increase at λ_{las}=254 nm, whereas the yield Y_{foam}^{ion} at the foam resonance decreases. This observation indicates, that part of the foams collapse before the photoexcitation and form compact clusters. Thus, both helium droplets with foam and free Mg_N are present in the beam. At high doping conditions, only free clusters reach the interaction region.

The presence of free Mg clusters opens an opportunity to study size-dependent properties, in particular, the ionization potential. Up to now, only theory provides an information on the IP of Mg_N [268, 293–295] and no experimental data are available. The latter is related to challenges in the production of free small Mg_N. For example, only $(MgO)_N$ clusters have been produced by the gas aggregation technique [296].

In helium droplets, the Mg_N clusters can be created at high doping conditions. Assuming that ions are only produced by the direct ionization, i.e. single-photon process, the ionization efficiency curves (see Fig. 6.11) can be used to determine the ionization potentials IP. The corresponding values can be extracted by application

of a method based on fitting the ionization efficiency curves with an error function [153, 234, 297]:

$$f(\epsilon) = \frac{1}{\pi} \int\limits_{b(E-\epsilon)}^{\inf} e^{-t^2} \, dt \qquad (7.6)$$

where b and E are fit parameters. E determines the maximum of the first derivative of $f(\epsilon)$, and the parameter b is inversely proportional to its half-width. The value of E can be assigned to the vertical ionization potential[18], when the width of the ionization threshold is only determined by electron-vibronic interaction of the neutral and ionized clusters. This method is applied to ionization efficiency curves of Mg_N in order to obtain corresponding values of ionization potentials IP_N. Examples of the fits are shown in Fig. 6.11

Extracted values of IP are shown in Fig.7.11 (black). The minimal cluster size which can be probed is limited to $N=7$, due to the highest photon energy of 5.61 eV which can be provided by the OPO laser system. For clusters with $N=5, 6$ an increase of the yields close to the 5.6 eV is observed, but the number of data points is not sufficient to extract the corresponding IP_N. Nevertheless, it indicates that clusters with sizes $N \leq 6$ have IP$\geq$5.6 eV. The values of IP_N for N in range $7 \leq N \leq 56$ decrease with increasing of N, and can be divided into two regions. (i) Between $N=7$ and $N = 18$ the IP drops from $IP_7=5.38$ eV down to $IP_{18}=5.00$ eV. (ii) Starting from $N=18$ the IP decreases gradually down to $IP_{56}=4.87$ eV. Additionally, some oscillations of the IP are observed. For sizes N=10, 13, 16, 17 the relative increase of IP is rather high, whereas for N=20, 22, 25, 28, 29, 34, 38, 44, 46 the IP increase only slightly.

The IP_N with N$\leq$22 agree fairly well with theory[19] [268, 293, 294], except that the oscillations of the IP are poorly reproduced. The experimental data show no evidence of the increase of IP_7, IP_9, IP_{11} predicted by Jellinek *et al.* and Lyalin *et al.* [268, 294], see Fig. 7.11 red and green, respectively. Moreover, the strong increase of IP_{10} is opposite to the calculations. Note, that no enhancement of IP_7, IP_9, IP_{11} has been found in

---

[18]By vertical ionization potential means a vertical transition from the electronic state of a neutral particle to the electronic state of ion in which the atomic configuration does not change. In contrast, the adiabatic ionization potential is the energy difference between the ground states of neutral and ionized particles. Since the atomic configuration of the ion can strongly deviate from neutral, direct experimental observation of AIP is challenging [195]. In following, the IP means the vertical ionization potential.

[19]Here the data from Janecek *et al* [295] are omitted, since only the adiabatic ionization potentials are calculated in that work.
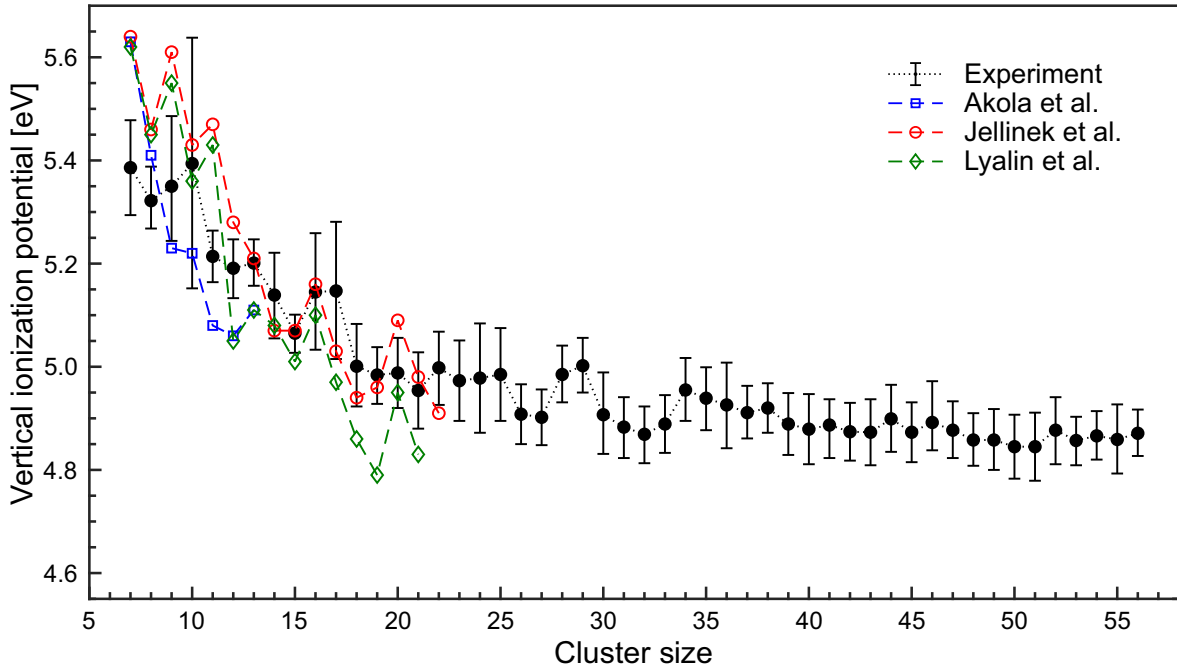
Figure 7.11: Ionizaion potentials IP$_N$ in the size range N=7-56 (black). Dashed color lines correspond to theoretical calculations, from works of Akola *et al.* (blue) [293], Jellinek *et al.* (red) [268] and Lyalin *et al.* (green) [294].

the work of Akola *et al.* [293]. Such an oscillatory behavior of IP$_N$ was assigned to the interplay between electronic and geometrical effects [294], meaning that the cluster geometry could play a significant role. For example, the calculated lowest energy geometries of Mg$_N$ by Akola *et al.* [293] differ from the work in [268,294], resulting in a difference of calculated IP$_7$, IP$_9$, IP$_{11}$. In the experiment, the clusters are formed by a spontaneous collapse of the foam. One can expect a high energy release even without photoexcitation. Therefore, the structures of the clusters might be different compared to their lowest energy geometries. Different isomers of clusters of the same size may give a contribution to the ion signal, as well. Nevertheless, the similarities between theory and experiment can be observed for IP$_{13}$, IP$_{16}$ and IP$_{20}$. For the latter size, the experimentally observed increase is significantly lower than predicted by calculations.

The maxima in IP can be attributed to the electronic shell closings of Mg$_N$ at certain sizes. According to the jellium model, the closing of the electronic shells is expected for clusters having N$_e$= 8, 18, 20, 34, 40, 58, 68, 90, 92, 106, etc. electrons (see Ch. 4). Since the Mg atoms have two valence electrons, the corresponding clusters sizes are N= 4, 9, 10, 17, 20, 29, 34, 45, 46, 53. Indeed, values of IP$_{10}$, IP$_{17}$, IP$_{20}$, IP$_{29}$, IP$_{34}$ and
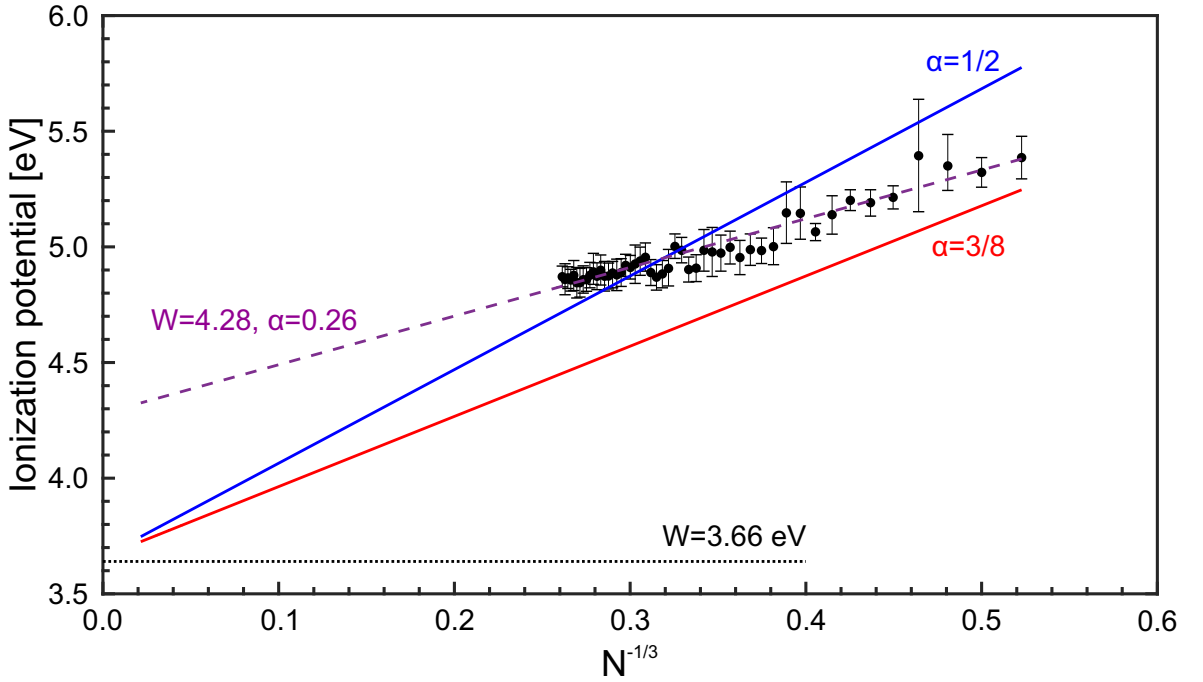
Figure 7.12: IP_N of Mg in comparison to the CSM. Black dots correspond to experimental data, plotted as a function of $N^{-1/3}$. Solid lines represent an size dependence of IP calculated by Eq. 4.3, with $\alpha=1/2$ and $\alpha=3/8$. Magenta dashed line corresponds to the fit based on Eq. 4.3. Black dotted line shows a bulk work function of Mg.

IP_{46} are slightly higher than for neighboring clusters. Hence, this can be assigned to the increase of the IP of closed shells clusters. The origin of other peaks can be related to the shell closure in non-spherical clusters, resulting in the enhancement of the IP[20].

Magnesium clusters are known to exhibit a nonmetal-to-metal transition with increasing size, which takes place around $N=18$-20 [187, 269]. However, the situation is not as simple when compared to other clusters, e.g. Hg_N [244]. According to photo-electron spectroscopy on Mg_N^- anions the metallic behavior might set in for a certain size, then be lost and reoccur for larger N. Moreover, the charge of the cluster could play an important role [298]. The metallic properties might manifest themselves in an agreement of the IP_N with the CSM. Figure 7.12 shows a comparison of the experimental data with ionization potentials of CSM model IP_{CSM}. Note, that the IP_N now are plotted as a function of $N^{-1/3}$, since it is proportional to the cluster radius,

---

[20]For example, an additional magic number of sodium clusters with $N_e=26$ correspond to a shell closing in deformed Na_{26}. The IP of Mg_{13} shows a slightly enhanced value in comparison to the neighbor sizes and hence, may indicate a similar situation

as $R_{cl}=r_{ws} \cdot N^{-1/3}$. The Wigner-Seitz radius of magnesium is r_{ws}=1.776 Å [299, 300]. The IP_{CSM} are calculated by Eq. 4.3 for two boundary values of α, e.g. α=1/2 (blue) and α=3/8 (red). The bulk work function is reported to be W_{Mg}=3.66 eV [301] (black dotted line). Obviously, the function that corresponds to α=3/8 is in complete disagreement with the experiment. For α=1/2, the situation appears to slightly better, but the CSM function crosses data points only in the range N=28-34. The variation of parameter α in between 1/2 and 3/8 does not improve the overall agreement. It has to be noted, that for α=0.465, IP$_{CMS}$ passes data points which correspond to the magic numbers, e.g. IP$_{10}$, IP$_{17}$ and IP$_{20}$, but the agreement with the complete data set is not observed. Application of Eq. 4.5 does not provide a better agreement as well. Moreover, considering an electron spill-out does not improve the situation.

The application of the fit procedure of the function given by Eq. 4.3 with free parameters W and α, provides a better agreement with the experiment. The best fit, corresponding to α=0.26 and W=4.28 eV is shown in Fig. 7.12, magenta dashed line. The value of α is lower than the limit of 3/8 in CSM. Such behavior has been found for other systems, indicating a strong dependence of α on the electron density [203, 240, 302]. Therefore, a deviation of α from classical values can be expected. However, the obtained value of the bulk work function W is questionable, since it is larger by 0.62 eV when compared to W_{Mg}. Similar situations have been observed for clusters of transition metals [235, 236, 303], where the agreement between CSM and experiment has been obtained assuming that W has a value different from the bulk. This has been interpreted as a difference in the cluster structure compared to the bulk material. Thus, the authors conclude that the bulk work function not necessarily is the right value for the CSM model. For Mg clusters, evidence of icosahedral geometry has been found in the size range 147≤N≤2869 [211], whereas a bulk magnesium has a hcp[21] structure [304]. One can expect, that clusters with N<147 may have an icosahedral structure as well and, hence, the shift of the IP can have a similar reason as for clusters of transition metals.

Another way to obtain relevant parameters for the CSM model is the comparison with the electron affinities, since IP and EA are related to each other (see Ch. 4). The experiments on the EA of Mg$_N^-$ were provided in [269, 305]. In the work of Thomas *et al.* [269] the EA have been measured for 3≤ N ≤35, whereas in the work of Kostko [305] the size range 3≤ N ≤95 has been studied. Both results are in good agreement with each other for sizes below N=35. Therefore, the data from [305] is used, since
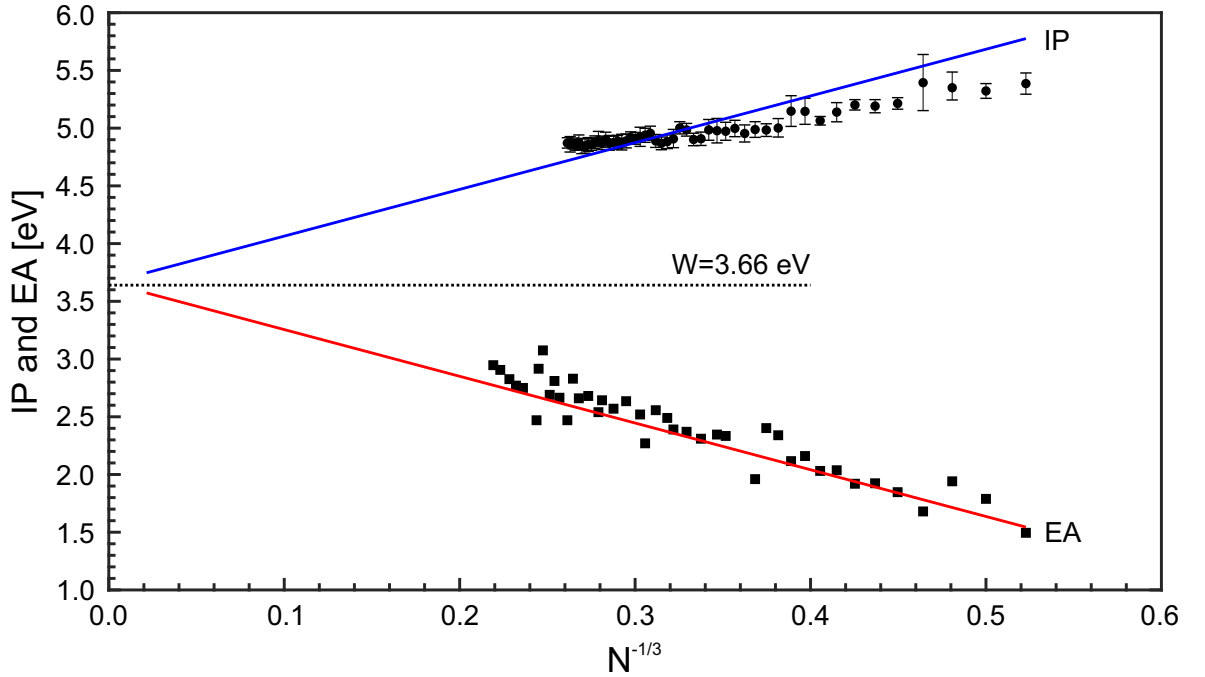
---

[21]Hexagonal close-packed

Figure 7.13: IP (black circles) and EA (black squares) of Mg_N as a function of $N^{-1/3}$. Lines corresponds to the CSM based on Eqs. 4.3 and 4.4, see text for details. The black dotted line shows the bulk work function of Mg. The EA data are taken from [305].

a larger size range is covered. Fig. 7.13 shows IP and EA as a function of $N^{-1/3}$, together with the CSM calculation by Eqs. 4.3 and 4.4, for α=0.5. The values of EA follow the CSM prediction well, indicating that negatively charged Mg_N^- exhibit metallic properties. In contrast, the IP of neutral Mg_N do not show such a clear trend. The similar situation has been observed in studies of size dependence of IP of Hg_N clusters [243]. Large deviations of the IP from CSM has been observed for $N \leq 70$ and was assigned to a not complete development of the metallicity in Hg_N. In addition, the photoelectron spectroscopy of Hg_N^- anions shows that metal-non-metal transition takes place for N=400. Mercury is a divalent element as magnesium and, therefore, a similar situation for Mg_N might be expected. Hence, the possible origin of the difference between experimental data and CSM could be assigned to a not complete development of metallic properties of Mg_N with $N \leq 56$.

Up to now, it has been assumed, that the shapes of the ionization efficiency curves only defined by the electronic-vibronic interaction of the neutral and ionized clusters. From a critical point of view, it is reasonable to assume that other processes can contribute to the ionization process. It is possible, that the plasmonic excitations may

give an impact on ionization efficiency. Indeed, when the plasmon energy has a value in the vicinity of the ionization threshold, the recorded ionization efficiency curves would be affected. Hence, the extracted values of the IP could be artificially lower or higher than the real one. Up to now no comprehensive experimental results on Mg_N plasmon energies are available. Density functional theory calculations of plasmon resonance energies of Mg_N are published, giving values in the range of 4.0-5.5 eV for N≤11 [196]. From RPA/LDA calculations the plasmon energies are obtained in the range 5.0-5.5 eV for cluster sizes N=10-56 [306]. In addition, work [196] predicts a strong absorption of small clusters at photon energies below 4.5 . Although no clear verification has been observed, a possible influence of the plasmon absorption on the ionization is conceivable. A plasmon peak around 5 eV might lead to an enhancement of the ionization cross-section in that energy range. Correspondingly, the IP_N extracted from ionization efficiency curves would exhibit lower boundaries. However, one can expect, that this effect will not be present, when the IP are away from the plasmon energy range, i.e. for large N.

The knowledge about IP_N with N>56 can provide more information on the metallic behavior of Mg_N. In the present work, the formation of larger clusters is limited by the droplet size, since it defines the critical number of atoms after which the spontaneous collapse occurs. Strong doping of droplets with $\overline{N}_{He}$>1.2·10^5, will lead to larger clusters. Although the cluster size is limited to N=56, the first experimental data on IP of Mg clusters are obtained in the frame of the present work.

8 Conclusion and outlook

In present work, the properties of magnesium ensembles in helium nanodroplets have been investigated. A combination of resonant two-photon ionization with photoelectron spectroscopy allows to probe the development of the photoexcited Mg foam on the nanosecond time scale. The main achievements are summarized as follows:

- Photoelectron spectra after the R2PI of the droplets containing a single Mg atom show a single peak. The corresponding binding energy is shifted with respect to a free atom. This feature is assigned to a reducing of the atomic ionization potential. The value of the shift indicates complete solvation of the Mg atom, even in the excited state. Together with the data on the optical absorption it confirms an interior location of Mg atoms in the droplet.

- When droplets are doped with several atoms, the photoelectron signals from highly excited states have been observed. The characteristic spectral pattern is identical for a wide range of doping conditions and droplet sizes. The appearance of highly excited atoms is assigned to implosion scenario, i.e. a fast collapse of excited foam which is accompanied by energy release in the range of one electronvolt per atom. Transfer of the excess energy leads to a population of highly excited states which are probed by the ionizing photon.

- Analysis of the doping dependence of the high energy electron emission with respect to the pick-up statistics reveals the foam size ranges within which the features can be observed. The minimal foam size is assigned to the lowest number of atoms required for efficient energy transfer. The weak dependence of this value on droplet size indicates that the process is rather efficient. The maximum number of atoms defines the largest foam size which can be stabilized in the droplet. In contrast to the minimal foam size, the stability limit strongly depends on the size of the droplet. Doping the droplets with a number of atoms beyond the stability limit leads to a spontaneous collapse of the foam before they reach the interaction region.

- Mass spectrometry studies on droplets doped higher than stability limit reveal a formation of free Mg_N clusters. Ionization potentials of Mg_N clusters have been measured by analysis of the ionization efficiency curves. The dependence of the ionization potential on cluster size shows a deviation from the prediction based on the charged sphere model. Possibly, either the metallicity of Mg_N is not developed for N≤56 or there is a contribution of the plasmon excitation on cluster ionization.

The results of studies on the optically induced implosion do not provide any time-resolved information, since the excitation and ionization take place on the timescale of the nanosecond laser pulse. Moreover, it is expected that the time required for the collapse is shorter than a nanosecond. The combination of the photoelectron spectroscopy with femtosecond pump-probe technique at the resonant wavelength can be used to map the dynamics of the collapse process. Thus, it allows to study collisions between low energy atoms under well-defined conditions.

Based on the obtained data, it is challenging to assign a dominant process which leads to the atomic excitation. More information can be revealed by a measurement of the kinetic energy of fragment ions. One can expect, that the contribution of energy pooling collisions will be reflected in specific features in the ion kinetic energy spectra. For example, this can be achieved by using velocity map imaging technique. Coincidence spectroscopy may also be used to reveal the origin of the photoelectron features, e.g., photoemission in the range $1.2\,\text{eV} \leq E_{kin} \leq 1.9\,\text{eV}$ and features observed at specific excitation wavelengths. In addition, this technique will allow to resolve the processes leading to cluster ionization, that is associative ionization or single photon ionization of excited clusters.

Evidence of the impact of the doping process on the foam stability has been observed. Due to the low binding energy of the Mg atoms, the sensitivity of the foam to small perturbations is expected. Hence, the foam may serve as a probe for experimental studies with respect to collisions between foreign particles and droplets.

The formation of free Mg_N clusters at high doping conditions opens the opportunities to study their size-dependent properties. For example, extending the present studies on the IP to larger cluster sizes will provide additional information on the onset of metallicity in Mg clusters, since an agreement with the conducting sphere model for metallic clusters is expected. In addition, the optical properties, e.g., an absorption or plasmonic excitation, may be studied as well.

Bibliography

[1] E. Whittle, D. A. Dows, and G. C. Pimentel. Matrix isolation method for the experimental study of unstable species. *J. Chem. Phys.*, 22(11):1943–1943, 1954.

[2] A. J. Barnes, W. J. Orville-Thomas, A. Müller, and R. Gaufrès, editors. *Matrix Isolation Spectroscopy*. Springer, Dordrecht, 1981.

[3] R. E. Smalley, B. L. Ramakrishna, D. H. Levy, and L. Wharton. Laser spectroscopy of supersonic molecular beams: Application to the NO_2 spectrum. *J. Chem. Phys.*, 61(10):4363–4364, 1974.

[4] R. E. Smalley, L. Wharton, and D. H. Levy. Molecular optical spectroscopy with supersonic beams and jets. *Acc. Chem. Res.*, 10(4):139–145, 1977.

[5] J. M. Hayes. Analytical spectroscopy in supersonic expansions. *Chem. Rev.*, 87(4):745–760, 1987.

[6] J. P. Toennies and A. F. Vilesov. Superfluid helium droplets: a uniquely cold nanomatrix for molecules and molecular complexes. *Angew. Chem. Int. Ed.*, 43(20):2622–2648, 2004.

[7] F. Stienkemeier and K. K. Lehmann. Spectroscopy and dynamics in helium nanodroplets. *J. Phys. B: At., Mol. Opt. Phys.*, 39(8):R127, 2006.

[8] J. Tiggesbäumker and F. Stienkemeier. Formation and properties of metal clusters isolated in helium droplets. *Phys. Chem. Chem. Phys.*, 9(34):4748–4770, 2007.

[9] A. Scheidemann, J. P. Toennies, and J. A. Northby. Capture of neon atoms by ^{4}He clusters. *Phys. Rev. Lett.*, 64(16):1899, 1990.

[10] B. E. Callicoatt, K. Förde, T. Ruchti, L. Jung, K. C. Janda, and N. Halberstadt. Capture and ionization of argon within liquid helium droplets. *J. Chem. Phys.*, 108(22):9371–9382, 1998.

[11] F. Stienkemeier, J. Higgins, W. Ernst, and G. Scoles. Laser spectroscopy of alkali-doped helium clusters. *Phys. Rev. Lett.*, 74:3592–3595, 1995.

[12] J. H. Reho, U. Merker, M. R. Radcliff, K. K. Lehmann, and G. Scoles. Spectroscopy and dynamics of Al atoms solvated in superfluid helium nanodroplets. *J. Phys. Chem. A*, 104(16):3620–3626, 2000.

[13] K. Nauta and R. E. Miller. Metastable vibrationally excited HF (v=1) in helium nanodroplets. *J. Chem. Phys.*, 113(21):9466–9469, 2000.

[14] K. von Haeften, A. Metzelthin, S. Rudolph, V. Staemmler, and M. Havenith. High-resolution spectroscopy of NO in helium droplets: A prototype for open shell molecular interactions in a quantum solvent. *Phys. Rev. Lett.*, 95:215301, Nov 2005.

[15] K. Nauta and R. Miller. The vibrational and rotational dynamics of acetylene solvated in superfluid helium nanodroplets. *J. Chem. Phys.*, 115(18):8384–8392, 2001.

[16] z. Birer, P. Moreschini, K. K. Lehmann, and G. Scoles. Electronic spectroscopy of biphenylene inside helium nanodroplets. *J. Phys. Chem. A*, 111(31):7624–7630, 2007. PMID: 17580829.

[17] M. Y. Choi and R. E. Miller. Four tautomers of isolated guanine from infrared laser spectroscopy in helium nanodroplets. *J. Am. Chem. Soc.*, 128(22):7320–7328, 2006. PMID: 16734487.

[18] M. Y. Choi and R. E. Miller. Infrared laser spectroscopy of uracil and thymine in helium nanodroplets: vibrational transition moment angle study. *J. Phys. Chem. A*, 111(13):2475–2479, 2007. PMID: 17388352.

[19] A. Lindinger, J. P. Toennies, and A. F. Vilesov. High resolution vibronic spectra of the amino acids tryptophan and tyrosine in 0.38 K cold helium droplets. *J. Chem. Phys.*, 110(3):1429–1436, 1999.

[20] S. Denifl, I. Mähr, F. Ferreira da Silva, F. Zappa, T. D. Märk, and P. Scheier. Electron impact ionization studies with the amino acid valine in the gas phase and (hydrated) in helium droplets. *Eur. Phys. J. D*, 51(1):73–79, Jan 2009.

[21] F. Bierau, P. Kupser, G. Meijer, and G. von Helden. Catching proteins in liquid helium droplets. *Phys. Rev. Lett.*, 105:133402, Sep 2010.

[22] M. Alghamdi, J. Zhang, A. Oswalt, J. J. Porter, R. A. Mehl, and W. Kong. Doping of green fluorescent protein into superfluid helium droplets: Size and velocity of doped droplets. *J. Phys. Chem. A*, 121(36):6671–6678, 2017.

[23] M. Hartmann, R. E. Miller, J. P. Toennies, and A. F. Vilesov. Rotationally resolved spectroscopy of SF_6 in liquid helium clusters: A molecular probe of cluster temperature. *Phys. Rev. Lett.*, 75:1566–1569, Aug 1995.

[24] F. Stienkemeier, J. Higgins, C. Callegari, S. I. Kanorsky, W. E. Ernst, and G. Scoles. Spectroscopy of alkali atoms (Li, Na, K) attached to large helium clusters. *Z. Phys. D*, 38(3):253–263, 1996.

[25] F. Federmann, K. Hoffmann, N. Quaas, and J. D. Close. Rydberg states of silver: excitation dynamics of doped helium droplets. *Phys. Rev. Lett.*, 83(13):2548, 1999.

[26] O. Bünermann, M. Mudrich, M. Weidemüller, and F. Stienkemeier. Spectroscopy of Cs attached to helium nanodroplets. *J. Chem. Phys.*, 121(18):8880–8886, 2004.

[27] M. Koch, A. Kautsch, F. Lackner, and W. E. Ernst. One- and two-color resonant photoionization spectroscopy of chromium-doped helium nanodroplets. *J. Phys. Chem. A*, 118(37):8373–8379, 2014. PMID: 24708058.

[28] M. Hartmann, R. E. Miller, J. P. Toennies, and A. F. Vilesov. High-resolution molecular spectroscopy of van der Waals clusters in liquid helium droplets. *Science*, 272(5268):1631–1634, 1996.

[29] S. Grebenev, J. P. Toennies, and A. F. Vilesov. Superfluidity within a small helium-4 cluster: The microscopic andronikashvili experiment. *Science*, 279(5359):2083–2086, 1998.

[30] M. Hartmann, N. Pörtner, B. Sartakov, J. P. Toennies, and A. F. Vilesov. High resolution infrared spectroscopy of single SF_6 molecules in helium droplets. i. Size effects in ^{4}He droplets. *J. Chem. Phys.*, 110(11):5109–5123, 1999.

[31] F. Federmann, K. Hoffmann, N. Quaas, and J. P. Toennies. Spectroscopy of extremely cold silver clusters in helium droplets. *Eur. Phys. J. D*, 9(1):11–14, Dec 1999.

[32] P. Radcliffe, A. Przystawik, T. Diederich, T. Döppner, J. Tiggesbäumker, and K.-H. Meiwes-Broer. Excited-state relaxation of Ag_8 clusters embedded in helium droplets. *Phys. Rev. Lett.*, 92(17):173403, 2004.

[33] E. Loginov, L. F. Gomez, N. Chiang, A. Halder, N. Guggemos, V. V. Kresin, and A. F. Vilesov. Photoabsorption of Ag_N (N$\sim$ 6–6000) nanoclusters formed in helium droplets: Transition from compact to multicenter aggregation. *Phys. Rev. Lett.*, 106(23):233401, 2011.

[34] E. Lugovoj, J. P. Toennies, and A. F. Vilesov. Manipulating and enhancing chemical reactions in helium droplets. *J. Chem. Phys.*, 112(19):8217–8220, 2000.

[35] S. A. Krasnokutski and F. Huisken. Ultra-low-temperature reactions of Mg atoms with O_2 molecules in helium droplets. *J. Phys. Chem. A*, 114(27):7292–7300, 2010.

[36] C. P. Moradi, A. M. Morrison, S. J. Klippenstein, C. F. Goldsmith, and G. E. Douberly. Propargyl + O_2 reaction in helium droplets: Entrance channel barrier or not? *J. Phys. Chem. A*, 117(50):13626–13635, 2013. PMID: 24015722.

[37] J. Zhang, Y. He, W. M. Freund, and W. Kong. Electron diffraction of superfluid helium droplets. *J. Phys. Chem. Lett.*, 5(11):1801–1805, 2014. PMID: 24920997.

[38] Y. He, J. Zhang, L. Lei, and W. Kong. Self-assembly of iodine in superfluid helium droplets: Halogen bonds and nanocrystals. *Angew. Chem. Int. Ed.*, 56:3541–3545, 2017.

[39] J. Zhang, Y. He, L. Lei, M. Alghamdi, and W. K. Andrew Oswalt. Serial single molecule electron diffraction imaging: diffraction background of superfluid helium droplets. *Proc. SPIE*, 10380:10380 – 10380 – 10, 2017.

[40] S. R. Krishnan, C. Peltz, L. Fechner, V. Sharma, M. Kremer, B. Fischer, N. Camus, T. Pfeifer, J. Jha, M. Krishnamurthy, C.-D. Schröter, J. Ullrich, F. Stienkemeier, R. Moshammer, T. Fennel, and M. Mudrich. Evolution of dopant-induced helium nanoplasmas. *New J. Phys.*, 14(7):075016, 2012.

[41] A. Heidenreich, B. Grüner, M. Rometsch, S. R. Krishnan, F. Stienkemeier, and M. Mudrich. Efficiency of dopant-induced ignition of helium nanoplasmas. *New J. Phys.*, 18(7):073046, 2016.

[42] A. C. LaForge, M. Drabbels, N. B. Brauer, M. Coreno, M. Devetta, M. Di Fraia, P. Finetti, C. Grazioli, R. Katzy, V. Lyamayev, et al. Collective autoionization in multiply-excited systems: a novel ionization process observed in helium nanodroplets. *Sci. Rep.*, 4:3621, 2014.

[43] M. Shcherbinin, A. C. LaForge, V. Sharma, M. Devetta, R. Richter, R. Moshammer, T. Pfeifer, and M. Mudrich. Interatomic coulombic decay in helium nanodroplets. *Phys. Rev. A*, 96(1):013407, 2017.

[44] L. F. Gomez, K. R. Ferguson, J. P. Cryan, C. Bacellar, R. M. P. Tanyag, C. Jones, S. Schorb, D. Anielski, A. Belkacem, C. Bernando, et al. Shapes and vorticities of superfluid helium nanodroplets. *Science*, 345(6199):906–909, 2014.

[45] O. Gessner and A. F. Vilesov. Imaging quantum vortices in superfluid helium droplets. *Annu. Rev. Phys. Chem.*, 70(1):173–198, 2019. PMID: 31174460.

[46] K. Nauta and R. E. Miller. Nonequilibrium self-assembly of long chains of polar molecules in superfluid helium. *Science*, 283(5409):1895–1897, 1999.

[47] K. Nauta and R. E. Miller. Formation of cyclic water hexamer in liquid helium: The smallest piece of ice. *Science*, 287(5451):293–295, 2000.

[48] C. P. Schulz, P. Claas, D. Schumacher, and F. Stienkemeier. Formation and stability of high-spin alkali clusters. *Phys. Rev. Lett.*, 92:013401, Jan 2004.

[49] F. Lackner and W. E. Ernst. Photoinduced molecule formation of spatially separated atoms on helium nanodroplets. *J. Phys. Chem. Lett.*, 0(0):3561–3566, 2018.

[50] J. Eloranta. Theoretical study of quantum gel formation in superfluid ^{4}He. *J. Low Temp. Phys.*, 162(5):718–723, 2011.

[51] A. Przystawik, S. Göde, T. Döppner, J. Tiggesbäumker, and K.-H. Meiwes-Broer. Light-induced collapse of metastable magnesium complexes formed in helium nanodroplets. *Phys. Rev. A*, 78:021202, Aug 2008.

[52] H. Buchenau, E. Knuth, J. Northby, J. Toennies, and C. Winkler. Mass spectra and time-of-flight distributions of helium cluster beams. *J. Chem. Phys.*, 92(11):6875–6889, 1990.

[53] J. Harms, J. P. Toennies, and E. L. Knuth. Droplets formed in helium free-jet expansions from states near the critical point. *J. Chem. Phys.*, 106(8):3348–3357, 1997.

[54] R. E. Grisenti and J. P. Toennies. Cryogenic microjet source for orthotropic beams of ultralarge superfluid helium droplets. *Phys. Rev. Lett.*, 90:234501, Jun 2003.

[55] R. Irsig, M. Shihab, L. Kazak, T. Bornath, J. Tiggesbäumker, R. Redmer, and K.-H. Meiwes-Broer. The interaction of intense femtosecond laser pulses with argon microdroplets studied near the soft x-ray emission threshold. *J. Phys. B: At., Mol. Opt. Phys.*, 51(2):024006, 2018.

[56] R. A. C. Fraga, A. Kalinin, M. Kühnel, D. C. Hochhaus, A. Schottelius, J. Polz, M. C. Kaluza, P. Neumayer, and R. E. Grisenti. Compact cryogenic source of periodic hydrogen and argon droplet beams for relativistic laser-plasma generation. *Rev. Sci. Instrum.*, 83(2):025102, 2012.

[57] J. B. Kim, C. Schoenwaelder, and S. H. Glenzer. Development and characterization of liquid argon and methane microjets for high-rep-rate laser-plasma experiments. *Rev. Sci. Instrum.*, 89(10):10K105, 2018.

[58] M. Gauthier, C. B. Curry, S. Göde, F.-E. Brack, J. B. Kim, M. J. MacDonald, J. Metzkes, L. Obst, M. Rehwald, C. Rödel, H.-P. Schlenvoigt, W. Schumaker, U. Schramm, K. Zeil, and S. H. Glenzer. High repetition rate, multi-mev proton source from cryogenic hydrogen jets. *Appl. Phys. Lett.*, 111(11):114102, 2017.

[59] M. Lewerenz, B. Schilling, and J. P. Toennies. A new scattering deflection method for determining and selecting the sizes of large liquid clusters of ^{4}He. *Chem. Phys. Lett.*, 206(1):381 – 387, 1993.

[60] J. Harms, J. P. Toennies, and F. Dalfovo. Density of superfluid helium droplets. *Phys. Rev. B*, 58(6):3341, 1998.

[61] E. L. Knuth and U. Henne. Average size and size distribution of large droplets produced in a free-jet expansion of a liquid. *J. Chem. Phys.*, 110(5):2664–2668, 1999.

[62] L. F. Gomez, E. Loginov, R. Sliter, and A. F. Vilesov. Sizes of large He droplets. *J. Chem. Phys.*, 135(15):154201, 2011.

[63] M. Lewerenz, B. Schilling, and J. Toennies. Successive capture and coagulation of atoms and molecules to small clusters in large liquid helium clusters. *J. Chem. Phys.*, 102(20):8191–8207, 1995.

[64] B. Schilling. *Molekularstrahlexperimente mit Helium–Clustern.* PhD thesis, Max–Planck–Institut für Strömungsforschung, Göttingen, 1993.

[65] T. Jiang and J. A. Northby. Fragmentation clusters formed in supercritical expansions of ^{4}He. *Phys. Rev. Lett.*, 68:2620–2623, Apr 1992.

[66] U. Henne and J. P. Toennies. Electron capture by large helium droplets. *J. Chem. Phys.*, 108(22):9327–9338, 1998.

[67] D. M. Brink and S. Stringari. Density of states and evaporation rate of helium clusters. *Z. Phys. D*, 15(3):257–263, Sep 1990.

[68] M. Casas and S. Stringari. Elementary excitations of ^{4}He clusters. *J. Low Temp. Phys.*, 79(3):135–149, May 1990.

[69] J. P. Toennies and A. F. Vilesov. Novel low-energy vibrational states of foreign particles in fluid ^{4}He clusters. *Chem. Phys. Lett.*, 235(5):596 – 603, 1995.

[70] J. A. Northby. Experimental studies of helium droplets. *J. Chem. Phys.*, 115(22):10065–10077, 2001.

[71] K. T. Tang, J. P. Toennies, and C. L. Yiu. Accurate analytical He-He van der Waals potential based on perturbation theory. *Phys. Rev. Lett.*, 74:1546–1549, Feb 1995.

[72] R. E. Grisenti, W. Schöllkopf, J. P. Toennies, G. C. Hegerfeldt, T. Köhler, and M. Stoll. Determination of the bond length and binding energy of the helium dimer by diffraction from a transmission grating. *Phys. Rev. Lett.*, 85:2284–2287, Sep 2000.

[73] S. A. Chin and E. Krotscheck. Systematics of pure and doped ^{4}He clusters. *Phys. Rev. B*, 52:10405–10428, Oct 1995.

[74] C. Bernando, R. M. P. Tanyag, C. Jones, C. Bacellar, M. Bucher, K. R. Ferguson, D. Rupp, M. P. Ziemkiewicz, L. F. Gomez, A. S. Chatterley, T. Gorkhover, M. Müller, J. Bozek, S. Carron, J. Kwok, S. L. Butler, T. Möller, C. Bostedt, O. Gessner, and A. F. Vilesov. Shapes of rotating superfluid helium nanodroplets. *Phys. Rev. B*, 95:064510, Feb 2017.

[75] D. Rupp, N. Monserud, B. Langbehn, M. Sauppe, J. Zimmermann, Y. Ovcharenko, T. Möller, F. Frassetto, L. Poletto, A. Trabattoni, et al. Coherent diffractive imaging of single helium nanodroplets with a high harmonic generation source. *Nat. Commun.*, 8(1):493, 2017.

[76] L. F. Gomez, E. Loginov, and A. F. Vilesov. Traces of vortices in superfluid helium droplets. *Phys. Rev. Lett.*, 108:155302, Apr 2012.

[77] M. Iino, M. Suzuki, and A. J. Ikushima. Surface tension of liquid ^{4}He. Surface energy of the Bose-Einstein condensate. *J. .Low Temp. Phys.*, 61(1):155–169, Oct 1985.

[78] M. Barranco, R. Guardiola, S. Hernández, R. Mayol, J. Navarro, and M. Pi. Helium nanodroplets: An overview. *J. Low Temp. Phys.*, 142(1-2):1, 2006.

[79] M. Hartmann, F. Mielke, J. Toennies, A. Vilesov, and G. Benedek. Direct spectroscopic observation of elementary excitations in superfluid He droplets. *Phys. Rev. Lett.*, 76(24):4560, 1996.

[80] L. A. Surin, A. V. Potapov, B. S. Dumesh, S. Schlemmer, Y. Xu, P. L. Raston, and W. Jäger. Rotational study of carbon monoxide solvated with helium atoms. *Phys. Rev. Lett.*, 101:233401, Dec 2008.

[81] J. D. Close, F. Federmann, K. Hoffmann, and N. Quaas. Helium droplets: A nanoscale cryostat for high resolution spectroscopy and studies of quantized vorticity. *J. Low Temp. Phys.*, 111(3):661–676, May 1998.

[82] F. Ancilotto, M. Barranco, and M. Pi. Probing vortices in ^{4}He nanodroplets. *Phys. Rev. Lett.*, 91:105302, Sep 2003.

[83] K. K. Lehmann and R. Schmied. Energetics and possible formation and decay mechanisms of vortices in helium nanodroplets. *Phys. Rev. B*, 68:224520, Dec 2003.

[84] R. M. P. Tanyag, C. Bernando, C. F. Jones, C. Bacellar, K. R. Ferguson, D. Anielski, R. Boll, S. Carron, J. P. Cryan, L. Englert, S. W. Epp, B. Erk, L. Foucar, L. F. Gomez, R. Hartmann, D. M. Neumark, D. Rolles, B. Rudek, A. Rudenko, K. R. Siefermann, J. Ullrich, F. Weise, C. Bostedt, O. Gessner, and A. F. Vilesov. Communication: X-ray coherent diffractive imaging by immersion in nanodroplets. *Struct. Dyn.*, 2(5):051102, 2015.

[85] C. F. Jones, C. Bernando, R. M. P. Tanyag, C. Bacellar, K. R. Ferguson, L. F. Gomez, D. Anielski, A. Belkacem, R. Boll, J. Bozek, et al. Coupled motion of Xe clusters and quantum vortices in He nanodroplets. *Phys. Rev. B*, 93(18):180510, 2016.

[86] F. Ancilotto, M. Pi, and M. Barranco. Vortex arrays in nanoscopic superfluid helium droplets. *Phys. Rev. B*, 91(10):100503, 2015.

[87] F. Ancilotto, M. Barranco, and M. Pi. Spinning superfluid ^{4}He nanodroplets. *Phys. Rev. B*, 97:184515, May 2018.

[88] F. Coppens, F. Ancilotto, M. Barranco, N. Halberstadt, and M. Pi. Capture of Xe and Ar atoms by quantized vortices in ^{4}He nanodroplets. *Phys. Chem. Chem. Phys.*, 19(36):24805–24818, 2017.

[89] C. Bernando and A. F. Vilesov. Kinematics of the doped quantum vortices in superfluid helium droplets. *J. Low Temp. Phys.*, 191(3):242–256, May 2018.

[90] D. Spence, E. Latimer, C. Feng, A. Boatwright, A. M. Ellis, and S. Yang. Vortex-induced aggregation in superfluid helium droplets. *Phys. Chem. Chem. Phys.*, 16(15):6903–6906, 2014.

[91] P. Thaler, A. Volk, F. Lackner, J. Steurer, D. Knez, W. Grogger, F. Hofer, and W. E. Ernst. Formation of bimetallic core-shell nanowires along vortices in superfluid He nanodroplets. *Phys. Rev. B*, 90:155442, Oct 2014.

[92] E. Latimer, D. Spence, C. Feng, A. Boatwright, A. M. Ellis, and S. Yang. Preparation of ultrathin nanowires using superfluid helium droplets. *Nano Lett.*, 14(5):2902–2906, 2014. PMID: 24742117.

[93] A. Volk, D. Knez, P. Thaler, A. W. Hauser, W. Grogger, F. Hofer, and W. E. Ernst. Thermal instabilities and Rayleigh breakup of ultrathin silver nanowires grown in helium nanodroplets. *Phys. Chem. Chem. Phys.*, 17(38):24570–24575, 2015.

[94] A. Volk, P. Thaler, D. Knez, A. W. Hauser, J. Steurer, W. Grogger, F. Hofer, and W. E. Ernst. The impact of doping rates on the morphologies of silver and gold nanowires grown in helium nanodroplets. *Phys. Chem. Chem. Phys.*, 18:1451–1459, 2016.

[95] H. Schöbel, P. Bartl, C. Leidlmair, S. Denifl, O. Echt, T. D. Märk, and P. Scheier. High-resolution mass spectrometric study of pure helium droplets, and droplets doped with krypton. *Eur. Phys. J. D*, 63(2):209–214, Jul 2011.

[96] F. Federmann, A. Bartelt, J. D. Close, K. Hoffmann, N. Quaas, and J. P. Toennies. The UV-absorption of europium atoms embedded in helium nanodroplets. *Z. Phys. D*, 39(1):1–2, Mar 1997.

[97] F. Lindebner, A. Kautsch, M. Koch, and W. E. Ernst. Laser ionization and spectroscopy of Cu in superfluid helium nanodroplets. *Int. J. Mass Spectrom.*, 365-366:255 – 259, 2014. Special issue: Tilmann Märk.

[98] S. Grebenev, M. Hartmann, A. Lindinger, N. Pörtner, B. Sartakov, J. P. Toennies, and A. F. Vilesov. Spectroscopy of molecules in helium droplets. *Physica B*, 280(1-4):65–72, 2000.

[99] D. Spence, E. Latimer, W. York, A. Boatwright, C. Feng, S. Yang, and A. M. Ellis. Formation of aluminium clusters in helium nanodroplets. *Int. J. Mass Spectrom.*, 365:86–88, 2014.

[100] M. Mudrich, O. Bünermann, F. Stienkemeier, O. Dulieu, and M. Weidemüller. Formation of cold bialkali dimers on helium nanodroplets. *Eur. Phys. J. D*, 31(2):291–299, 2004.

[101] M. Harnisch, N. Weinberger, S. Denifl, P. Scheier, and O. Echt. Helium droplets doped with sulfur and C_{60}. *J. Phys. Chem. C*, 119(20):10919–10924, 2015. PMID: 26045732.

[102] G. Haberfehlner, P. Thaler, D. Knez, A. Volk, F. Hofer, W. E. Ernst, and G. Kothleitner. Formation of bimetallic clusters in superfluid helium nanodroplets analysed by atomic resolution electron tomography. *Nat. Commun.*, 6:8779, 2015.

[103] E. Loginov, L. F. Gomez, B. G. Sartakov, and A. F. Vilesov. Formation of core–shell ethane–silver clusters in he droplets. *J. Phys. Chem. A*, 121(32):5978–5982, 2017.

[104] O. Bünermann and F. Stienkemeier. Modeling the formation of alkali clusters attached to helium nanodroplets and the abundance of high-spin states. *Eur. Phys. J. D*, 61(3):645–655, 2011.

[105] S. Kuma, H. Goto, M. N. Slipchenko, A. F. Vilesov, A. Khramov, and T. Momose. Laser induced fluorescence of Mg-phthalocyanine in He droplets: Evidence for fluxionality of large H_2 clusters at 0.38 K. *J. Chem. Phys.*, 127(21):214301, 2007.

[106] V. Mozhayskiy, M. N. Slipchenko, V. K. Adamchuk, and A. F. Vilesov. Use of helium nanodroplets for assembly, transport, and surface deposition of large molecular and atomic clusters. *J. Chem. Phys.*, 127(9):094701, 2007.

[107] O. Bünermann, G. Droppelmann, A. Hernando, R. Mayol, and F. Stienkemeier. Unraveling the absorption spectra of alkali metal atoms attached to helium nanodroplets. *J. Phys. Chem. A*, 111(49):12684–12694, 2007.

[108] L. Fechner, B. Grüner, A. Sieg, C. Callegari, F. Ancilotto, F. Stienkemeier, and M. Mudrich. Photoionization and imaging spectroscopy of rubidium atoms attached to helium nanodroplets. *Phys. Chem. Chem. Phys.*, 14(11):3843–3851, 2012.

[109] F. Ancilotto, E. Cheng, M. Cole, and F. Toigo. The binding of alkali atoms to the surfaces of liquid helium and hydrogen. *Z. Phys. B*, 98(3):323–329, 1995.

[110] A. B. Pacheco, B. Thorndyke, A. Reyes, and D. A. Micha. Quantum dynamics of an excited alkali atom in a noble gas cluster: Lithium attached to a helium cluster. *J. Chem. Phys.*, 127(24):244504, 2007.

[111] A. Hernando, M. Barranco, R. Mayol, M. Pi, F. Ancilotto, O. Bünermann, and F. Stienkemeier. Absorption spectrum of Na atoms attached to helium nanodroplets. *J. Low Temp. Phys.*, 158(1-2):105, 2010.

[112] T. Ruchti, K. Förde, B. E. Callicoatt, H. Ludwigs, and K. C. Janda. Charge transfer and fragmentation of liquid helium clusters that contain one or more neon atoms. *J. Chem. Phys.*, 109(24):10679–10687, 1998.

[113] F. Dalfovo. Atomic and molecular impurities in ^{4}He clusters. *Z. Phys. D*, 29(1):61–66, Mar 1994.

[114] A. Bartelt, J. Close, F. Federmann, N. Quaas, and J. Toennies. Cold metal clusters: Helium droplets as a nanoscale cryostat. *Phys. Rev. Lett.*, 77(17):3525, 1996.

[115] A. Kautsch, M. Koch, and W. E. Ernst. Electronic relaxation after resonant laser excitation of Cr in superfluid helium nanodroplets. *J. Phys. Chem. A*, 117(39):9621–9625, 2013. PMID: 23410146.

[116] R. Messner, A. Schiffmann, J. V. Pototschnig, M. Lasserus, M. Schnedlitz, F. Lackner, and W. E. Ernst. Spectroscopy of gold atoms and gold oligomers in helium nanodroplets. *J. Chem. Phys.*, 149(2):024305, 2018.

[117] F. Ancilotto, P. B. Lerner, and M. W. Cole. Physics of solvation. *J. Low Temp. Phys.*, 101(5):1123–1146, Dec 1995.

[118] A. Hernando, R. Mayol, M. Pi, M. Barranco, F. Ancilotto, O. Bünermann, and F. Stienkemeier. The structure and energetics of ^{3}He and ^{4}He nanodroplets doped with alkaline earth atoms. *J. Phys. Chem. A*, 111(31):7303–7308, 2007.

[119] F. Stienkemeier, F. Meier, and H. O. Lutz. Alkaline earth metals (Ca, Sr) attached to liquid helium droplets: Inside or out? *J. Chem. Phys.*, 107(24):10816–10818, 1997.

[120] K. T. Tang and J. P. Toennies. The van der Waals potentials between all the rare gas atoms from He to Rn. *J. Chem. Phys.*, 118(11):4976–4983, 2003.

[121] F. Cargnoni, T. Kuś, M. Mella, and R. J. Bartlett. Ground state potential energy surfaces and bound states of M–He dimers (M=Cu,Ag,Au): A theoretical investigation. *J. Chem. Phys.*, 129(20):204307, 2008.

[122] R. J. Hinde. Mg–He and Ca–He van der Waals interactions: approaching the Born–Oppenheimer limit. *J. Phys. B: At., Mol. Opt. Phys.*, 36(14):3119, 2003.

[123] U. Kleinekathöfer. Ground state potentials for alkaline-earth–helium diatoms calculated by the surface integral method. *Chem. Phys. Lett.*, 324(5):403 – 410, 2000.

[124] E. Czuchaj, H. Stoll, and H. Preuss. Pseudopotential SCF/CI calculations for the potential energies of the MHe and MNe (M=Mg, Cd, Hg) systems. *J. Phys. B: At. Mol. Phys.*, 20(7):1487, 1987.

[125] C. C. Lovallo and M. Klobukowski. Accurate ab initio pair potentials between helium and the heavier group 2 elements. *J. Chem. Phys.*, 120(1):246–252, 2004.

[126] R. D. M. Carty. Thermodynamic properties of helium 4 from 2 to 1500 K at pressures to 108 Pa. *J. Phys. Chem. Ref. Data*, 2(4):923–1042, 1973.

[127] E. Cheng, M. W. Cole, W. F. Saam, and J. Treiner. Wetting transitions of classical liquid films: A nearly universal trend. *Phys. Rev. B*, 48:18214–18221, Dec 1993.

[128] R. J. Donnelly and C. F. Barenghi. The observed properties of liquid helium at the saturated vapor pressure. *J. Phys. Chem. Ref. Data*, 27(6):1217–1274, 1998.

[129] C. Stark and V. V. Kresin. Critical sizes for the submersion of alkali clusters into liquid helium. *Phys. Rev. B*, 81:085401, Feb 2010.

[130] L. An der Lan, P. Bartl, C. Leidlmair, H. Schöbel, R. Jochum, S. Denifl, T. D. Märk, A. M. Ellis, and P. Scheier. The submersion of sodium clusters in helium nanodroplets: Identification of the surface → interior transition. *J. Chem. Phys.*, 135(4):044309, 2011.

[131] L. An der Lan, P. Bartl, C. Leidlmair, H. Schöbel, S. Denifl, T. D. Märk, A. M. Ellis, and P. Scheier. Submersion of potassium clusters in helium nanodroplets. *Phys. Rev. B*, 85:115414, Mar 2012.

[132] M. Renzler, M. Daxner, L. Kranabetter, A. Kaiser, A. W. Hauser, W. E. Ernst, A. Lindinger, R. Zillich, P. Scheier, and A. M. Ellis. Communication: Dopant-induced solvation of alkalis in liquid helium nanodroplets. *J. Chem. Phys.*, 145(18):181101, 2016.

[133] J. von Vangerow, A. Sieg, F. Stienkemeier, M. Mudrich, A. Leal, D. Mateo, A. Hernando, M. Barranco, and M. Pi. Desorption dynamics of heavy alkali

metal atoms (Rb, Cs) off the surface of helium nanodroplets. *J. Phys. Chem. A*, 118(33):6604–6614, 2014. PMID: 24911255.

[134] F. R. Brühl, R. A. Trasca, and W. E. Ernst. Rb–He exciplex formation on helium nanodroplets. *J. Chem. Phys.*, 115(22):10220–10224, 2001.

[135] B. Tabbert, H. Günther, and G. Zu Putlitz. Optical investigation of impurities in superfluid ^{4}He. *J. Low Temp. Phys.*, 109(5-6):653–707, 1997.

[136] A. P. Hickman, W. Steets, and N. F. Lane. Nature of excited helium atoms in liquid helium: A theoretical model. *Phys. Rev. B*, 12:3705–3717, Nov 1975.

[137] G. DeToffol, F. Ancilotto, and F. Toigo. Excited states of alkali atoms in liquid ^{4}He from density functional calculations. *Journal of Low Temperature Physics*, 102(5):381–410, Mar 1996.

[138] V. Ludwig, P. K. Mukherjee, K. Coutinho, and S. Canuto. Spectral shift of sodium in a liquid-helium environment: A sequential Monte Carlo time-dependent density-functional-theory study. *Phys. Rev. A*, 72:062714, Dec 2005.

[139] J. Anton, B. Fricke, P. Mukherjee, and S. Fritzsche. Ab-initio relativistic density functional calculations for spectral line shifts of Rb atoms in liquid helium. *Physics Letters A*, 372(24):4462 – 4464, 2008.

[140] L. Modesto-Costa, P. K. Mukherjee, and S. Canuto. A CASPT2 study of the spectral shift of the resonance emission lines of Rb and Cs embedded in liquid He. *Chem. Phys. Lett.*, 655-656:91 – 95, 2016.

[141] F. F. da Silva, P. Bartl, S. Denifl, O. Echt, T. D. Märk, and P. Scheier. Argon clusters embedded in helium nanodroplets. *Phys. Chem. Chem. Phys.*, 11(42):9791–9797, 2009.

[142] A. Przystawik, P. Radcliffe, S. Göde, K. Meiwes-Broer, and J. Tiggesbäumker. Spectroscopy of silver dimers in triplet states. *J. Phys. B: At., Mol. Opt. Phys.*, 39(19):S1183, 2006.

[143] A. Przystawik, P. Radcliffe, T. Diederich, T. Döppner, J. Tiggesbäumker, and K.-H. Meiwes-Broer. Photoelectron studies of neutral Ag$_3$ in helium droplets. *J. Chem. Phys.*, 126(18):184306, 2007.

[144] C. C. Wang, O. Kornilov, O. Gessner, J. H. Kim, D. S. Peterka, and D. M. Neumark. Photoelectron imaging of helium droplets doped with Xe and Kr atoms. *J. Phys. Chem. A*, 112(39):9356–9365, 2008. PMID: 18690675.

[145] F. Stienkemeier, F. Meier, and H. Lutz. Spectroscopy of barium attached to superfluid helium clusters. *Eur. Phys. J. D*, 9(1):313–315, 1999.

[146] J.-Z. Tang, M. Kimura, and I. Shimamura. Absorption and emission spectra of alkaline-earth atoms in liquid helium: a theoretical study. *Chem. Phys. Lett.*, 256(3):327 – 333, 1996.

[147] M. Rossi, M. Verona, D. E. Galli, and L. Reatto. Alkali and alkali-earth ions in ^{4}He systems. *Phys. Rev. B*, 69:212510, Jun 2004.

[148] R. E. Zillich, Y. Kwon, and K. B. Whaley. Roton-rotation coupling of acetylene in ^{4}He. *Phys. Rev. Lett.*, 93(25):250401, 2004.

[149] A. Hernando, M. Barranco, R. Mayol, M. Pi, and F. Ancilotto. Density functional theory of the structure of magnesium-doped helium nanodroplets. *Phys. Rev. B*, 78(18):184515, 2008.

[150] D. Mateo, A. Hernando, M. Barranco, E. Loginov, M. Drabbels, and M. Pi. Translational dynamics of photoexcited atoms in ^{4}He nanodroplets: the case of silver. *Phys. Chem. Chem. Phys.*, 15:18388–18400, 2013.

[151] E. Loginov, D. Rossi, and M. Drabbels. Photoelectron spectroscopy of doped helium nanodroplets. *Phys. Rev. Lett.*, 95(16):163401, 2005.

[152] D. S. Peterka, J. H. Kim, C. C. Wang, L. Poisson, and D. M. Neumark. Photoionization dynamics in pure helium droplets. *J. Phys. Chem. A*, 111(31):7449–7459, 2007. PMID: 17571863.

[153] M. Theisen, F. Lackner, G. Krois, and W. E. Ernst. Ionization thresholds of alkali metal atoms on helium droplets. *J. Phys. Chem. Lett.*, 2(21):2778–2782, 2011.

[154] F. Lackner, G. Krois, and W. E. Ernst. Lithium atoms on helium nanodroplets: Rydberg series and ionization dynamics. *J. Chem. Phys.*, 147(18):184302, 2017.

[155] E. Loginov and M. Drabbels. Spectroscopy and dynamics of barium-doped helium nanodroplets. *J. Chem. Phys.*, 136(15):154302, 2012.

[156] T. Döppner, T. Diederich, S. Göde, A. Przystawik, J. Tiggesbäumker, and K.-H. Meiwes-Broer. Ion induced snowballs as a diagnostic tool to investigate the caging of metal clusters in large helium droplets. *J. Chem. Phys.*, 126(24):244513, 2007.

[157] P. Bartl, C. Leidlmair, S. Denifl, P. Scheier, and O. Echt. On the size and structure of helium snowballs formed around charged atoms and clusters of noble gases. *J. Phys. Chem. A*, 118(37):8050–8059, 2014. PMID: 24128371.

[158] F. Coppens, J. Von Vangerow, M. Barranco, N. Halberstadt, F. Stienkemeier, M. Pi, and M. Mudrich. Desorption dynamics of RbHe exciplexes off He nanodroplets induced by spin-relaxation. *Phys. Chem. Chem. Phys.*, 20(14):9309–9320, 2018.

[159] T. Döppner, T. Diederich, A. Przystawik, N. Truong, T. Fennel, J. Tiggesbäumker, and K.-H. Meiwes-Broer. Charging of metal clusters in helium droplets exposed to intense femtosecond laser pulses. *Phys. Chem. Chem. Phys.*, 9(33):4639–4652, 2007.

[160] E. Loginov and M. Drabbels. Dynamics of excited sodium atoms attached to helium nanodroplets. *J. Phys. Chem. A*, 118(15):2738–2748, 2014. PMID: 24673631.

[161] E. Loginov, A. Hernando, J. A. Beswick, N. Halberstadt, and M. Drabbels. Excitation of sodium atoms attached to helium nanodroplets: The 3p ← 3s transition revisited. *J. Phys. Chem. A*, 119(23):6033–6044, 2015. PMID: 25582680.

[162] N. V. Dozmorov, A. V. Baklanov, J. von Vangerow, F. Stienkemeier, J. A. M. Fordyce, and M. Mudrich. Quantum dynamics of Rb atoms desorbing off the surface of He nanodroplets. *Phys. Rev. A*, 98:043403, Oct 2018.

[163] E. Loginov and M. Drabbels. Excited state dynamics of Ag atoms in helium nanodroplets. *J. Phys. Chem. A*, 111:7504–7515, 2007.

[164] M. Ratschek, J. V. Pototschnig, A. W. Hauser, and W. E. Ernst. Solvation and spectral line shifts of chromium atoms in helium droplets based on a density functional theory approach. *J. Phys. Chem. A*, 118(33):6622–6631, 2014.

[165] N. B. Brauer, S. Smolarek, E. Loginov, D. Mateo, A. Hernando, M. Pi, M. Barranco, W. J. Buma, and M. Drabbels. Critical Landau velocity in helium nanodroplets. *Phys. Rev. Lett.*, 111(15):153002, 2013.

[166] X. Zhang and M. Drabbels. Communication: Barium ions and helium nanodroplets: Solvation and desolvation. *J. Chem. Phys.*, 2012.

[167] J. von Vangerow, F. Coppens, A. Leal, M. Pi, M. Barranco, N. Halberstadt, F. Stienkemeier, and M. Mudrich. Imaging excited-state dynamics of doped He nanodroplets in real-time. *J. Phys. Chem. Lett.*, 8(1):307–312, 2017. PMID: 27996261.

[168] J. Harms, M. Hartmann, B. Sartakov, J. P. Toennies, and A. F. Vilesov. High resolution infrared spectroscopy of single SF_6 molecules in helium droplets. II. The effect of small amounts of ^{4}He in large ^{3}He droplets. *J. Chem. Phys.*, 110(11):5124–5136, 1999.

[169] D. A. Thomas, E. Mucha, S. Gewinner, W. Schöllkopf, G. Meijer, and G. von Helden. Vibrational spectroscopy of fluoroformate, FCO_2^-, trapped in helium nanodroplets. *J. Phys. Chem. Lett.*, 9(9):2305–2310, 2018. PMID: 29669208.

[170] B. Dick and A. Slenczka. Inhomogeneous line shape theory of electronic transitions for molecules embedded in superfluid helium droplets. *J. Chem. Phys.*, 115(22):10206–10213, 2001.

[171] R. Lehnig and A. Slenczka. Spectroscopic investigation of the solvation of organic molecules in superfluid helium droplets. *J. Chem. Phys.*, 122(24):244317, 2005.

[172] D. Pentlehner, R. Riechers, A. Vdovin, G. M. Pötzl, and A. Slenczka. Electronic spectroscopy of molecules in superfluid helium nanodroplets: An excellent sensor for intramolecular charge redistribution. *J. Phys. Chem. A*, 115(25):7034–7043, 2011. PMID: 21615111.

[173] A. Vdovin, A. Slenczka, and B. Dick. Electronic spectroscopy of lumiflavin in superfluid helium nanodroplets. *Chem. Phys.*, 422:195 – 203, 2013. A tribute to Dr. Robin Hochstasser.

[174] R. Lehnig and A. Slenczka. Emission spectra of free base phthalocyanine in superfluid helium droplets. *J. Chem. Phys.*, 118(18):8256–8260, 2003.

[175] S. Fuchs, J. Fischer, A. Slenczka, M. Karra, and B. Friedrich. Microsolvation of phthalocyanine molecules in superfluid helium nanodroplets as revealed by the optical line shape at electronic origin. *J. Chem. Phys.*, 148(14):144301, 2018.

[176] A. Braun and M. Drabbels. Photodissociation of alkyl iodides in helium nanodroplets. I. Kinetic energy transfer. *J. Chem. Phys.*, 127(11):114303, 2007.

[177] A. Braun and M. Drabbels. Photodissociation of alkyl iodides in helium nanodroplets. II. Solvation dynamics. *J. Chem. Phys.*, 127(11):114304, 2007.

[178] A. Braun and M. Drabbels. Photodissociation of alkyl iodides in helium nanodroplets. III. Recombination. *J. Chem. Phys.*, 127(11):114305, 2007.

[179] M. Briant, E. Mengesha, M.-A. Gaveau, B. Soep, J.-M. Mestdagh, and L. Poisson. Dynamics of acetylene dimers hosted in helium droplets. *Phys. Chem. Chem. Phys.*, 20(4):2597–2605, 2018.

[180] J. D. Pickering, B. Shepperson, B. A. K. Hübschmann, F. Thorning, and H. Stapelfeldt. Alignment and imaging of the CS_2 dimer inside helium nanodroplets. *Phys. Rev. Lett.*, 120:113202, Mar 2018.

[181] J. D. Pickering, B. Shepperson, L. Christiansen, and H. Stapelfeldt. Femtosecond laser induced coulomb explosion imaging of aligned OCS oligomers inside helium nanodroplets. *J. Chem. Phys.*, 149(15):154306, 2018.

[182] J. Higgins, C. Callegari, J. Reho, F. Stienkemeier, W. E. Ernst, K. K. Lehmann, M. Gutowski, and G. Scoles. Photoinduced chemical dynamics of high-spin alkali trimers. *Science*, 273(5275):629–631, 1996.

[183] J. Higgins, C. Callegari, J. Reho, F. Stienkemeier, W. E. Ernst, M. Gutowski, and G. Scoles. Helium cluster isolation spectroscopy of alkali dimers in the triplet manifold. *J. Phys. Chem. A*, 102(26):4952–4965, 1998.

[184] A. Kramida, Yu. Ralchenko, J. Reader, and and NIST ASD Team. NIST Atomic Spectra Database (ver. 5.5.2), [Online]. Available: `https://physics.nist.gov/asd` [2018, March 1]. National Institute of Standards and Technology, Gaithersburg, MD., 2018.

[185] R. Okasaka and K. Fukuda. Doubly excited levels of alkaline-earth elements near the first ionisation limit. I. Magnesium. *J. Phys. B: At., Mol. Opt. Phys.*, 15(3):347–355, feb 1982.

[186] J. Reho, U. Merker, M. R. Radcliff, K. K. Lehmann, and G. Scoles. Spectroscopy of Mg atoms solvated in helium nanodroplets. *J. Chem. Phys.*, 112(19):8409–8416, 2000.

[187] T. Diederich, T. Döppner, J. Braune, J. Tiggesbäumker, and K.-H. Meiwes-Broer. Electron delocalization in magnesium clusters grown in supercold helium droplets. *Phys. Rev. Lett.*, 86(21):4807, 2001.

[188] T. Döppner, T. Diederich, J. Tiggesbäumker, and K.-H. Meiwes-Broer. Femtosecond ionization of magnesium clusters grown in ultracold helium droplets. *Eur. Phys. J. D*, 16(1):13–16, 2001.

[189] S. Goede, R. Irsig, J. Tiggesbäumker, and K.-H. Meiwes-Broer. Time-resolved studies on the collapse of magnesium atom foam in helium nanodroplets. *New J. Phys.*, 15:015026, 2013.

[190] Y. Moriwaki and N. Morita. Ultraviolet spectra of Mg in liquid helium. *Eur. Phys. J. D*, 5(1):53–57, Jan 1999.

[191] Y. Moriwaki, K. Inui, K. Kobayashi, F. Matsushima, and N. Morita. Laser spectroscopic study of Mg atoms in pressurized liquid helium. *J. Mol. Struct.*, 786(2-3):112–117, 2006.

[192] M. Mella, G. Calderoni, and F. Cargnoni. Predicting atomic dopant solvation in helium clusters: The $MgHe_n$ case. *J. Chem. Phys.*, 123(5):054328, 2005.

[193] S. Göde. *Strahlungsfeldinduzierte Korrelationen in Atomaggregaten, Clustern und Mikrotropfen.* PhD thesis, University of Rostock, 2013.

[194] S. Göde, L. Kazak, A. Przystawik, M. Siegfried, J. Tiggesbäumker, and K.-H. Meiwes-Broer. Growth study of magnesium foam ensembles in helium nanodroplets. In preparation.

[195] W. A. de Heer. The physics of simple metal clusters: experimental aspects and simple models. *Rev. Mod. Phys.*, 65:611–676, Jul 1993.

[196] I. A. Solov'yov, A. V. Solov'yov, and W. Greiner. Optical response of small magnesium clusters. *J. Phys. B: At., Mol. Opt. Phys.*, 37(7):L137, 2004.

[197] H. Knöckel, S. Rühmann, and E. Tiemann. The $X^1\Sigma_g^+$ ground state of Mg_2 studied by fourier-transform spectroscopy. *J. Chem. Phys.*, 138(9):094303, 2013.

[198] E. Krotscheck and R. E. Zillich. Solvation of Mg in helium-4: Are there meta-stable Mg dimers? *J. Chem. Phys.*, 145:244317, 2016.

[199] H. Knöckel, S. Rühmann, and E. Tiemann. The $A^1\Sigma_u^+ + (1)^1\Pi_u$ system of Mg_2. *Eur. Phys. J. D*, 68(10):293, Oct 2014.

[200] T. Diederich, T. Döppner, T. Fennel, J. Tiggesbäumker, and K.-H. Meiwes-Broer. Shell structure of magnesium and other divalent metal clusters. *Phys. Rev. A*, 72(2):023203, 2005.

[201] A. Castleman Jr and R. Keesee. Clusters: properties and formation. *Annu. Rev. Phys. Chem.*, 37(1):525–550, 1986.

[202] H. Göhlich, T. Lange, T. Bergmann, U. Näher, and T. Martin. Ionization energies of sodium clusters containing up to 22000 atoms. *Chem. Phys. Lett.*, 187(1):67 – 72, 1991.

[203] G. Wrigge, M. Astruc Hoffmann, B. von Issendorff, and H. Haberland. Ultraviolet photoelectron spectroscopy of Nb_4^- to Nb_{200}^-. *Eur. Phys. J. D*, 24(1):23–26, Jun 2003.

[204] W. D. Knight, K. Clemenger, W. A. de Heer, W. A. Saunders, M. Y. Chou, and M. L. Cohen. Electronic shell structure and abundances of sodium clusters. *Phys. Rev. Lett.*, 52:2141–2143, Jun 1984.

[205] J. A. Alonso. Electronic and atomic structure, and magnetism of transition-metal clusters. *Chem. Rev.*, 100(2):637–678, 2000. PMID: 11749247.

[206] F. Baletto and R. Ferrando. Structural properties of nanoclusters: Energetic, thermodynamic, and kinetic effects. *Rev. Mod. Phys.*, 77:371–423, May 2005.

[207] W. Miehle, O. Kandler, T. Leisner, and O. Echt. Mass spectrometric evidence for icosahedral structure in large rare gas clusters: Ar, Kr, Xe. *J. Chem. Phys.*, 91(10):5940–5952, 1989.

[208] T. Martin. Shells of atoms. *Phys. Rep.*, 273(4):199 – 241, 1996.

[209] V. Kumar. Icosahedral symmetry in clusters. *Prog. Cryst. Growth Charact. Mater.*, 34(1):95 – 131, 1997.

[210] D. Rayane, P. Melinon, B. Cabaud, A. Hoareau, B. Tribollet, and M. Broyer. Close-packing structure of small barium clusters. *Phys. Rev. A*, 39:6056–6059, Jun 1989.

[211] T. Martin, T. Bergmann, H. Göhlich, and T. Lange. Evidence for icosahedral shell structure in large magnesium clusters. *Chem. Phys. Lett.*, 176(3):343 – 347, 1991.

[212] T. Martin, U. Näher, T. Bergmann, H. Göhlich, and T. Lange. Observation of icosahedral shells and subshells in calcium clusters. *Chem. Phys. Lett.*, 183(1):119 – 124, 1991.

[213] W. Knight, W. A. de Heer, K. Clemenger, and W. A. Saunders. Electronic shell structure in potassium clusters. *Solid State Commun.*, 53(5):445 – 446, 1985.

[214] I. Katakuse, T. Ichihara, Y. Fujita, T. Matsuo, T. Sakurai, and H. Matsuda. Mass distributions of copper, silver and gold clusters and electronic shell structure. *Int. J. Mass Spectrom. Ion Processes*, 67(2):229 – 236, 1985.

[215] I. Katakuse, T. Ichihara, Y. Fujita, T. Matsuo, T. Sakurai, and H. Matsuda. Correlation between mass distributions of zinc, cadmium clusters and electronic shell structure. *Int. J. Mass Spectrom. Ion Processes*, 69(1):109 – 114, 1986.

[216] I. Katakuse, T. Ichihara, M. Morris, T. Matsuo, T. Sakurai, and H. Matsuda. Mass distributions of positive and negative cluster ions of zinc and cadmium. *Int. J. Mass Spectrom. Ion Processes*, 91(1):85 – 91, 1989.

[217] G. Alameddin, J. Hunter, D. Cameron, and M. M. Kappes. Electronic and geometric structure in silver clusters. *Chem. Phys. Lett.*, 192(1):122 – 128, 1992.

[218] T. Martin, T. Bergmann, H. Göhlich, and T. Lange. Observation of electronic shells and shells of atoms in large Na clusters. *Chem. Phys. Lett.*, 172(3):209 – 213, 1990.

[219] T. Martin, U. Näher, and H. Schaber. Evidence for octahedral shell structure in aluminum clusters. *Chem. Phys. Lett.*, 199(5):470 – 474, 1992.

[220] B. Baguenard, M. Pellarin, J. Lermé, J. L. Vialle, and M. Broyer. Competition between atomic shell and electronic shell structures in aluminum clusters. *J. Chem. Phys.*, 100(1):754–755, 1994.

[221] J. Zhao, Y. Luo, and G. Wang. Tight-binding study of structural and electronic properties of silver clusters. *Eur. Phys. J. D*, 14(3):309–316, Jun 2001.

[222] J. Wang, G. Wang, and J. Zhao. Density-functional study of Au_n (n=2-20) clusters: Lowest-energy structures and electronic properties. *Phys. Rev. B*, 66:035418, Jul 2002.

[223] K. Clemenger. Ellipsoidal shell structure in free-electron metal clusters. *Phys. Rev. B*, 32:1359–1362, Jul 1985.

[224] B. R. Mottelson and S. G. Nilsson. Classification of the nucleonic states in deformed nuclei. *Phys. Rev.*, 99:1615–1617, Sep 1955.

[225] S. G. Nilsson, C. F. Tsang, A. Sobiczewski, Z. Szymański, S. Wycech, C. Gustafson, I.-L. Lamm, P. Möller, and B. Nilsson. On the nuclear structure and stability of heavy and superheavy elements. *Nucl. Phys. A*, 131(1):1 – 66, 1969.

[226] M. Brack. The physics of simple metal clusters: self-consistent jellium model and semiclassical approaches. *Rev. Mod. Phys.*, 65:677–732, Jul 1993.

[227] W. Ekardt and Z. Penzar. Self-consistent sommerfeld droplet as a simple model for an accurate prediction of the electronic properties of small metal particles. *Phys. Rev. B*, 38:4273–4276, Aug 1988.

[228] T. Hirschmann, M. Brack, and J. Meyer. Spheroidally deformed sodium clusters in the selfconsistent jellium model. *Annalen der Physik*, 506(5):336–369, 1994.

[229] M. Chou, A. Cleland, and M. L. Cohen. Total energies, abundances, and electronic shell structure of lithium, sodium, and potassium clusters. *Solid State Commun.*, 52(7):645 – 648, 1984.

[230] B. Baguenard, M. Pellarin, C. Bordas, J. Lermé, J. Vialle, and M. Broyer. Shell structure of small indium clusters below n≈200 atoms. *Chem. Phys. Lett.*, 205(1):13 – 18, 1993.

[231] S. Bjørnholm, J. Borggreen, O. Echt, K. Hansen, J. Pedersen, and H. D. Rasmussen. Mean-field quantization of several hundred electrons in sodium metal clusters. *Phys. Rev. Lett.*, 65:1627–1630, Sep 1990.

[232] M. Seidl, K.-H. Meiwes-Broer, and M. Brack. Finite-size effects in ionization potentials and electron affinities of metal clusters. *J. Chem. Phys.*, 95(2):1295–1303, 1991.

[233] D. M. Wood. Classical size dependence of the work function of small metallic spheres. *Phys. Rev. Lett.*, 46:749–749, Mar 1981.

[234] H. G. Limberger and T. P. Martin. Photoionization spectra of cesium and cesium oxide clusters. *J. Chem. Phys.*, 90(6):2979–2991, 1989.

[235] S. Yang and M. B. Knickelbein. Photoionization studies of transition metal clusters: Ionization potentials for Fe_n and Co_n. *J. Chem. Phys.*, 93(3):1533–1539, 1990.

[236] M. B. Knickelbein, S. Yang, and S. J. Riley. Near-threshold photoionization of nickel clusters: Ionization potentials for Ni_3 to Ni_{90}. *J. Chem. Phys.*, 93(1):94–104, 1990.

[237] M. B. Knickelbein. Photoionization studies of chromium clusters: Ionization energies of Cr_4 to Cr_{25}. *Phys. Rev. A*, 67:013202, Jan 2003.

[238] G. M. Koretsky and M. B. Knickelbein. Photoionization studies of manganese clusters: Ionization potentials for Mn_7 to Mn_{64}. *J. Chem. Phys.*, 106(23):9810–9814, 1997.

[239] K. H. Meiwes-Broer. Work functions of metal clusters. *Hyperfine Interact.*, 89(1):263–269, Dec 1994.

[240] B. von Issendorff and O. Cheshnovsky. Metal to insulator transitions in clusters. *Annu. Rev. Phys. Chem.*, 56(1):549–580, 2005. PMID: 15796711.

[241] J. P. Perdew. Energetics of charged metallic particles: From atom to bulk solid. *Phys. Rev. B*, 37:6175–6180, Apr 1988.

[242] M. B. Knickelbein and S. Yang. Photoionization studies of niobium clusters: Ionization potentials for Nb_2–Nb_{76}. *The Journal of Chemical Physics*, 93(8):5760–5767, 1990.

[243] K. Rademann, B. Kaiser, U. Even, and F. Hensel. Size dependence of the gradual transition to metallic properties in isolated mercury clusters. *Phys. Rev. Lett.*, 59:2319–2321, Nov 1987.

[244] R. Busani, M. Folkers, and O. Cheshnovsky. Direct observation of band-gap closure in mercury clusters. *Phys. Rev. Lett.*, 81:3836–3839, Nov 1998.

[245] K. Hoffmann. *Heliumcluster als kalte, flüssige Matrix zur Laserspektroskopie von Silberatomen, Silberclustern und C_{60}-Fullerenen.* PhD thesis, Max–Planck–Institut für Strömungsforschung, Göttingen, 1999.

[246] C. Alcock, V. Itkin, and M. Horrigan. Vapour pressure equations for the metallic elements: 298–2500 K. *Can. Metall. Q.*, 23(3):309–313, 1984.

[247] N. Quaas. Spektroskopie an kalten metallclustern eingelagert in heliumtröpfchen. Diplomarbeit, Max–Planck–Institut für Strömungsforschung, Göttingen, 1997.

[248] S. C. Köhnke. Magnesium complexes in superfluid helium droplets. Master's thesis, University of Rostock, 2015.

[249] P. Kruit, J. Kimman, and M. J. V. der Wiel. Absorption of additional photons in the multiphoton ionisation continuum of xenon at 1064, 532 and 440 nm. *J. Phys. B: At. Mol. Phys.*, 14(19):L597, 1981.

[250] P. Kruit and F. H. Read. Magnetic field paralleliser for 2π electron-spectrometer and electron-image magnifier. *J. Phys. E: Sci. Instrum.*, 16(4):313, 1983.

[251] P. Radcliffe. *The Ionization Dynamics of Silver Clusters after Exposure to Strong Laser Pulses.* PhD thesis, Universität Rostock, 2005.

[252] B. Mamyrin. Time-of-flight mass spectrometry (concepts, achievements, and prospects). *Int. J. Mass Spectrom.*, 206(3):251–266, 2001.

[253] W. Wiley and I. H. McLaren. Time-of-flight mass spectrometer with improved resolution. *Rev. Sci. Instrum.*, 26(12):1150–1157, 1955.

[254] F. Chandezon, B. Huber, and C. Ristori. A new-regime Wiley-McLaren time-of-flight mass spectrometer. *Review of Scientific Instruments*, 65(11):3344–3353, 1994.

[255] S. M. Colby, T. B. King, J. P. Reilly, and D. M. Lubman. Improving the resolution of matrix-assisted laser desorption/ionization time-of-flight mass spectrometry by exploiting the correlation between ion position and velocity. *Rapid Communications in Mass Spectrometry*, 8(11):865–868, 1994.

[256] B. A. Mamyrin, V. I. Karataev, D. V. Shmikk, and V. A. Zagulin. The mass-reflectron, a new nonmagnetic time-of-flight mass spectrometer with high resolution. *Sov. Phys. JETP*, 37(1):45–48, 1973.

[257] O. Svelto and D. C. Hanna. *Principles of lasers*, volume 4. Springer, 1998.

[258] M. Taniguchi, H. Du, and J. S. Lindsey. Photochemcad 3: Diverse modules for photophysical calculations with multiple spectral databases. *Photochemistry and Photobiology*, 94(2):277–289, 2018.

[259] J. Navarro, D. Mateo, M. Barranco, and A. Sarsa. Mg impurity in helium droplets. *J. Chem. Phys.*, 136(5):02B602, 2012.

[260] Y. Ren and V. V. Kresin. Surface location of alkaline-earth-metal-atom impurities on helium nanodroplets. *Phys. Rev. A*, 76(4):043204, 2007.

[261] L. Kazak, S. Göde, K.-H. Meiwes-Broer, and J. Tiggesbäumker. Photoelectron spectroscopy on magnesium ensembles in helium nanodroplets. *J. Phys. Chem. A*, 123(28):5951–5956, 2019. PMID: 31240915.

[262] S. Amaran, R. Kosloff, M. Tomza, W. Skomorowski, F. Pawłowski, R. Moszynski, L. Rybak, L. Levin, Z. Amitay, J. M. Berglund, D. M. Reich, and C. P. Koch. Femtosecond two-photon photoassociation of hot magnesium atoms: A quantum dynamical study using thermal random phase wavefunctions. *J. Chem. Phys.*, 139(16):164124, 2013.

[263] R. E. Continetti. Ccoincidence spectroscopy. *Annu. Rev. Phys. Chem.*, 52(1):165–192, 2001. PMID: 11326063.

[264] A. Leal, D. Mateo, A. Hernando, M. Pi, and M. Barranco. Capture of heliophobic atoms by ^{4}He nanodroplets: the case of cesium. *Phys. Chem. Chem. Phys.*, 16(42):23206–23213, 2014.

[265] F. Coppens, A. Leal, M. Barranco, N. Halberstadt, and M. Pi. Head-on collisions of Xe atoms against superfluid ^{4}He nanodroplets. *J. Low Temp. Phys.*, 187(5-6):439–445, 2017.

[266] A. Vilà, M. González, and R. Mayol. Relaxation dynamics of helium nanodroplets after photodissociation of a dopant homonuclear diatomic molecule. The case of $Cl_2@(^4He)_N$. *Phys. Chem. Chem. Phys.*, 18(4):2409–2416, 2016.

[267] M. Kelbg, A. Heidenreich, L. Kazak, M. Zabel, B. Krebs, K.-H. Meiwes-Broer, and J. Tiggesbäumker. Comparison of electron and ion emission from xenon cluster-induced ignition of helium nanodroplets. *J. Phys. Chem. A*, 122(41):8107–8113, 2018. PMID: 30239204.

[268] J. Jellinek and P. H. Acioli. Magnesium clusters: structural and electronic properties and the size-induced nonmetal-to-metal transition. *J. Phys. Chem. A*, 106(45):10919–10925, 2002.

[269] O. C. Thomas, W. Zheng, S. Xu, and K. H. Bowen. Onset of metallic behavior in magnesium clusters. *Phys. Rev. Lett.*, 89:213403, Nov 2002.

[270] V. Kempter, F. Veith, and L. Zehnle. Study of the optical emission in Ne+Ne and Ar+Ar collisions in the range 15 to 500 eV. *J. Phys. B: At. Mol. Opt. Phys.*, 8(17):2835, 1975.

[271] V. Kempter, F. Veith, and L. Zehnle. Excitation processes in low-energy collisions between ground state helium atoms. *J. Phys. B: At. Mol. Opt. Phys.*, 8(7):1041, 1975.

[272] W. Mecklenbrauck, J. Schon, E. Speller, and V. Kempter. Study of the optical emission in collisions between sodium and noble-gas atoms in the energy range between 10 and 500 eV. *J. Phys. B: At. Mol. Opt. Phys.*, 10(16):3271, 1977.

[273] N. Andersen, T. Andersen, K. Bahr, C. L. Cocke, E. H. Pedersen, and J. O. Olsen. Differential-excitation studies of quasi-one-electron systems. i. Na 3^2P excitation in Na-He, Ne, Ar collisions. *J. Phys. B: At. Mol. Opt. Phys.*, 12(15):2529, 1979.

[274] C. Courbin-Gaussorgues and V. Sidis. Theoretical study of the Na(3s-3p) excitation in Na+He collisions. *J. Phys. B: At. Mol. Opt. Phys.*, 18(4):699, 1985.

[275] A. Kopystyńska and L. Moi. Energy transfer in collisions between excited atoms. *Phys. Rep.*, 92(4):135 – 181, 1982.

[276] A. Bambini, P. R. Berman, R. Buffa, E. J. Robinson, and M. Matera. Laser-induced collisional energy transfer. *Phys. Rep.*, 238(5):245 – 339, 1994.

[277] M. Allegrini, G. Alzetta, A. Kopystyńska, L. Moi, and G. Orriols. Electronic energy transfer induced by collision between two excited sodium atoms. *Opt. Commun*, 19(1):96–99, 1976.

[278] M. Allegrini, P. Bicchi, and L. Moi. Cross-section measurement for the energy-transfer collisions Na($3p$)+Na($3p$) $\rightarrow$ Na($5s, 4d$)+Na($3s$). *Phys. Rev. A*, 28:1338–1343, Sep 1983.

[279] Z. J. Jabbour, R. K. Namiotka, J. Huennekens, M. Allegrini, S. Milošević, and F. de Tomasi. Energy-pooling collisions in cesium: 6P$_J$+6P$_J$→6S+(nl=7P,6D,8S,4F). *Phys. Rev. A*, 54:1372–1384, Aug 1996.

[280] R. K. Namiotka, J. Huennekens, and M. Allegrini. Energy-pooling collisions in potassium: $4P_J$+$4P_J$ $\rightarrow$ $4S$ + ($nl = 5P, 6S, 4D$). *Phys. Rev. A*, 56:514–520, Jul 1997.

[281] C. Vadla. Energy pooling in caesium vapour:. *Eur. Phys. J. D*, 1(3):259–264, Apr 1998.

[282] P. H. T. Philipsen, J. H. Nijland, H. Rudolph, and H. G. M. Heideman. Semi-classical calculations for energy transfer reactions in collisions between polarized sodium atoms. *J. Phys. B: At. Mol. Opt. Phys.*, 26(5):939, 1993.

[283] S. Gozzini, S. Abdullah, M. Allegrini, A. Cremoncini, and L. Moi. Heteronuclear energy pooling collisions: The Na(3P) + K(4P) reaction. *Opt. Commun*, 63(2):97 – 102, 1987.

[284] C. Gabbanini, S. Gozzini, G. Squadrito, M. Allegrini, and L. Moi. Energy-pooling collisions for K(4P)+Rb(5P) and Na(3P)+Rb(5P) heteronuclear systems. *Phys. Rev. A*, 39:6148–6153, Jun 1989.

[285] G. De Filippo, S. Guldberg-Kjær, S. Milošević, J. O. P. Pedersen, and M. Allegrini. Reverse energy pooling in a K-Na mixture. *Phys. Rev. A*, 57:255–266, Jan 1998.

[286] D. Zhang, B. Chen, R. Ju, and X. Zhao. Experimental observation on anomalous emission in Mg vapor. *Opt. Commun*, 55(1):13–16, 1985.

[287] A. T. Pritt, D. Patel, and D. J. Benard. Energy transfer and pooling between magnesium(3P) and calcium atoms. *J. Phys. Chem.*, 90(1):72–75, 1986.

[288] J. A. Neuman, A. Gallagher, and J. Cooper. Energy-pooling collisions in barium. *Phys. Rev. A*, 50:1292–1300, Aug 1994.

[289] P. Bicchi, C. Marinelli, E. Mariotti, M. Meucci, and L. Moi. Energy pooling collision cross section measurements in indium: the $In(6S_{1/2})+In(6S_{1/2})$ to $In(nP)+In(5P_{3/2})$ process. *J. Phys. B: At. Mol. Opt. Phys.*, 26(15):2335, 1993.

[290] S. Majetich, E. M. Boczar, and J. R. Wiesenfeld. Energy pooling and associative ionization following laser excitation of mercury vapor. *J. Appl. Phys.*, 66(2):475–481, 1989.

[291] J. Lorenzen, H. Hotop, M. W. Ruf, and H. Morgner. Rovibronic structure in the electron energy spectrum for associative ionization: Ne(3p2), ar(3p2)+h. *Z. Phys. A*, 297(1):19–23, Mar 1980.

[292] T. Baumert, R. Thalweiser, V. Weiß, and G. Gerber. Time-resolved studies of neutral and ionized nan clusters with femtosecond light pulses. *Z. Phys. D*, 26(1):131–134, Mar 1993.

[293] J. Akola, K. Rytkönen, and M. Manninen. Metallic evolution of small magnesium clusters. *Eur. Phys. J. D*, 16(1):21–24, 2001.

[294] A. Lyalin, I. A. Solov'yov, A. V. Solov'yov, and W. Greiner. Evolution of the electronic and ionic structure of Mg clusters with increase in cluster size. *Phys. Rev. A*, 67(6):063203, 2003.

[295] S. Janecek, E. Krotscheck, M. Liebrecht, and R. Wahl. Structure of Mg_n and Mg_n^+ clusters up to n=30. *Eur. Phys. J. D*, 63(3):377–390, Aug 2011.

[296] P. J. Ziemann and A. W. Castleman. Mass spectrometric study of MgO clusters produced by the gas aggregation technique. *Z. Phys. D*, 20(1):97–99, Mar 1991.

[297] T. Bergmann and T. P. Martin. Observation of electronic shell structure in large cesium oxide clusters. *J. Chem. Phys.*, 90(6):2848–2855, 1989.

[298] J. Jellinek and P. H. Acioli. Magnesium clusters: structural and electronic properties and the size-induced nonmetal-to-metal transition. *J. Phys. Chem. A*, 106(45):10919–10925, 2002.

[299] N. W. Ashcroft and N. D. Mermin. *Solid State Physics*. Saunders College Publishing, 1976.

[300] M. Y. Chou and M. L. Cohen. Electronic shell structure in simple metal clusters. *Phys. Lett. A*, 113(8):420 – 424, 1986.

[301] D. R. Lide, editor. *CRC Handbook of Chemistry and Physics*. CRC Press, Boca Raton, FL, 2005.

[302] M. Seidl and M. Brack. Liquid drop model for charged spherical metal clusters. *Ann. Phys.*, 245(2):275 – 310, 1996.

[303] A. Kaldor, D. M. Cox, D. J. Trevor, and M. R. Zakin. The chemistry and physics of molecular surfaces. *Z. Ph. D*, 3(2):195–204, Jun 1986.

[304] P. Li, G. Gao, Y. Wang, and Y. Ma. Crystal structures and exotic behavior of magnesium under pressure. *J. Phys. Chem. C*, 114(49):21745–21749, 2010.

[305] O. Kostko. *Photoelectron spectroscopy of mass-selected sodium, coinage metal and divalent metal cluster anions*. PhD thesis, Universität Freiburg, 2007.

[306] T. Diederich. *Elektronische Struktur und Stabilität von Silber- und Magnesiumclustern in Heliumtropfen*. PhD thesis, University of Rostock, 2003.

Acknowledgements

List of publications

1. L. Kazak, S. Göde, K.-H. Meiwes-Broer, and J. Tiggesbäumker. Photoelectron spectroscopy on magnesium ensembles in helium nanodroplets. *J.Phys. Chem. A*, 123(28):5951–5956, 2019. PMID: 31240915.

2. M. Kelbg, M. Zabel, B. Krebs, L. Kazak, K.-H. Meiwes-Broer, and J. Tiggesbäumker. Auger emission from the Coulomb explosion of helium nanoplasmas. *J. Chem. Phys.*, 150(20):204302, 2019.

3. M. Kelbg, A. Heidenreich, L. Kazak, M. Zabel, B. Krebs, K.-H. Meiwes-Broer, and J. Tiggesbäumker. Comparison of electron and ion emission from xenon cluster-induced ignition of helium nanodroplets. *J. Phys. Chem. A*, 122(41): 8107–8113, 2018. PMID: 30239204.

4. T. Ziegler, M. Rehwald, L. Obst, C. Bernert, F. E. Brack, C. B. Curry, M. Gauthier, S. H. Glenzer, S. Göde, L. Kazak, S. D. Kraft, M. Kuntzsch, M. Loeser, J. Metzkes-Ng, C. Rödel, H.-P. Schlenvoigt, U. Schramm, M. Siebold, J. Tiggesbäumker, S. Wolter, and K. Zeil. Optical probing of high intensity laser interaction with micron-sized cryogenic hydrogen jets. *Plasma Phys. Control. Fusion*, 60(7):074003, 2018.

5. D. Komar, L. Kazak, M. Almassarani, K-H. Meiwes-Broer, and J. Tiggesbäumker. Highly charged Rydberg ions from the coulomb explosion of clusters. *Phys. Rev. Lett.*, 120:133207, Mar 2018.

6. U. Zastrau, C. Rödel, M. Nakatsutsumi, T. Feigl, K. Appel, B. Chen, T. Döppner, T. Fennel, T. Fiedler, L. B. Fletcher, E. Förster, E. Gamboa, D. O. Gericke, S. Göde, C. Grote-Fortmann, V. Hilbert, L. Kazak, T. Laarmann, H. J. Lee, P. Mabey, F. Martinez, K.-H. Meiwes-Broer, H. Pauer, M. Perske, A. Przystawik, S. Roling, S. Skruszewicz, M. Shihab, J. Tiggesbäumker, S. Toleikis, M. Wünsche, H. Zacharias, S. H. Glenzer, and G. Gregori. A sensitive EUV Schwarzschild microscope for plasma studies with sub-micrometer resolution. *Rev. Sci. Instrum.*, 89(2):023703, 2018.

7. R. Irsig, M. Shihab, L. Kazak, T. Bornath, J. Tiggesbäumker, R. Redmer, and K.-H. Meiwes-Broer. The interaction of intense femtosecond laser pulses with argon microdroplets studied near the soft x-ray emission threshold. *J. Phys. B: At., Mol. Opt. Phys.*, 51(2):024006, 2018.

8. L. Obst, S. Göde, M. Rehwald, F.-E. Brack, J. Branco, S. Bock, M. Bussmann, T. E. Cowan, C. B. Curry, F. Fiuza, M. Gauthier, R. Gebhardt, U. Helbig, A. Huebl, U. Huebner, A. Irman, L. Kazak, J. B. Kim, T. Kluge, S. Kraft, M. Loeser, J. Metzkes, R. Mishra, C. Rödel, H.-P. Schlenvoigt, M. Siebold, J. Tiggesbäumker, S. Wolter, T. Ziegler, U. Schramm, S. H. Glenzer, and K. Zeil. Efficient laserdriven proton acceleration from cylindrical and planar cryogenic hydrogen jets. *Sci. Rep.*, 7, AUG 31 2017

9. G. Galinis, L. G. Mendoza Luna, M. J. Watkins, A. M. Ellis, R. S. Minns, M. Mladenovic, M. Lewerenz, R. T. Chapman, I. C. Edmond Turcu, C. Cacho, E. Springate, L. Kazak, S. Göde, R. Irsig, S. Skruszewicz, J. Tiggesbäumker, K.-H. Meiwes-Broer, A. Rouzee, J. G. Underwood, M. Siano, and K. von Haeften. Formation of coherent rotational wavepackets in small molecule-helium clusters using impulsive alignment. *Faraday Discuss.*, 171:195–2180, 2014.

10. V. Hilbert, C. Rödel, G. Brenner, T. Döppner, S. Düsterer, S. Dziarzhytski,L. Fletcher, E. Förster, S. H. Glenzer, M. Harmand, N. J. Hartley, L. Kazak, D. Komar, T. Laarmann, H. J. Lee, T. Ma, M. Nakatsutsumi, A. Przystawik, H. Redlin, S. Skruszewicz, P. Sperling, J. Tiggesbäumker, S. Toleikis, and U. Zastrau. Spatio-temporal coherence of free-electron laser radiation in the extreme ultraviolet determined by a Michelson interferometer. *Appl. Phys. Lett.*, 105(10):101102, 2014.

Submitted

11. M. Kelbg, M. Zabel, B. Krebs, L. Kazak, K-H. Meiwes-Broer and J. Tiggesbäumker. Temporal development of a laser-induced helium hanoplasma measured through impeded Auger emission and above-threshold ionization. Submitted.

In preparation

12. S. Göde, L. Kazak, A. Przystawik, M. Siegfried, J. Tiggesbäumker, K.-H. Meiwes-Broer. Growth study of magnesium foam ensembles in helium nanodroplets. In preparation.

Curriculum Vitae

Not included in the online version.

Selbständigkeitserklärung

Hiermit versichere ich, dass ich die vorliegende Arbeit selbständig angefertigt und ohne fremde Hilfe verfasst habe, keine außer den von mir angegebenen Hilfsmitteln und Quellen dazu verwendet habe und die den benutzten Werken inhaltlich und wörtlich entnommenen Stellen als solche kenntlich gemacht habe.

Rostock, den 23.08.2019

Lev Kazak